

Aus der Universität Bayreuth

# Motility and Force Generation Based on the Dynamics of Actin Gels

---

Dissertation

zur Erlangung des akademischen Grades

Doktor der Naturwissenschaften

– Dr. rer. nat. –

im Fach Chemie der Fakultät Biologie, Chemie, Geowissenschaften  
der Universität Bayreuth

vorgelegt von

**Stephan Schmidt**

geboren in Potsdam

Bayreuth, im Februar 2009

## Erklärung

---

Die vorliegende Arbeit wurde in der Zeit vom Dezember 2005 bis Mai 2007 im Max-Planck-Institut für Kolloid und Grenzflächenforschung in Golm, danach bis zum Februar 2009 in der Universität Bayreuth angefertigt. Die Betreuung an beiden Instituten erfolgte durch Prof. Dr. Andreas Fery.

Vollständiger Abdruck der von der Fakultät für Biologie / Chemie / Geowissenschaften der Universität Bayreuth genehmigten Dissertation zur Erlangung des Grades eines Doktors der Naturwissenschaften (Dr. rer. nat.).

Dissertation eingereicht am:	27.02.2009
Zulassung durch die Prüfungskommission:	11.03.2009
Wissenschaftliches Kolloquium:	18.05.2009
Amtierender Dekan:	Prof. Dr. Axel H.E. Müller

### **Prüfungsausschuss:**

Prof. Dr. Andreas Fery (Erstgutachter)  
Prof. Dr. Andreas Bausch (TUM, Zweitgutachter)  
Prof. Dr. Walter Zimmermann  
Prof. Dr. Franz Schmid (Vorsitz)

## **1 Table of Contents**

2	Introduction .....	5
3	Status of the Field .....	8
3.1	Structure and Properties of Actin.....	10
3.2	Actin Polymerization .....	11
3.2.1	Actin Treadmilling.....	12
3.2.2	The Effect of Regulatory Proteins .....	13
3.2.3	Formin Based Actin Polymerization .....	16
3.2.4	Reconstruction In Vitro .....	17
3.3	Actin Force Assays .....	19
3.4	Force Generation of Actin Filaments: Microscopic View.....	22
3.4.1	Elastic Brownian Ratchet .....	22
3.4.2	Tethered Ratchet Model .....	23
3.5	Force Generation of Actin Gels: Mesoscopic Elastic Model .....	28
3.5.1	Role of Stresses in Listeria Motility .....	30
3.5.2	Effect of Stresses on Gel Growth and Gel Symmetry Breaking 33	
3.6	Microscopy.....	37
3.6.1	Light Microscopy Basics .....	37
3.6.2	Phase Contrast Microscopy .....	38
3.6.3	Fluorescence Microscopy .....	40
3.7	Atomic Force Microscopy .....	43
3.7.1	AFM Working Principle .....	44
3.7.2	AFM Force Measurements .....	46
3.7.3	The Colloidal Probe.....	50
4	Preparation Procedures.....	52
4.1	Preparing the Actin In Vitro Medium.....	52
4.2	Preparation of the Bead Trajectory Assay .....	55
4.3	Force Assay Preparation Procedures .....	57

5	Results and Discussion.....	62
5.1	Trajectories of Actin Propelled Beads.....	62
5.1.1	Curvature Distribution of the Bead Trajectories.....	64
5.1.2	Trajectory Analysis in Confining Channels.....	76
5.2	AFM Force Measurements.....	83
5.2.1	Development of the AFM-Experiment.....	84
5.2.2	AFM Force Measurements for Varying Gel Size and Curvature.. .....	91
5.2.3	Effect of the Medium Composition.....	117
5.2.4	Formin Based Actin Polymerization and Generation of Force..... .....	126
5.3	Measuring Forces In-Vivo: Capsule Deformation in Cells.....	129
6	Conclusion.....	132
7	Zusammenfassung.....	136
8	Appendix.....	140
8.1	Parameters and Abbreviations.....	140
8.2	Force measurement on actin comets at the colloidal probe.....	142
8.3	Working up g-Actin.....	146
8.4	Grey Value Normalization in Image Stacks Using an Internal Reference.....	146
8.5	Automated Linear Fits for AFM Force-Distance Curves.....	147
9	References.....	152

## **2 Introduction**

It was in 1675 when van Leeuwenhoek discovered motile microscopic creatures in rainwater. He observed that these cellular microorganisms would “put forth little horns, extended and contracted, and had pleasing and nimble motions” [1]. Even after centuries of scientific development the significance of this observation remains. The key point of this discovery was that cells drive themselves actively by extension and contraction of their body. This mode of active motion is called cell crawling and it is an important part of fundamental biological and medical phenomena, such as: morphogenesis, wound healing, immune response and cancer spread. The basic concept of cell crawling has been established already almost 40 years ago, but it is the molecular details and the mechanism of the driving force that are subject of intense research until today.

Crawling cells generate their driving force by expanding the cytoskeleton against the leading edge of the cell. The cytoskeleton is almost solely comprised of a gel-like actin filament network. As the cell moves, actin filaments elongate by polymerization so that they collectively grow against the membrane. From a broader perspective the process appears as supramolecular self-assembly where the structure of the network and the polarity of the filaments establish an “auto-pilot” that directs the involved biomolecular reactions into forward motion of the cell. Even though the process of actin network formation seems to be straight forward, there are many unclear aspects, in particular concerning the generation of force. For example, the response to external forces, the regulation of the moving direction, and even the nature of the propulsive force are not understood. In this work we study these phenomena and focus on the following questions.

- What is the magnitude of forces generated by the actin gel and how does the gel morphology affect the generation of force?
- What are the mechanical properties of the actin network and how are these properties regulated?
- How is the direction and distribution of the force in the gel regulated? What are the implications for motility?
- How can we quantitatively measure forces in cells?

In order to analyze these problems we mainly address these problems using an *in vitro* approach: Here gel-motility and force measurements are conducted in stripped-down model systems. These are comprised of only purified proteins that reconstitute actin polymerization in solution. Second, measurements *in vivo*: Here force measurements are performed directly in living cells.

It is tempting to speculate about how the mesoscopic actin based motion is generated by just molecular self assembly of the actin gel, without any motor proteins. The *in vitro* approach allows conducting proper measurements in well defined conditions, without having to deal with the complex behavior of cells [2]. In the first part of the work we explore the *in vitro* motion of polystyrene beads that are propelled by an elongated actin network, very similar to the intracellular propulsion of pathogens like *Listeria* bacteria [3]. Here we analyze the bead-trajectories, the effect of geometrical confinement and extract statistical parameters governing the motion of actin propelled objects. We discuss the results based on existing actin force generation models [4] and provide further insight into the molecular mechanisms of actin based motility.

In the second part, the force generation of expanding actin gels is directly measured via a modified colloidal probe AFM technique *in vitro*. Using this technique we control the size and morphology of the expanding gels. This is important, because the force generation of actin gels is believed to be a function of the gel morphology [5, 6]. Therefore, by monitoring the forces in conjunction with the gel shape, we expect to gain new insights into actin based force generation. Another very important factor controlling the dynamics of actin gels are actin binding proteins and their composition in the medium. Using the same AFM technique, we study how the gel composition regulates the generation of force. For example, we vary the branching- and filament density to analyze their effect on the mechanical properties and force generation of the gel.

In the final part, we expand our focus towards *in vivo* studies. Such assays are harder to control due to the sheer complexity of cellular processes. Nevertheless, *in vivo* assays are fundamental, because mere *in vitro* results cannot always be extrapolated to the living cell. Therefore, it is worthwhile to compare the force data obtained *in vitro* with the forces generated in living cells. Here we measure the forces associated with phagocytosis, which is a major mechanism to remove pathogens from the organism. During phagocytosis intracellular forces are of vital importance as the defense cells exert mechanical forces in order to engulf and disarm the pathogens. Our approach is to offer capsules with

well defined mechanical properties to the phagocytes and measuring the capsule shape changes during engulfment into the cells.

From a technical point of view, the measurement methods developed in this work are rather versatile. They can be adapted for studying other force generation mechanisms in biological systems, but they are as well of interest for artificial responsive and force generating gels.

## **3 Status of the Field**

Understanding the biophysical basis of the coordinated action of actin scaffolds is an interdisciplinary challenge. It requires complete-as-possible biochemical control over the experiment and measuring techniques that span from molecular biology to material science. Also mathematical and computational modeling are important tools, as they relate the multitude of experimental findings, and also identify molecular mechanism that cannot (yet) be directly studied.

It was the crawling motion of cells that motivated the research on actin dynamics in the first place. As cells crawl on a substrate, they expand their actin cytoskeleton to form a cell-protrusion called lamellipodium. During lamellipodium formation a dendritic network of actin filaments imposes forces against the cell membrane and expands the cell [7]. On the molecular scale, this process can be depicted as follows: Actin filaments are polarized, meaning that they grow only at one end by inserting actin monomers. Monomer insertion leads to extension of the filaments by which the filament network generates a propulsive force. In the dendritic actin network, the filaments are aligned towards the cell membrane. Therefore, actin monomers are inserted primarily to filaments at the membrane where the force for the network expansion is required. The details of this process will be discussed in the course of this chapter.

The motile leading edge of crawling cells, the lamellipodium, is maybe the most relevant subject to study actin dynamics [8]. However, biophysical experiments on lamellipodial cell protrusions are impractical for studying the dynamics of a single molecular species. This is due to the interference of many different cellular activities on the actin machinery. For example, the complex behavior of an intact cell membrane, or the extraordinary high number of actin regulating proteins that exist in the cytoplasm [9, 10] make it difficult to analyze the biophysics of the actin network in cells. Therefore research has focused on simplified model systems, in particular on the intracellular bacterial pathogen *Listeria monocytogenes*. In 1989 [11] *Listeria* was found to be propelled by the actin contained in crawling cells. The bacteria virtually “highjack” the actin machinery from which it obtains an elongated actin network that grows against it, pushing it through the cytoplasm. It was found that the *Listeria* actin network undergoes the same kind of molecular reactions that take place at leading edge of



crawling cells (i.e. “actin treadmilling” see section 3.2.1). Since then research on *Listeria* has helped to indentify factors that promote actin based motion [3].

From the biochemical point of view a recent breakthrough was the discovery of the essential protein building blocks needed for actin based motion. This allowed for in vitro-reconstruction of *Listeria*-like motion under complete control of the actin network properties [12]. Such in vitro systems with a minimum set of components are extremely useful to study the complex interactions in an actin networks. For example, actin based motion of a functionalized bead from a minimum number of pure proteins, was used to study the general biochemical principles at work in actin based motility [13]. In this way, such in vitro studies in media comprising of pure proteins yield insight into actin-based motile processes of entire cells [14]. Here we use similar in vitro systems because they are a basic requirement for fully controlled physical measurements. Paragraph 3.2. presents the bimolecular mechanisms, the effect of regulatory proteins and the formation principles of actin networks as studied in this work.

Force measurements on actin dynamics make use of a diverse pool of measurement techniques of which micropipettes, optical tweezers and atomic force microscopy have been utilized so far. Section will 3.3 give an overview on these complementary techniques. Rheology measurements on actin networks in vitro are used to study their viscoelastic properties [15-17] and provide insight in regulation mechanisms that govern the mechanical properties of cells [18, 19]. Other methods like scattering techniques [20], electron microscopy [21] and fluorescence microscopy have been used to reveal the structure of actin filaments and networks as well as their biochemical activity. The latter has contributed to understanding the growth-regulation of actin networks [13, 22, 23] and its formation at the leading edge in lamellipodia protrusions [7, 24].

Recently, different models on the force generation of actin gels have been developed. They were inspired by finding actin polymerization alone being sufficient to propel *Listeria* and entire cells [12] without any motor proteins required. Therefore, the underlying mechanism can be assumed to be rather simple. However, the different models that have been developed are quite diverse as they analyze the mechanism on different scales. On the mesoscopic scale, a continuum model of *Listeria* propulsion was developed, relying on the elastic shear stress generated by growth of the actin network [5, 25]. This model has been extended to explain symmetry breaking of actin network (section 3.5.1) [26, 27]. On a microscopic level, force is thought to arise from directing the

thermal motion of the filament tips. This model is complementary to the mesoscopic elastic model and furthermore capable of explaining the actin based motion of flat surfaces and the trajectories of actin propelled beads [28]. A unifying model, which is still pending, would combine the elastic mesoscopic model and the microscopic ratchet model. So far, these two models are accepted by most researchers. According to these models the combined effects of the regulatory proteins in force generation can be explained (see sections 3.4 and 3.5). An important aspect for actin based motility in all models is that the propulsive forces are almost compensated due to antagonistic friction forces in the actin network. The magnitude of this internal friction force is usually much larger than the external force (e.g. viscous drag) that need to be overcome in order to keep moving. It is believed that this internal friction is still advantageous for moving organisms. If, for example, the bacterium or cell needs larger forces to overcome an obstacle, there is enough power in reserve that can be released by regulating the actin network properties. The same is true for the steady ATP consuming assembly and disassembly of actin filaments in the cytoskeleton which seems to be a waste of energy. The advantage is that the network is in a dynamic state, allowing for fast regulation of the network in response of external stimuli.

In the following the biochemical properties of actin networks and their regulation by actin binding proteins will be explained in more detail. The whole set of actin binding proteins described in the next part is used to prepare the actin networks for the different experiments. Then a brief overview of the actin force measurements methods will be given, followed by mathematical models on the actin based force generation. Finally, imaging methods and the general principle of the AFM as a force measurement technique are explained in this chapter.

#### ***3.1 Structure and Properties of Actin***

Actin is the most abundant protein in eukaryotic cells [10]. It is a 43 kDa globular protein that is able to polymerize under ATP hydrolysis into linear filaments. In the filamentous state (f-actin) it is the main regulator for the viscoelastic properties and transport phenomena of cells. Along with myosin actin is also a main component of muscle cells. In low ionic strength solution (in vitro conditions) actin remains in its monomeric globular state (g-actin). The molecular size of g-actin is 3.3 nm x 5.6 nm x 5.0 nm as determined by electron microscopy [21]. It consists of 376 amino acids on a single polypeptide chain. F-actin

forms a linear, two stranded and right-handed double helix which twists around itself every 37 nm (see Figure 3-1A, on page 12). Upon transformation from g-actin to f-actin almost no change in monomer size occurs [10, 21]. That is, in the filamentous form each monomer is 5.4 nm in size. F-actin is a supramolecular structure with a Kuhn length of 3-15  $\mu\text{m}$  as determined by fluorescence microscopy [29]. In cells many proteins bind to actin filaments to regulate its structure and polymerization kinetics (see paragraph 3.2). Very prominent examples of actin binding proteins are motor proteins (Kinesins) that slide along the filament axis. Sliding of motor proteins occurs in discrete steps under generation of force due to changes of their molecular conformation. It was observed that motor proteins “walk” in well defined directions on the filaments, showing that actin filaments possess a polar nature. The two different ends of actin filaments are called pointed and barbed ends. These terms stem from the direction of motion of motor proteins along the filaments. When discussing actin polymerization the filament ends are also termed minus (-) and plus (+) end, respectively. The polarity of f-actin controls the elongation direction of the filaments upon monomer insertion and release (treadmilling, see following section 3.2).

Introductory Literature: [30, 31]

Specialized Literature: [23, 32, 33]

### ***3.2 Actin Polymerization***

In high ionic strength solution containing ATP, globular monomeric actin (g-actin) polymerizes to form filamentous actin (f-actin), while depolymerization may take place at the same time. Actin polymerization and depolymerization (also called actin turnover) is sensitive towards the types of ions in the medium. The influence of  $\text{Mg}^{2+}$  and  $\text{Ca}^{2+}$  is known to be relevant in vivo and has therefore been investigated in vitro [10]. In pure actin-buffer media the turnover rate is on the order of 0.03  $\mu\text{m}/\text{min}$ , which is 100 times smaller than in vivo. This shows that in nature actin turnover is strongly enhanced by enzymatic activity. This will be discussed in the following sections, as will be the basics of actin treadmilling, the nucleation of actin polymerization and the reconstruction of actin based motility in vitro.

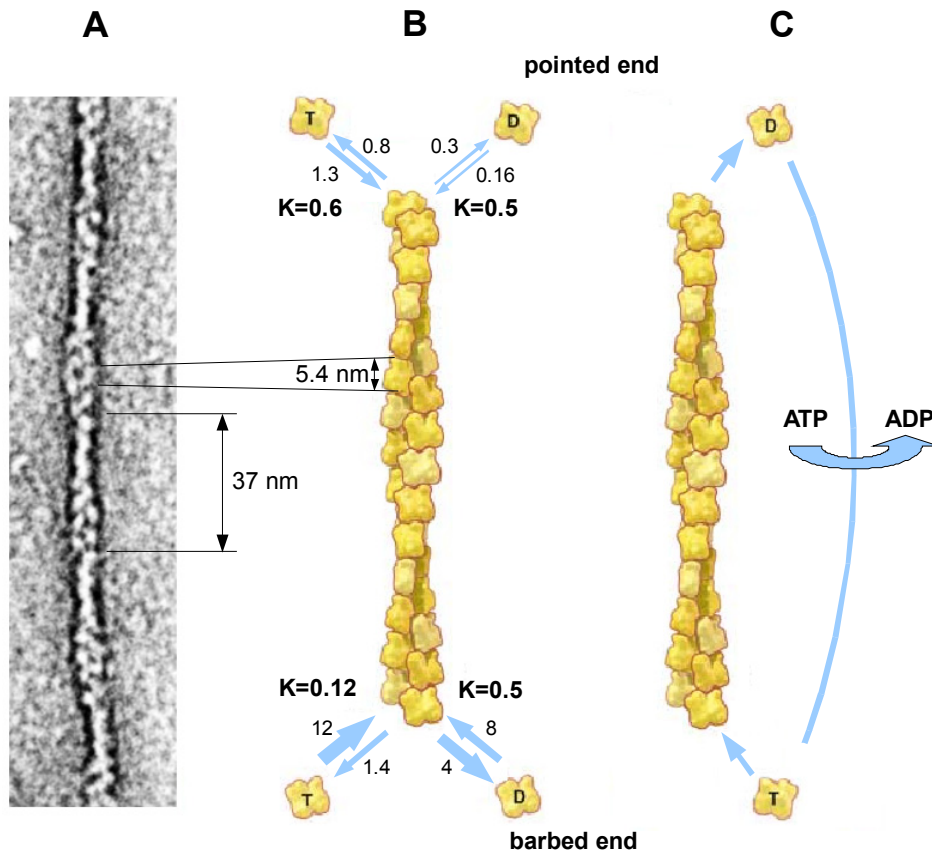


**Figure 3-1** F-actin dimensions (de)polymerization and rate constants. A) Electron micrograph of a single actin filament. The right-handed helical structure is visible. B) Reconstructed f-actin structure; T-denotes ATP-actin, D-denotes ADP-actin ; The association rate constants have units of  $\mu\text{M}^{-1}\text{s}^{-1}$ . The dissociation rate constants have units of  $\text{s}^{-1}$ . Both represent in vivo values. The ratio of the dissociation rate constant to the association rate constant gives  $K$ , the dissociation equilibrium constant with units of  $\mu\text{M}$ . The equilibrium constants for ATP-actin differ at the two ends in case of ATP-actin, giving rise to slow steady state treadmilling under consumption of ATP C). Modified from original artwork in [23].

### 3.2.1 Actin Treadmilling

Due to the polarity of actin, the turnover rate is enhanced at one filament end, the barbed end. The barbed end associates and dissociates g-actin at a rate one order of magnitude faster than the pointed end. The ratio of the rate constants for association and dissociation of the actin monomers  $k_-/k_+$  is the dissociation equilibrium constant  $K$  for subunit binding at the end of a filament. When the rates of polymerization and depolymerization at both ends balance, the monomeric g-actin is at its *critical concentration*  $[A_G]$ , which is the equilibrium constant  $K = [A_G] = k_-/k_+$ . In absence of ATP hydrolysis the critical

concentration of g-actin is the same at both ends  $K = [A_g] \approx 0.5 \mu\text{M}$ , see Figure 3-1). In this case the length and *position* of actin filaments do not change. Now, the unique feature of actin filaments is that they can change their position upon regulating the g-actin turnover. This is always accompanied with ATP hydrolysis. When actin monomers bind ATP and polymerize a kinetic asymmetry is produced at the two ends of the filaments. As a result, the effective affinity for new monomers at the barbed end is high and the critical concentration is low ( $\approx 0.12 \mu\text{M}$ ). At the pointed end the affinity stays low, the critical concentration is large ( $\approx 0.7 \mu\text{M}$ ). The consequence of this asymmetry is “treadmilling”: Depolymerization from the minus end is balanced by polymerization onto the barbed end, without changing the average filament length. Therefore, the filament displaces itself in direction of the barbed end. Monomeric ADP-g-actin is recycled by diffusion and binding to ATP. Thus, treadmilling consumes chemical energy via ATP hydrolysis. With the rate constants for the barbed end  $k_+^b$ ,  $k_-^b$  and the pointed end  $k_+^p$ ,  $k_-^p$  the load free polymerization rate can be described as:

$$\frac{d[A_f]}{dt} = (k_+^b + k_+^p)[A_f][A_g] - (k_-^b - k_-^p)[A_f] \quad \text{Eq. 3-1}$$

### 3.2.2 The Effect of Regulatory Proteins

In crawling cells a large number of actin binding compounds affect the properties of the filament network formation. Here we focus only on the proteins that are part of the in vitro medium used in this work.

**Treadmilling regulation by ADF and profilin:** The behavior of actin in the lamellipodium or at intracellular pathogens is different compared to pure actin in buffer solutions. For example: Actin filament growth is nucleated at the cell- or bacteria membrane to grow into dense polarized filament scaffolds, or actin gels. Furthermore, actin filaments in cells grow 100 times faster than in pure buffer. The increased growth speed of individual filaments can be partially attributed to the action of the proteinic enzymes ADF and profilin.

ADF (actin depolymerization factor, also called cofilin) accelerates minus-end depolymerization, which is the rate limiting step in the ATP consuming treadmilling cycle [34]. As a result, a higher steady-state concentration of monomeric ATP-actin is established in f-actin solutions containing ADF. This

promotes faster plus-end growth and balances the faster pointed end depolymerization. In other words ADF increases the actin turnover rate by increasing the reverse growth rate at the pointed end  $k_{-}^p$ . Eq. 3-1 directly shows that by increasing  $k_{-}^p$  the filament growth  $d[A_f]/dt$  rate is increased. Recently, the proposed treadmilling increase mechanism by ADF as presented in [34] is under debate. Newer work argues that ADF inhibits g-actin dissociation at barbed ends and increases dissociation at pointed ends only up to the ADP-actin rate [35]. However, the exact mechanism has no effect on the force generation or the network growth as a whole.

When profilin is added to the medium, the large pool of ADP-g-actin, which underwent accelerated dissociation reactions at the pointed ends by the action of ADF, is converted into the ATP-bound profilin-actin complex. This complex has the unique property to polymerize at barbed ends only [36]. Therefore, profilin enhances the processivity of treadmilling and also serves as the nucleotide exchange factor for actin, catalyzing the exchange of ADP for ATP. In vitro, treadmilling is accelerated by 125-fold by the synergistic effects of ADF and profilin, reaching values close to those found in vivo [37]. Profilin promotes barbed end association and the concentration of the ATP bound monomer  $[A_g]$ . As a result, profilin enhances barbed end polymerization (see Eq. 3-1).

***Nucleation and branching with N-WASP and ARP2/3:*** Nucleation of filaments by only actin monomers is unfavorable owing to the instability of small actin oligomers in vivo [38]. Thus, the question is on how actin filament growth is nucleated and spatially confined to the leading edge of a lamellipodium or the rear of *Listeria* bacteria. Figure 3-2A shows an actin comet growing from a *Listeria* bacterium. Here single actin filaments are obviously in contact with the bacteria surface. It was found that actin polymerization is nucleated at the bacteria surface by a complex of two proteins: ActA, which is bound to the bacteria surface and ARP2/3. ActA is a protein that belongs to the WASP family (WASP: Wiskott Aldrich Syndrom Protein). WASP proteins form an activated complex with ARP2/3 which is able to nucleate actin polymerization [39]. Besides the WASP family proteins, a few other nucleation promotion factors (NPFs) are known [22]. As NPF we use N-WASP, the neural isoform of WASP or formins (see next subsection). When N-WASP is activated, the ARP2/3 complex is believed to undergo structural conformation followed by association to a g-actin monomer. This surface bound system, N-WASP|ARP2/3|g-actin,

## 3.2 Actin Polymerization

represents the nucleation center of a new filament. Furthermore, it was observed that free barbed ends can transiently attach to the surface bound NPFs via g-actin bound before to the NPF [40]. The NPFs therefore fulfill another function; they serve as “tether points” at the load to be pushed by the filaments. Filament tethering might help to stabilize actin propulsion [41]. The finding that actin filaments are partially tethered to the load they push [6, 42], has stimulated development of models regarding the force generation of growing actin networks (see section 3.4).

The ARP2/3 protein consists of two subunits ARP2 and ARP3. The molecule possesses a Y-shape with subdomains that allows branching the filament into a mother and a daughter filament. The branched filaments grow at an angle of  $70^\circ$  to each other and form a dendritic array in nascent ARP2/3-actin gels. ARP2/3 is assumed to generate new filaments by interacting with the products of the polymerization reaction, i.e. actin filaments [43]. Hence, the branching process incorporates new filament branches into the pre-existing network, providing a strengthened scaffold that supports the force generation against a load (Figure 3-2B). Multiple branching also enhances the network growth by multiplying the barbed ends, which represent additional polymerization sites. With generation of new polymerization sites by ARP2/3 induced branching, the kinetics of actin polymerization become autocatalytic. This is different to the nucleation-growth kinetics of for the polymerization of pure actin. The exact mechanism of branch formation, the conformation of the NPF-ARP2/3 complex and the role of ATP hydrolysis upon ARP2/3 branching are still under debate [22].

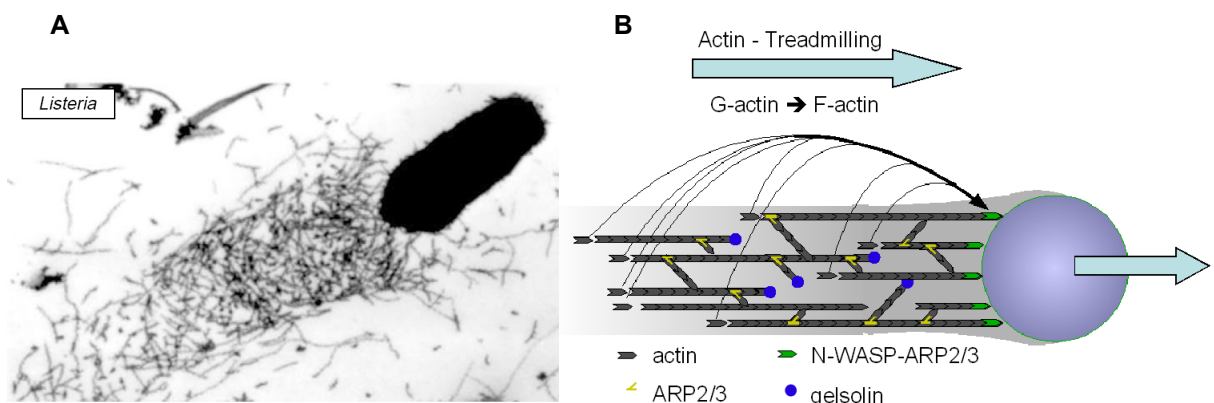


**Figure 3-2** Branched networks in ARP2/3 mediated growth A) EM image of a *Listeria* bacteria showing individual actin filaments in an actin comet attached to the rear of the bacteria (taken from [3]). B) Schematic image of the reconstructed *Lis-*

*teria* with the proteinic constituents of the actin network and an N-WASP coated bead.

Since the ARP2/3 controls the degree of branching in the network, we expect a change in the mechanical properties upon varying the APR2/3 concentration in the medium. ARP2/3 is one of the candidates by which cells regulate the network morphology and its ability to generate forces. In this work we vary the ARP2/3 concentration and measure the effect on the forces generated by the actin network.

***Capping of ARP2/3 regulated actin networks:*** There are a number of proteins that “cap” barbed ends and prevent the filaments from elongating. In this work we use gelsolin to cap filament ends. Capping proteins are required for efficient motility in ARP2/3 branched networks. In these dendritic networks the major fraction of actin filaments does not have direct contact to the load, i.e. the cell membrane or bacteria. Capping proteins enhance motility by two possible mechanisms: 1) By blocking a large fraction of the barbed ends, the capping proteins funnel the flux of actin monomers to feed the growth of only a few, uncapped filaments [13]. These uncapped filaments grow fast and therefore they constitute the front of the actin network. Since at the front most of the polymerization activity is required, the capping proteins enhance the network motility. 2) Other work [44], argues that capping enhances motility via promoting the filament nucleation by the Arp2/3 complex. It is assumed that free barbed ends compete with the Arp2/3 complex for NPF bound actin monomers. Capping proteins are proposed to promote nucleation of new filaments by capping the barbed ends of “old” filaments near the NPF-surface. These capped “old” filaments cannot compete for activated g-actin at the NPF surface. This would increase the concentration of free NPFs on the surface ready to form nucleating complexes with Arp2/3. Hence nucleation of new filaments and network growth is enhanced.

The capping protein used in this work is gelsolin and we vary its concentration in the medium to assess its effect on the force generation. Its is believed to promote branching, at least according to the second mechanism described above. Therefore gelsolin should have a pronounced effect on the mechanical properties and the generation of force.

#### ***3.2.3 Formin Based Actin Polymerization***



## 3.2 Actin Polymerization

Besides N-WASP|ARP2/3|g-actin based nucleation and polymerization, there is another mode of actin polymerization where formins emerged as the nucleator and key-regulator [45, 46]. The main difference to ARP2/3 driven network growth is that the formin mechanism generates linear, unbranched filaments. Therefore, the formin-built networks are not dendritic and should have completely different mechanical properties as compared to ARP2/3 associated networks. The mechanical properties of dendritic and non-dendritic networks will be investigated and compared in this work.

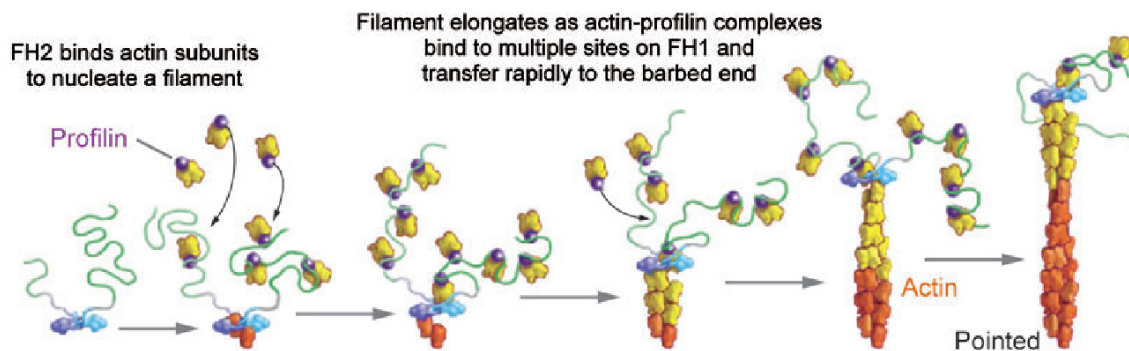


**Figure 3-3** Elongation mechanism with actin-profilin binding to multiple sites on the FH1 domains and transferring rapidly to the barbed end growing in association with the FH2 domain. Image from [31].

Formins can interact with actin in two principally different ways, using its subdomains FH1 and FH2. First, the formin subdomain FH2 nucleates actin polymerization and can interact with barbed ends [47]. Second, FH1 domains have sequences that interact with profilin. Because profilin can bind simultaneously to FH1 and to an actin monomer, FH1 domains tether multiple profilin/actin complexes near the end of a growing filament (Figure 3-3). It is not known how actin units at FH1 insert themselves at the actin units at FH2. However, this type of monomer additions shows a large processivity: The formins stays attached to the filament barbed end for more than 1000 subunits added and generate long linear filaments. This is a complex process that will not be discussed in further detail, as it is not relevant to the presented work, see [22] for a recent review on the molecular details.

### 3.2.4 Reconstruction In Vitro

As a result of the discovery of the biochemical mechanisms that control actin dynamics, minimal media have been designed allowing assays in a controlled

fashion and apart from the “crowded” cellular conditions. Such media contain only the minimum set of purified proteins required for actin based motion, as described in section 3.2.2. Assays in these media clearly show, that no motor proteins are required for *Listeria* type motion. Instead, this type of motion, and to a major extend also the crawling motion of cells, depend solely on directional actin polymerization. Generally, NPF coated colloidal objects, like polystyrene beads, lipid droplets or lipid vesicles are utilized as actin driven objects in reconstructed in vitro assays [48-50]. The first successful complete reconstruction of *Listeria*-like actin based motion was reported in 1999 [12]. NPF coated microspheres in actin rich cell extracts have been studied before [51]. In all in vitro media prepared in this work, ATP is required as energy source, as well as ADF and profilin for fast actin treadmilling. Dendritic *Listeria*-like networks are formed at N-WASP coated surfaces of colloidal beads that are brought into contact with actin media containing ARP2/3 and gelsolin [12, 48]. Figure 3-2B (p. 15) shows the schematic description of actin based propulsion of an artificial bead by a dendritic actin network. This type of reconstructed medium is used for assays presented in section 5.1 and 5.2. The minimum medium required for formin based actin polymerization does not require ARP2/3 or gelsolin, but profilin/ADF and formin coated colloidal objects [52]. The experiments with formin coated beads result in unbranched, non-dendritic networks. The respective results are presented in section 5.2.4.

Introductory literature: [30, 31]

Specialized literature: [13, 14, 22, 23, 32]

### 3.3 Actin Force Assays

In vitro experiments in minimum motility media suggested that force generation and motility of *Listeria* type motion is merely due to the polymerization of actin filaments against the motile objects. Although hypothesized [53], for ARP2/3 mediated actin polymerization so far no molecular motors based on conformation-change were discovered. In case of formin based actin polymerization, force generation due to conformation changes of the formin molecule is more likely. The structure and processivity of the formin motor suggest that conformation changes take place during actin polymerization. However, a direct experimental prove is yet to be found [22].

From basic motility assays, the characteristics of actin based force generation remains rather puzzling and even inconsistent. For example, velocity measurements of actin propelled colloids in media with varying viscosity suggested a self-strengthening response of the actin network as the drag force is increased. This rendered the velocity of propulsion largely independent of the drag force [48]. However, similar measurements performed by another group of researches indicated that the velocities depended on the viscous drag force [54]. Others observed that *Listeria* appeared to advance in discrete steps of 5.5 nm, similar to the size of an actin monomer [42]. These steps could suggest some intrinsic molecular scale mechanism at the interface between filaments and the surface, which is also yet to be proven. The next logic step in further understanding actin based motion would be a direct measurement of the polymerization force on a growing actin gel. Several techniques have been successfully used. Their working principles and the results will be briefly explained in the following.

**Micropipettes:** Marcy et al. used a micromanipulation approach [55]. Here a *Listeria* like comet grows at a bead attached to a thin glass fiber. The force is measured by recoding the deflection of the glass fiber using optical microscopy. To apply forces, the comet was pushed or pulled by a micropipette, while recording the growth speed of the comet. By pushing (positive) or pulling (negative) forces on the order of -1.7 to 4.3 nN were applied and the force–velocity relation was established. Marcy et al. found linear force-velocity regimes for both pulling and pushing forces, which decays more rapidly for pulling forces. Furthermore, by pulling the actin tail away from the bead at high speed, the elastic modulus of the gel and the force necessary to detach the tail from the bead were estimated. Also thickening of the gel was observed upon pushing

forces, which could explain the self-strengthening of the actin network upon compression.

Friction forces in the actin network have been measured in the same group utilizing a very similar setup [56]. With the micropipette the comet was pulled 2-3 times faster than its natural growth speed, which resulted in an oscillating behavior of force and velocity. This result suggests a stick slip phenomenon where smooth movement occurs when an average number of filaments remain attached to the bead, whereas stick-slip motion occurs when a cooperative breaking happens. This work suggests that both, actin polymerization and connection of actin filaments to the surface, is controlled by the N-WASP|ARP2/3 complex.

**Atomic Force Microscopy (AFM):** A modified AFM was used to study the force generation and load dependence of actin polymerization by Parekh et al. [57]. The AFM measurement technique was optimized to account for the unpredictable drift in z-direction which becomes problematic in long term measurements at constant piezo positions [58]. Here actin was polymerized in cell extracts at the apex of a standard contact mode imaging cantilever. Parekh obtained force–velocity curves of growing actin networks until network elongation ceased at the stall force. The growth velocity was found to be load-independent over a wide range of forces before stalling, which could be due to self-strengthening of the actin network. When decreasing the forces on the growing network, the velocity increased to a value greater than the previous velocity, similar to the results found by Marcy et al. [55, 56]. Among other differences to the AFM experiments shown in this work (see section 5.2), the measurements by Parekh et al. involve a flat force probe geometry. Also the actin network grows in a cytoplasmic extract, whereas we use a completely reconstructed medium comprised of pure proteins. This gives us the opportunity to control the properties of the actin gel and to test various the gel compositions. One aim of our approach is to learn about the role of regulatory proteins in the generation of force.

The same group also performed AFM based microrheology assays on dendritic actin networks and reported stress stiffening followed by a regime of reversible stress softening at increasing loads [59]. Stress stiffening is attributed to entropic elasticity of individual filaments, while the softening behavior can be explained by elastic buckling of individual filaments under compression.

**Lipid vesicles/droplets:** To probe the polymerization forces quantitatively in a reconstructed in vitro assay, two similar experimental systems have been introduced at about the same time. Lipid vesicles [50] and lipid droplets [60] were coated with ActA to form a dendritic actin comet in a suitable ARP2/3 containing medium. Unlike hard plastic beads (see section 5.1) the “soft” vesicles and droplets deform as the dendritic actin network evolves at their surface. The reason is buildup of elastic tension due to insertion of monomers at curved surfaces (see section 3.5). Both groups analyze the shape of the soft colloidal objects and deduce the compression forces associated with actin polymerization. According to Giardini et al. [60] the forces are on the order of 0.4-4 nN for a droplet with a spherical radius of 1.45  $\mu\text{m}$ . The forces determined by Upadhyaya et al. [50] are on the order of 3-8  $\text{nN}/\mu\text{m}^2$ . An example of a deformed lipid vesicle is shown in Figure 3-7C (p. 33).

**Optical tweezers:** Force measurements on a small number (approximately eight) of parallel filaments were performed by Footer et al. [61]. The micro fabricated setup mimics the geometry of filopodial of crawling cells protrusions. The unparalleled sensitivity of optical tweezers was required to the measure force which was on the order of 1 pN. This relatively small value was attributed to the fact that only one filament at a time is in contact with the force probe. This is consistent with the theoretical load required to stall the elongation of a single filament. The results imply that living cells must use actin-associated factors to enhance the force generation ability of small filopodia-like actin bundles.

### 3.4 Force Generation of Actin Filaments: Microscopic View

Surprisingly all molecular motors, like stepping, rotary, and filament motors, work on the same general principle. Short range molecular interactions between the motor and the support “catch” favorable Brownian fluctuations in order to move the load [62]. Filament motors are less complex “one shot”-motors, but still efficient enough to explain the actin based propulsion. In this section the working principle of filament motors will be explained, which is covered by the Elastic Brownian Ratchet model. The specific working principle of dendritic actin networks is accounted for in a specialized Elastic Brownian Ratchet model, the Tethered Ratchet model.

#### 3.4.1 Elastic Brownian Ratchet

In case of a simple Brownian ratchet the filament do not actually “push” the object but rather rectify its Brownian motion. Such models [62] predict that the load’s velocity should depend on its diffusion coefficient and therefore on its size. However, experiments failed to show such size dependence, and so the Elastic Brownian Ratchet model was developed by Mogilner and Oster [63]. The Elastic Brownian Ratchet model suggests that thermal bending undulations of a semi-stiff actin fiber, rather than load diffusion creates the polymerization gap and the elastic force of the filaments push the load forward.

By polymerizing a filament against the load force  $f_L$  using the free energy of binding a monomer onto the tip of the filament chemical energy is converted into a mechanical force. The load free filament elongation rate is  $V_p = l \cos \theta (k_+[A_g] - k_-)$ , where  $l = \delta \cos \theta$  is the projected size of a monomer in direction of motion,  $\delta$  the effective monomer size,  $[A_g]$  the monomer concentration,  $k_+$  and  $k_-$  the rate constants for polymerization and depolymerization at the barbed end, respectively. In order for a monomer to bind to the tip of a filament a gap of size  $\delta \cos \theta$  must open between the load and the filament and remain open for a time  $\sim 1/k_+[A_g]$  to allow for a monomer addition event to take place. Using the fact that the thermal fluctuations of a filament tip is much faster than the elongation rate, the polymerization velocity is given by the equation  $V_p = \delta \cos \theta (k_+[A_g] \cdot p(\theta, f_L) - k_-)$ . That is, the polymerization rate is weighted by the probability  $p(\theta, f_L)$  for a gap of sufficient size and duration to allow for monomer insertion. This probability depends on the load force  $f_L$

pushing against the polymerizing filaments. In general the function  $p(\theta, f_L)$  must be calculated numerically. Mogilner and Oster have shown that in the biological relevant regime  $p = \exp[-f_L l / k_B T]$ , where  $f_L l$  is the work done required to move the load a distance  $l$ . The principal equation of the Elastic Brownian Model then reads

$$V_p = V_{max} \exp[-f_L l / k_B T] - V_{dep} \quad \text{Eq. 3-2}$$

where  $V_{max} = l \cdot k_+ \cdot [A_g]$  is the free polymerization velocity and  $V_{dep} = l \cdot k_-$  is the depolymerization velocity.

### 3.4.2 Tethered Ratchet Model

The elastic Brownian ratchet model was developed to account for the finding that the velocity of an actin propelled object is invariant with the size of the object. It is an extension of the classic thermal ratchet [62] model, developed to include this additional aspect. However, another incompatible observation arose, namely the actin filament appeared to be attached at the *Listeria* membrane or bead surface. This was shown in a number of experiments using electron microscopy [6], [64] or *Listeria* diffusion measurements [42] and (pull-off) force measurements [56]. These observations fit very well with biochemical models on ARP2/3 mediated polymerization, which proposed that ARP2/3 forms a complex with surface bound nucleation promoting factors (NPFs) [22] to initiate actin polymerization. The problem in the Elastic Brownian Model is that it remains unclear how the filaments can insert monomers and generate force when they are attached to the surface. The ‘‘Tethered Ratchet’’ model proposed by Mogilner and Oster [41] solves this problem by assuming that the filaments attach to the bacterial surface only transiently.

The model considers two population of filaments: a) attached filaments, that are stretched due to the forward motion of the load and hence resist forward motion by imposing a force  $f_a$ ; b) dissociated, growing filaments that are compressed and working against the load each with an elastic force  $f_w$ , see Figure 3-4 for a graphical illustration.

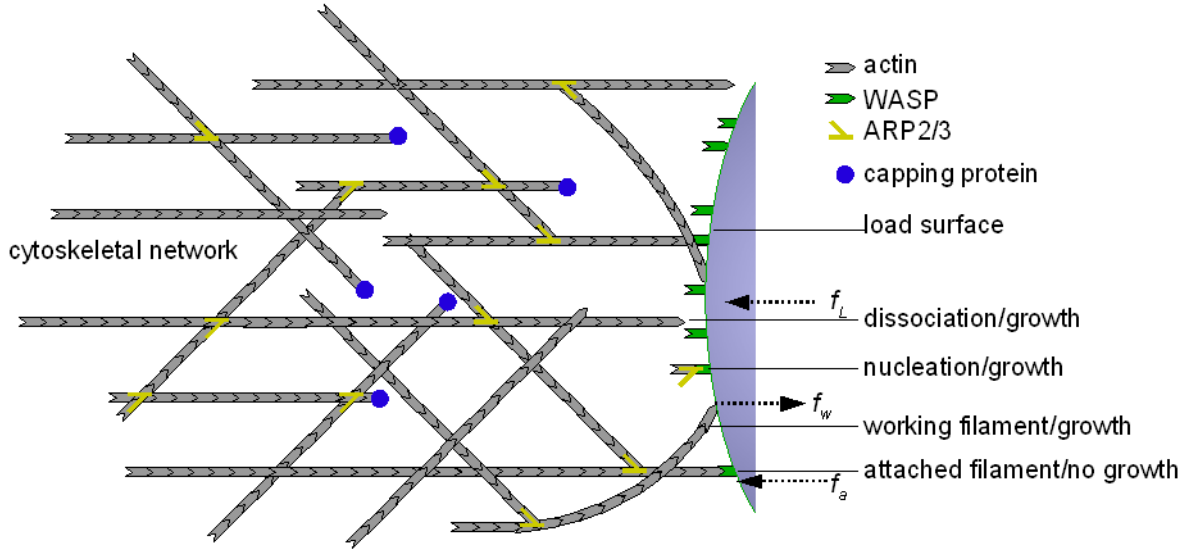


**Figure 3-4** Sketch of the Tethered Brownian Ratchet model. Working filaments (curved) are formed when attached filaments dissociate and with rate  $k_d$  and are capped with rate  $k_c$ . Attached filaments are generated with nucleation rate  $k_n$ . Force balance: the polymerization ratchet force,  $f_w$ , generated by the working filaments is balanced by the force of attachment,  $f_a$ , and load force,  $f_L$ .

The model consists of three principal equations that describe a) the number of attached/detached filaments at the surface, b) a force balance equation and c) equations that connect the force with the filament dissociation rate. In the following these relations will be written down and briefly explained. The complete derivation can be found in the publication by Mogilner and Oster [41].

**a) Number of filaments near the surface:** The rate of attached filament formation is  $da/dt = n - k_d a$ , where  $n$  is the nucleation rate of attached filaments,  $k_d$  the dissociation rate and  $a$  the number of filaments attached to the surface. The working filament formation rate is  $dw/dt = k_d a - \kappa w$ , where  $\kappa$  is the capping rate of the working filaments,  $w$  and  $a$  are the number of the working and attached filaments, respectively. The solutions of these equations are

$$a(v) = n/k_d, \quad w(v) = n/\kappa. \quad \text{Eq. 3-3}$$

We will see in the following that the number of attached filaments ( $a$ ) and detached filaments ( $w$ ) depend on the propulsion velocity of the load ( $v$ ).

**b) Force balance:** With the forces exerted by the attached and working filaments  $f_a$  and  $f_w$ , respectively, and  $f_L$  the load force the force balance reads



$$w \cdot f_w = a \cdot f_a + f_L, \quad \text{Eq. 3-4}$$

**c) force-dissociation relation:** The dissociation rate  $k_d$  of filaments from the bead surface depends on the force acting on the link: pulling on a bond lowers the activation barrier and enhances dissociation. This has been observed experimentally by [55] who showed that the comet tail could be detached from the bead by tearing at it. The actual relation between the dissociation rate and the force depends on the form of the potential associated with the link, but in many cases it can be approximated by an exponential relation [65].

$$k_d = k_{d,0} \exp(f/f_b) \quad \text{Eq. 3-5}$$

where  $f_b$  is the characteristic strength of an attachment bond. If the load moves at a velocity  $V$ , then at a time  $t$  after an attachment the force applied to the molecular link is  $f = k_a V t$ . Thus the force applied to the attachment link is velocity dependent. By a similar argument the dissociation rate is velocity dependent,  $k_d = k_{d,0} \exp(k_a V t / f_b)$ .

**Characteristics of the Model:** Substituting the force balance Eq. 3-4 into the force-velocity equation obtained from the Elastic Brownian Model (Eq. 3-2) leads to:

$$V_p = V_{max} \exp[-l(f_a(a/w) + (f_L/w))/k_B T] - V_{dep} \quad \text{Eq. 3-6}$$

The number of the working filaments  $w$  and attached filaments  $a$  are unknown and depend on the velocity of polymerization, as  $k_d$  depend on the velocity (Eq. 3-5) and is connected with  $a$  and  $w$  (Eq. 3-3). To overcome this problem a velocity scale  $V_0$  is introduced and Eq. 3-6 can be rewritten. Roughly speaking, when the polymerization velocity exceeds a certain velocity  $V_p > V_0$  then the filament attachment links are deformed, and the bonds break faster than with their free dissociation rate. Hence  $a$  decreases and  $w$  increases in this case. If  $V_p < V_0$  then the bonds break with their free polymerization rate. Eq. 3-6 can be rewritten the dimensionless form with  $v \equiv V_p/V_0$ ,  $\varepsilon_1$  the work done per filament in breaking an attachment,  $\varepsilon_2$  the dimensionless free polymerization ve-

locity,  $\varepsilon_3$  the dimensionless free depolymerization velocity,  $\varepsilon_4$  the work done per working filament on the load:

$$v = \varepsilon_2 \exp[-\varepsilon_1 v \omega^2(v) - \varepsilon_4] - \varepsilon_3 \quad \text{Eq. 3-7}$$

This equation can be used to analyze the Brownian ratchet model. Here  $\omega$  is a function that describes the velocity dependence of the dissociation rate  $k_d$  and the attachment force  $f_a$ . It has the following behavior: a) For slow movement,  $v \ll 1$ ,  $k_d \approx k_{d,0}$ ; that is the dissociation rate is equal to the free dissociation rate, and  $f_a \propto v$ ; i.e. the attachment force is proportional to the velocity. b) For fast movement  $v \gg 1$ ,  $k_d \approx k_{d,0} v / \ln(v)$ ; the dissociation rate increases with the velocity in a sub linear way, and  $f_a \propto \ln(v)$ ; the detachment force increases logarithmically with the velocity. With the parameters of ARP2/3 mediated polymerization shown in appendix 8.1 Eq. 3-7 can be numerically solved. The result is illustrated in Figure 3-5A. For small velocities Eq. 3-7 is a decreasing function because for slow movement the dissociation is constant, whereas the force of attachment that resists the working filaments is proportional to the velocity. For faster movement, the force of attachment increases with velocity more slowly than the dissociation rate. Therefore, Eq. 3-7 is a slowly increasing function of the velocity.

Mogilner and Oster predict that the force-velocity relation for a bead or *Listeria* computed with Eq. 3-7 is biphasic. At small loads, the velocity decreases very fast, while for greater loads the velocity decreases more slowly. The reason is, that for almost zero load ( $f_L$ ), when the object moves in the fast regime, the attachments break quickly and the resistance from the attachment links is small. For a small increase in load the bacterium is slowed which increases the drag as the filaments stay attached longer. This positive feedback decreases the velocity very quickly as the load grows. At still larger loads the object moves in the slow regime where the attachment links break at their free dissociation rate. In this case a positive feedback is not observed. As a result, the velocity decreases not as strongly for larger loads.

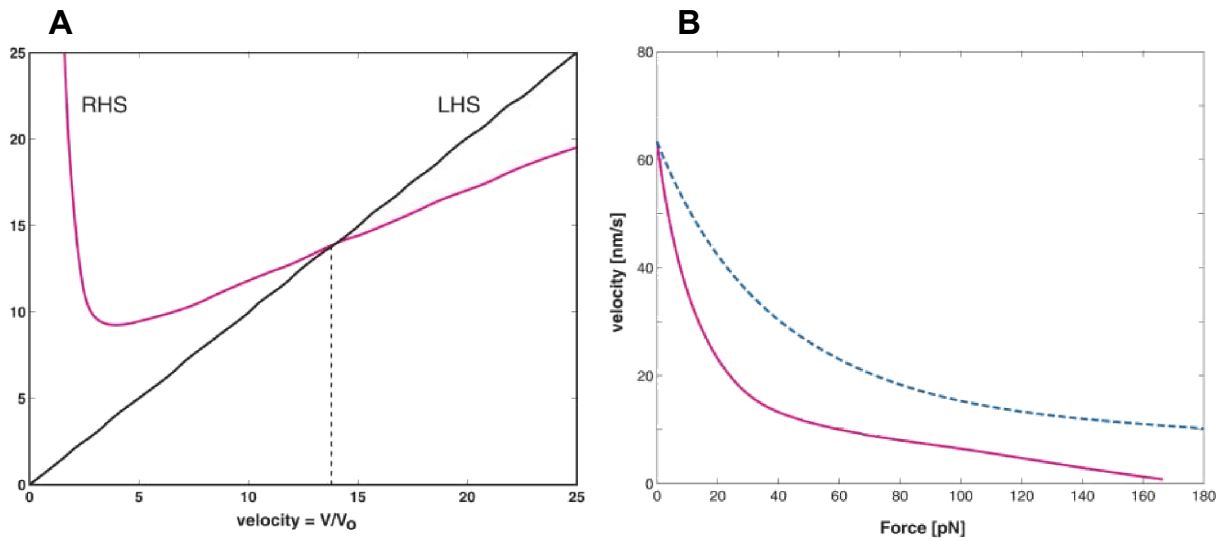


**Figure 3-5** A) The right-hand side (RHS) of Eq. 3-7 (magenta) is displayed as the function of the dimensionless velocity,  $v$ . The left-hand side corresponds to the straight line. The intersection gives the steady-state value of  $v$ , and shows that actin propelled *Listeria* move in the “fast” regime (see text) . The non monotonic shape of the right-hand side accounts for the biphasic behavior of the load-velocity curve in B): The force-velocity curve for *Listeria*. The solid curve corresponds to the parameter values in appendix 8.1. The dashed curve corresponds to a threefold increase in nucleation rate over the solid curve, and illustrates the effect of filament density on the load-velocity behavior. Both graphs were taken from [41].

### 3.5 Force Generation of Actin Gels: Mesoscopic Elastic Model

On the mesoscopic scale the force generation of actin networks can also be described by treating the network as a continuous medium. This approach is complementary to the microscopic picture of the actin network in the framework of the “Tethered Ratchet” model, both models do not contradict each other. The mesoscopic model proposes that insertion of actin monomers induces elastic deformations in the gel: Nascent actin layers at the nucleating surface displaces and deforms previously formed filament layers. In that view, the energy produced by actin polymerization is not used directly for propulsion but first stored in form of elastic energy in the gel. As boundary conditions for buildup of elastic energy, the gel has to be crosslinked and growing from curved surfaces. We consider a bead with a curved nucleating surface, e.g. coated with N-WASP. Furthermore the filaments are branched via ARP2/3, and therefore form physical crosslinks. Outward growth of actin filaments extends the crosslinks of previously grown actin layers as they are forced to attain a larger radius. This is the basis of elastic energy buildup ( $\propto R_{gel}^3$ ) and associated phenomena like cessation of gel growth, gel symmetry break or motility [25].

**Calculation of strains and stresses in the actin gel:** For force generation and motility the stress buildup on the load’s surface is of general interest. In the following the stress in a piece of spherical actin gel is calculated. For this work calculations on a more complicated geometry (Figure 5-24, p.111) would be more appropriate. However, an analytical solution for the geometry studied here cannot be found. We therefore compare the experimental results from predictions of the spherical geometry only (Figure 3-6, p.29). The gel thickness is  $h$ ,  $R_{bead}$  the bead radius and  $\sigma_{rr}$  and  $\sigma_{\perp\perp}$  the radial and the tangential component of the stress, respectively. As the actin polymerizes, each actin layer extends from  $R_{bead}$  to the radius  $r$ . Nascent actin layers at the bead surface are not stretched and therefore have no tangential stresses:  $\sigma_{\perp\perp}(r = R_{bead}) = 0$ . Furthermore,  $\sigma_{rr}$  is allowed to vanish at the external boundary of the gel  $\sigma_{rr}(R_{bead} + h) = 0$ . In spherical coordinates the force balance reads:

$$\nabla\sigma(r) = \frac{1}{r^2} \frac{\delta}{\delta r} r^2 \sigma_{rr}(r) + \frac{2}{r} \sigma_{\perp\perp}(r) = 0 \quad \text{Eq. 3-8}$$

The tangential component of the stress can be written down as [66]:

$$\sigma_{\perp\perp}(r) = Y \frac{r - R_{bead}}{R_{bead}} \quad \text{Eq. 3-9}$$

The solution of Eq. 3-8 that accounts for the boundary conditions of  $\sigma_{\perp\perp}$  and  $\sigma_{rr}$  at the inner and outer gel boundary is:

$$\sigma_{rr}(r) = 2Y \left[ \frac{R_{gel}^2}{r^2} \left( \frac{R_{gel}}{3R_{bead}} - \frac{1}{2} \right) - \frac{r}{3R_{bead}} + \frac{1}{2} \right] \quad \text{Eq. 3-10}$$

On the bead surface the gel exerts a stress  $\sigma = \sigma_{rr}(r = R_{bead})$ , given by:

$$\sigma = 2Y \left[ \frac{R_{gel}^2}{R_{bead}^2} \left( \frac{R_{gel}}{3R_{bead}} - \frac{1}{2} \right) + \frac{1}{6} \right] \quad \text{Eq. 3-11}$$

This equation gives the total amount of stress on the bead surface. In an asymmetrical situation the stress imposed on the bead ( $\sigma$ ) would lead to motion, as is the case for *Listeria* bacteria. We also note that the stress depends on the gel thickness ( $R_{gel}$ ) and the curvature of the bead ( $1/R_{bead}$ ).

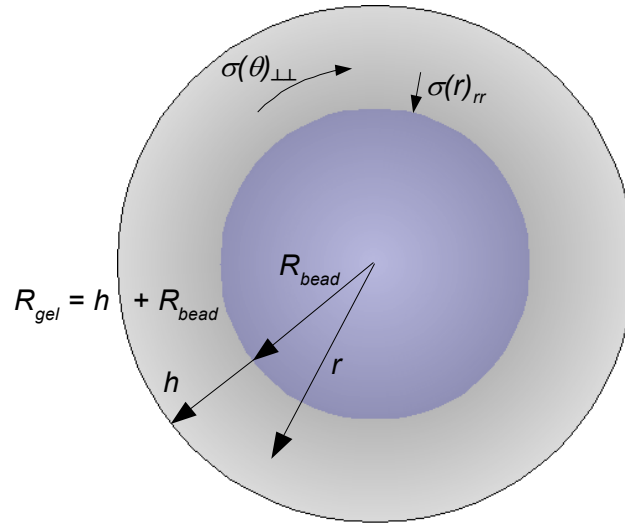


**Figure 3-6** Actin network growth and stress generation on a spherical bead.  $R_{bead}$  is the radius of the bead,  $h$  is the thickness of the gel layer,  $r$  and  $\theta$  are the spherical coordinates.

### 3.5.1 Role of Stresses in *Listeria* Motility

The motility of the *Listeria* bacteria emerging from mesoscopic elastic stress imposed by the actin gel was analyzed by Gerbal et al. [5]. Here we only show the fundamental equations that relate the force generation with actin polymerization based stresses. Generally the force-velocity relation for an actin propelled is given by solving the force balance equation, similar to Eq. 3-4. In the model discussed by Gerbal et al. the generated force is a result of two propulsive contributions,  $f_{mot_1}$  and  $f_{mot_2}$ , and an internal gel-friction force  $f_{fric}$  (see Figure 3-7)

$$f_l = f_{mot_1} + f_{mot_2} + f_{fric}. \quad \text{Eq. 3-12}$$

In the following the origin of the forces will be described only phenomenologically. Their complete derivation can be found in [5].  $f_{mot_1}$  originates from a longitudinal strain (direction of growth) within the actin gel which stems from the fact that the cross section of the bacteria or bead  $S_b$  is smaller than the cross section of the actin tail  $S_t$  (see Figure 3-7A on p.33). The strain arises by latitudinal extension of the comet from  $S_b$  to  $S_t$ , which is associated with longitudinal compression due to volume conservation of the gel. Furthermore, the two cross sections can be related to the velocity of actin gel growth using the total flux of actin gel as  $v_p S_b = v S_t$ , where  $v$  is the velocity of the bacterium and  $v_p$  the polymerization speed. Linear elasticity relates the longitudinal strain ( $\varepsilon_1$ ) in the tail,  $\varepsilon_1 = \sigma_1/Y$ , where  $\sigma_1$  is the longitudinal component of the stress and  $Y$  is Young's modulus.  $f_{mot_1}$  is the force exerted along the direction of comet elongation. The longitudinal (along the comet) component of the stress is therefore  $\sigma_1 = f_{mot_1}/S_t$ . The force velocity relationship for  $f_{mot_1}$  reads

$$\frac{v}{v_p} = \frac{1}{1 + f_{mot_1}/YS_b} \quad \text{Eq. 3-13}$$

The second propulsive contribution in the model  $f_{mot_2}$  is due to a radial stress at the curved surface of the *Listeria* or bead, see Eq. 3-11. This equation is relevant for the gel that grows at the side of the bacterium, which is pushed by polymerization of new actin to become a part of the tail. The elastic energy of this gel adds additionally to propulsion, while the origin of stress and strain

in the tail is due to a bigger external radius of the gel “above” the bacterium as compared to the tail, see Figure 3-7A. An illustrative description of the force generation in this situation would be the “soap effect”, i.e. fast motion of a piece of soap (the bacteria or bead) slipping away as it is slowly squeezed by hand (the actin gel). As for  $f_{mot_1}$  Gerbal et al. assume actin gel volume- and flux conservation and furthermore assume that the speed of the propelled object is approximately to the speed of polymerization ( $v \sim v_p$ ). They find the following force scaling:

$$f_{mot_2} \sim Y S_b \alpha^3 \quad \text{Eq. 3-14}$$

where  $\alpha$  is a dimensionless thickness of the gel ( $h/R_{bead}$ , see Figure 3-6). The internal friction of the gel is described as

$$f_{fric} = -\gamma v_p. \quad \text{Eq. 3-15}$$

The force-velocity curves are given by solving Eq. 3-12, which is done numerically using Eq. 3-13, Eq. 3-14 and Eq. 3-15, the result is shown in Figure 3-7B. In contrast to the “Tethered Ratchet” model the force-velocity curves are much flatter (compare Figure 3-5B, p. 27 with Figure 3-7B, p.33). It takes a much larger force ( $Y S_b \approx 1\text{nN}$ ) to significantly slow down the load in the elastic model compared to the Tethered Ratchet model. This should be mainly due to the absence of the positive feedback between polymerization speed and reduction of  $f_l$  in the elastic model. Rather, the elastic model predicts a self-strengthening of the propulsive force  $f_{mot_2}$  as the external forces  $f_l$  increase. Although,  $f_l$  and  $\gamma$  slows down the bacteria or bead, the gel has time to grow thicker, and a larger stress builds up, which increases the driving force  $f_{mot_2}$ , see Eq. 3-14. This can also be seen in the increasing slope of  $f_{mot_2}$  in Figure 3-7B as  $f_l$  is increased.

The most important aspect of the elastic gel model in actin based motility is that strong antagonistic friction forces are applied on the load ( $f_{fric}$  vs.  $f_{mot_1}, f_{mot_2}$ ) that almost compensate each other. This allows for holding enough propulsive power in reserve as the propelled object encounters increasing external forces  $f_l$ . Some parts of the gel become more compressed and generate an increased driving force in response. The mesoscopic elastic model also

reproduces macroscopic observation such as stick slip motion of mutant *Listeria* and densely NPF coated beads with high degree of branching, see [49, 67, 68]. However, the elastic analysis describes the force generation process on convex-curved surfaces. The question remains, whether this situation is applicable to the process of lamellipodium formation, which occurs at concave-curved surfaces. In this case the “soap effect” would not occur. However, actin polymerization also propels flat or concave surfaces [69]. This implies that the elastic model alone is not sufficient to describe the motion of actin propelled objects, even if they possess a convex shape. On the other hand, the “soap squeezing” effect by the actin gels on convex surfaces definitely exists. The effect was visualized on convex deformable objects like lipid droplets and vesicles (Figure 3-7C). This shows that a significant part of actin gel force generation can be described by the mesoscopic elastic models.



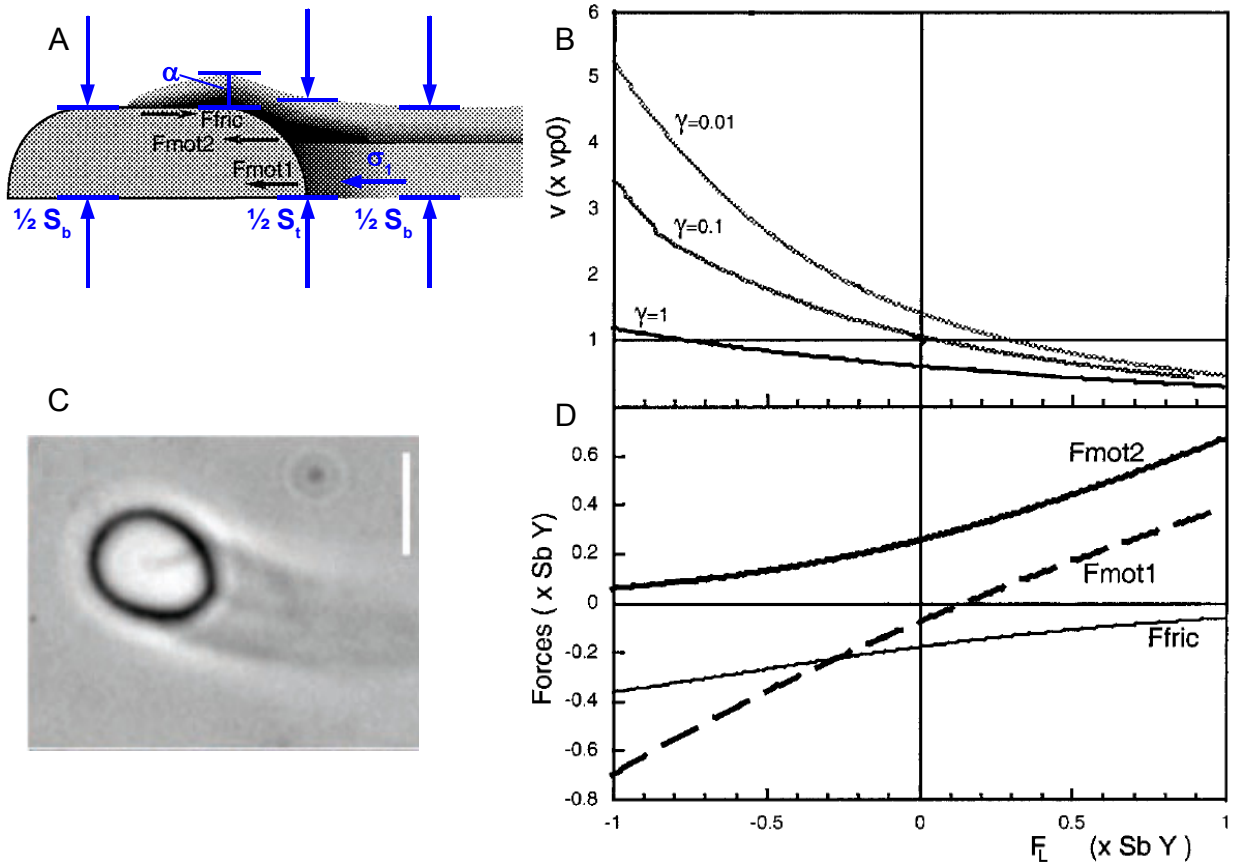


**Figure 3-7** A) Notations for the elastic analysis of *Listeria* propulsion. Note that in spite of the elongated geometry of the bacterium the equations developed in the model are still applicable to the spherical colloids used in this work. B) Force-velocity curve for various values of the friction parameter  $\gamma$ . C) “Soap effect” shown in a deformable lipid vesicle which is squeezed at the attachment site of the actin tail. D) Force exerted by the various parts of the gel on the bacterium versus the external force  $f_i$ . Figures A, B, D were taken and modified from [5], figure C was taken from [50].

### 3.5.2 Effect of Stresses on Gel Growth and Gel Symmetry Breaking

The stress developed by growing actin gels on spherical objects (see Eq. 3-11) was found to affect both, the rate of gel growth and fracture of the gel [6, 26, 27, 70, 71]. Stress induced fracture of the gel is the first step in the formation of an actin comet propelling *Listeria* and NPF coated beads. The gel growth around a NPF coated bead is structured in three phases: First, spherical gel growth; second, gel symmetry break; third, formation of the comet.

**Actin Gel Growth:** In the initial phase, where spherical actin gels grow at the bead, the velocity of gel growth  $dh/dt$  decreases as the thickness of the gel  $h$

increases [71]. The growth velocity  $dh/dt$  can be described by actin polymerization kinetics (see Eq. 3-1) and the filament length increment  $\delta$  by monomer addition:

$$\frac{dh}{dt} = \delta(k_+^b[A_g] - k_-^p) \quad \text{Eq. 3-16}$$

where  $[A_g]$  is the monomer concentration, with  $k_+^b$  and  $k_-^p$  the rate constants for barbed end polymerization and pointed end depolymerization, respectively. The parameters  $k_+^b$  and  $k_-^p$  depend on the stress in the gel, since pulling or pushing forces on filaments change these rate constants [72]. The decrease in growth rate of a spherical actin gel was attributed to two different scenarios: a) growth rate decrease due to diffusion limitation of g-actin to the bead surface [70] and b) stress induced limitation of actin gel growth [6, 71]. Which of the two scenarios is the limiting factor seems to depend on the actual medium composition, degree of NPF functionalization and geometry, i.e. curvature, of the actin gel. The more likely scenario and the physiologically more relevant one is the stress-limited growth [26, 71]. In a first approximation (when neglecting treadmilling), one can state that the polymerization process stops when the chemical energy gain in the polymerization ( $E_{chem}$ ) is balanced by the elastic energy cost for adding a new monomer ( $E_{el}$ ). With  $\xi$  the mesh size of the network and  $1/\xi^2$  the NPF surface density  $E_{chem}$  can be written as  $E_{chem} = \Delta\mu \cdot 1/\xi^2 \cdot 4\pi R_b^2$ . The elastic work for adding a monomer per unit area is  $\sigma_{rr}\delta$ , where  $\sigma_{rr}$  is the radial component of the stress and  $\delta$  the size of a g-actin monomer.  $E_{el}$  can then be expressed as  $E_{el} = \sigma_{rr}\delta \cdot 4\pi R_b^2$ . From Eq. 3-11 Noireaux et al. [6] deduce that  $E_{el} \cong Y(h/R_b^2)\delta \cdot 4\pi R_b^2$ , where  $Y$  is again the elastic modulus of the gel which depends on the density of the gel as well as on  $\xi$  [17]. When no break of symmetry occurs, the actin gel grows into a stationary regime with  $E_{chem} = E_{el}$ , where the thickness of the gel  $h^{max}$  is constant and linearly dependent on the bead diameter  $R_{bead}$ . According to [6] the following equation applies:

$$h^{max} \cong R_{bead} \left( \frac{\Delta\mu}{\delta Y \xi^2} \right)^{1/2}. \quad \text{Eq. 3-17}$$

Eq. 3-17 expresses the fact that the polymerization stops, when the mechanical work required to add a new monomer equals the chemical energy gained in the process. The gel thickness is proportional to the bead radius, which says that steady state is reached at a certain degree of stress in the gel. This value should be dependent on the gel composition which is subject to investigations in this work.

**Symmetry Break Modeling:** The spontaneous break of symmetry that leads to formation of an actin comet was subject to modeling efforts soon after actin growth on artificial beads was established. The acceleration of filament depolymerization as gel generates radial stress was incorporated into these models as a mechano-chemical coupling [26, 41, 73]. When the stress distribution of the entire actin gel is taken into account [26], the mechano-chemical coupling can act as a positive feedback that will ultimately lead to break of symmetry during gel growth: At regions that show lower gel thickness  $h$  the stress in the gel layer is increased. This leads to an increase in depolymerization and further reduction of the gel thickness and ultimately to symmetry break. A prerequisite for this mechanism is a perturbed, non-smooth gel surface. In a nonlinear study of symmetry breaking in actin gels [27] several harmonic modes of perturbations (ripples) on the gel surface were considered. These may arise solely by polymerization of actin and, by of finite element modeling, found to be sufficient to trigger an instability. A result from that work was that the mechano-chemical coupling is not mandatory to create an instability.

**Symmetry Break Experiments:** In-vitro experiments have shown evidence that the actin gel breaks at certain flaws (inhomogeneities) in the gel that inevitably form during polymerization. These flaws may grow inward as the gel grows and form a crack that will finally result in symmetry break [71]. This mesoscopic view is complementary to the theoretic studies mentioned above, as one could interpret a single crack as occurring from a single mode perturbation. In this situation the symmetry break can be discussed using classic fracture mechanics. In engineering science, the resistance of a material to fracture can be estimated by considering the contributions of the energy needed to create a crack, i.e to break the physical bonds between filaments,  $E_{br}$ , and the energy released when the crack is formed,  $E_{el}$  [74]. The amount of the elastic energy released by the presence of a crack is  $E_{el} \propto (\sigma_{\perp\perp}(h)^2/Y)l \propto Yl^3h^2/R_{bead}$ , where  $l$  is the depth of the crack [74]. The energy required for breaking a bond is  $E_{br} \propto l^2\Gamma$ , where  $\Gamma$  is the fracture energy per unit area. The energy change

due to a crack is  $\Delta E(l) = E_{br} - E_{el}$  is function with a maximum at  $l = l^* = Y\Gamma/\sigma_{\perp\perp}$ . For small cracks  $l < l^*$ , crack growth and symmetry break is energetically unfavorable, while for  $l > l^*$  crack growth is spontaneous because  $\Delta E(l)$  decreases with increasing length of the crack  $l$ . As the gel thickness  $h$  increases the critical crack length  $l^*$  decreases. Therefore there exists a critical gel thickness  $h^f$  at which fracture occurs for a typical flaw size  $d$ [71]:

$$h^f \cong R_{bead} \left( \frac{\Gamma}{dY} \right)^{1/2}. \quad \text{Eq. 3-18}$$

If the ratio of Eq. 3-17 and Eq. 3-18 is larger than one  $h^s/h^f > 1$  the actin gel breaks, because the critical stress for fracture is reached before the thickness reaches its homogeneous steady state value. In the force measurements shown in section 5.2 we aim for the other scenario  $h^s/h^f < 1$  in order to not have to deal with the rather unpredictable break of symmetry. Interestingly Eq. 3-17 and Eq. 3-18 are both proportional to  $R_{bead}$ , showing that the symmetry break is insensitive towards the bead size. Rather, the propensity for symmetry breaks depends on by the meshwork size and the number of crosslinks in the network. Both can be controlled by the branching protein ARP2/3, the capping protein and the density of NPF on the bead surface [44, 71].

Up to this point we reviewed the key studies of the field. Most of what has been described will be recalled when discussing of the results of this experimental work. We now turn the focus on the instruments and methods used for conducting the experiments with the actin network.

### 3.6 Microscopy

Although optical magnification via lenses is known for more than 1000 years, optical microscopy is still one of the most important analytical techniques in science. A lot of introductory literature is available (see [75] for a comprehensive textbook), therefore the basic working principles and quantities like magnification and resolution will only be briefly introduced in this section. Contrast enhancing techniques are more relevant for this work as they are needed for the visualization of biological samples. In this work epifluorescence and phase contrast mode were used and will be explained in the following sections.

#### 3.6.1 Light Microscopy Basics

The schematic setup of a transmission light microscope in “Köhler illumination” is shown in Figure 3-8. Also other modes, like epi-illumination or phase contrast utilize and depend critically on Köhler’s type of illumination. [75, 76] Generally, this type of configuration aims for homogeneous illumination of the sample, regardless of the actual light source, which is often a not well defined lamp filament. The light irradiated by the lamp is focused by the collector lens at the front focal plane of the condenser lens, while completely filling the aperture (Figure 3-8). Illumination of the sample is then bright and even. The field diaphragm is used to limit the area of illumination in the specimen to protect the specimen and to reduce the amount of scattered light reaching the eye or detector. The light passing the specimen is then collected by the objective. The objective produces a magnified image of the specimen, which is again magnified by the ocular on the camera or the eye. The magnification of the microscope  $\Gamma_M$  is the product of the magnification of the objective  $\beta_{obj}$  and the ocular  $\Gamma_{oc}$ .

$$\Gamma_M = \beta_{obj} \Gamma_{oc} \quad \text{Eq. 3-19}$$

The second important parameter of a microscope is its resolution, which is also mainly given by the objective. The resolution is defined as the minimal distance at which two points can be observed separately ( $d_{min}$ ). For the microscopy scheme like introduced here, the maximum resolution is diffraction limited and given by the ratio of the wavelength of the light ( $\lambda$ ) and the numerical aper-

ture (N.A.) (Rayleigh limit). The proportionality constant is depending on illumination and is e.g. 0.61 for self illuminating point-shaped objects.

$$d_{min} \propto \frac{\lambda}{N.A.} \quad \text{Eq. 3-20}$$

The numerical aperture can be calculated from the index of refraction of the medium between the objective and the object (in reflection mode the cover slip, respectively) and  $\frac{1}{2}$  of the opening angle of the objective,  $\alpha_{1/2}$ .

$$N.A. = n_m \sin \alpha_{1/2} \quad \text{Eq. 3-21}$$

Therefore, the maximum aperture, depends on the refractive index of the adjacent medium, which means the resolution of oil immersion objectives ( $n_m = 1.45$ ) is even higher than for water immersion objectives ( $n_m = 1.33$ ).

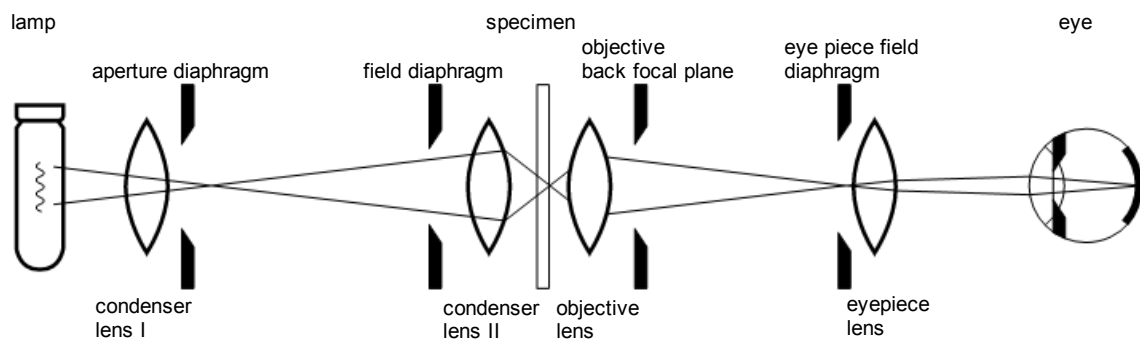


**Figure 3-8** Scheme of a light microscope in transmission mode and the locations of the object focal planes adjusted for Koehler illumination. Image modified from original artwork in [75].

Introductory literature: [75-77]

### 3.6.2 Phase Contrast Microscopy

The eye and CCD cameras detect objects only by their light intensity, or the amplitude of the light the objects irradiate. In optics, contrast is defined as the difference in light intensity between the objects in an image. Owing to the poor contrast of unstained biological samples in liquid, e.g. proteinic structures in cells, they are poorly visible in common bright-field microscopy. However, although these structures are transparent, they can induce a phase shift to a frac-

tion of light that passes them. Unfortunately, the eye and CCD cameras cannot detect differences in the phase. Phase contrast microscopy aims to translate phase changes to large variations in the amplitude. The physical reason for phase shifts in the specimen are optical density gradients which lead to diffraction of light in the sample. The diffracted fraction of the light (D) will be scattered in many directions and has its phase retarded by  $\lambda/4$  with respect to the undeviated light (U), which passes through the sample without interacting with it. Both the U and D light are collected by the microscope optics, will undergo interference, and generate the resulting light (R). Typically only a minority of incident light is diffracted by proteinic objects in aqueous solution. Also, the objects are only detected if the amplitudes of R and U are significantly different. Figure 3-9A shows that the amplitudes differences of R and U depend on the phase difference  $\phi$  and the amplitude of D. Phase contrast microscopy manages to optimize intensity differences between R and U. This is achieved by a) separating the undeviated light U from the most of the diffracted light D so that they occupy different locations at the back aperture of the objective lens, where they are recombined shortly after (Figure 3-9B), and b) advance the phase and reduce the amplitude of the U light, in order to maximize differences in amplitude between the object and background in the image plane. Figure 3-9B and C shows that with a condenser annulus and a phase plate these requirements can be fulfilled. The condenser annulus, a black plate with a transparent annulus illuminates the specimen with a ring of light. In Köhler Illumination the U light then forms a bright image at the back aperture of the objective, while D light is across the entire back aperture. The amount of D light depends on the density and refractive index of light-scattering objects in the specimen. To strongly alter the phase and amplitude of U with respect to the R a phase plate is mounted in the phase contrast objectives, located at or near its back focal plane. The phase plate retards the U light with respect to the D light by  $\lambda/2$  to enhance destructive interference. In addition it attenuates the U light by a semitransparent coating to about 20% intensity to match the intensities of U and D light (Figure 3-9C). Optimizing the phase relations and intensities of U and D for maximum destructive interference results in an increased intensity difference between the R-light and U light. As eyes and cameras interpret contrast as intensity difference, objects with just different optical densities appear with increased contrast.

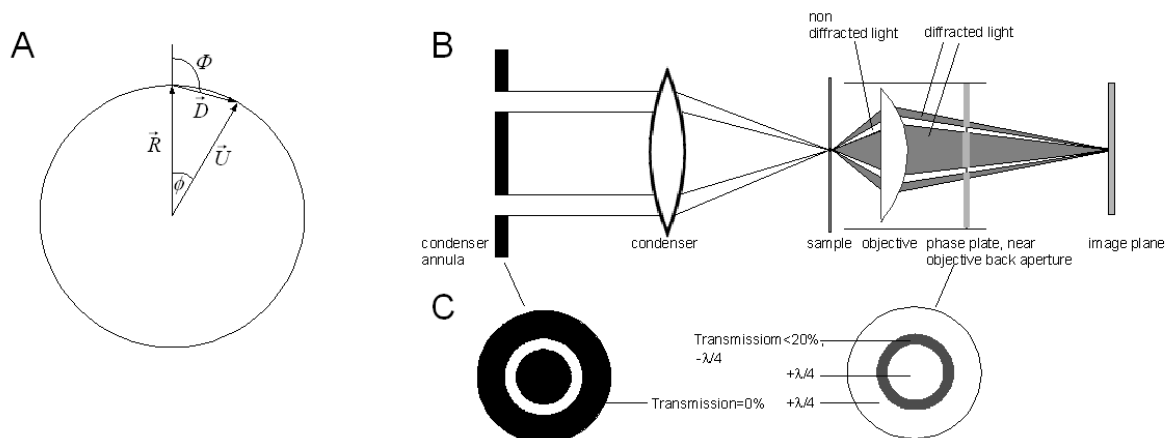


**Figure 3-9** Phase contrast optics: A) Phasor diagram, the electric of  $R$  is shown as the vector sum of the field vectors of  $D$  and  $U$ .  $\phi$  represents the amount of phase displacement. B) Path of the non diffracted and diffracted beams in a phase contrast microscope. The annular aperture in the front focal plane of the condenser generates a hollow cone of light that illuminates the specimen and continues (approximately) as an inverted cone that is intercepted by a phase plate at the back aperture of the objective lens. C) condenser annula and phase plate

Introductory literature: [75, 76]

Specialized literature: [78-80]

### 3.6.3 Fluorescence Microscopy

Instead of using the alterations of light by absorption or phase differences for visualization, in fluorescence microscopy the light emitted by labeled objects is collected exclusively. This has several advantages over conventional types of illumination. Most importantly, fluorescence microscopy allows, visualization of specific molecules that emit light in presence of excitatory light. For this reason fluorescence microscopy has become a versatile technique that allows for special measurements like binding constants and diffusion coefficients using FRAP (fluorescence recovery after photobleaching). Also observation of interaction states and reaction mechanisms are possible with fluorescence energy transfer measurements (FRET). TIRF (total internal reflection fluorescence) and laser scanning techniques allow studying dynamics of single labeled molecules in very thin focal planes.

Compared to other types of contrast enhancing techniques, the process of imaging and image interpretation is often more straight-forward in fluorescence microscopy. However, labeling the specimen with fluorescent dyes is critical,



and has become a science in its own. The physical basis of fluorescence microscopy is the excitation of the fluorophores and subsequent relaxation under emission of photons (Figure 3-10A). Electrons in the ground state  $S_0$  (highest occupied molecular orbital, HOMO) are stimulated by the excitatory light to the first excited state  $S_1$  (lowest unoccupied molecular orbital, LUMO). After electron relaxation to  $S_0$ , light is emitted, with a red-shift (Stokes shift) with respect to the excitatory light. This is due to two reasons. First, only vertical electron transitions are allowed and second, relaxation of the fluorophore's vibrational levels in the  $S_1$  state (Franck Condon principle). In fluorescence microscopes the excitatory light needs to be isolated from the emitted light using a set of interference filters. It is therefore advantageous to use dyes with large Stokes shifts.

Construction-wise a fluorescent microscope shows a number of important characteristics. It has a very intense light source, such as a mercury arc lamp, because only a small fraction of light is suitable for sample excitation. To increase the contrast all fluorescent microscopes are built for epi-illumination, i.e. the objective lens functions both as the condenser, illuminating the specimen, and as the objective lens, collecting the emitted light. This configuration is advantageous because it avoids the strong excitatory beam being directed to the detector (Figure 3-10B). The fluorescence filter set contains three filter sets that further separate the excitatory light from the emitted light: the excitation filter, the dichroic mirror and the emission filter. Finally the fluorescence objectives are optimized as well; they contain low-fluorescent glass and have a high numerical aperture.

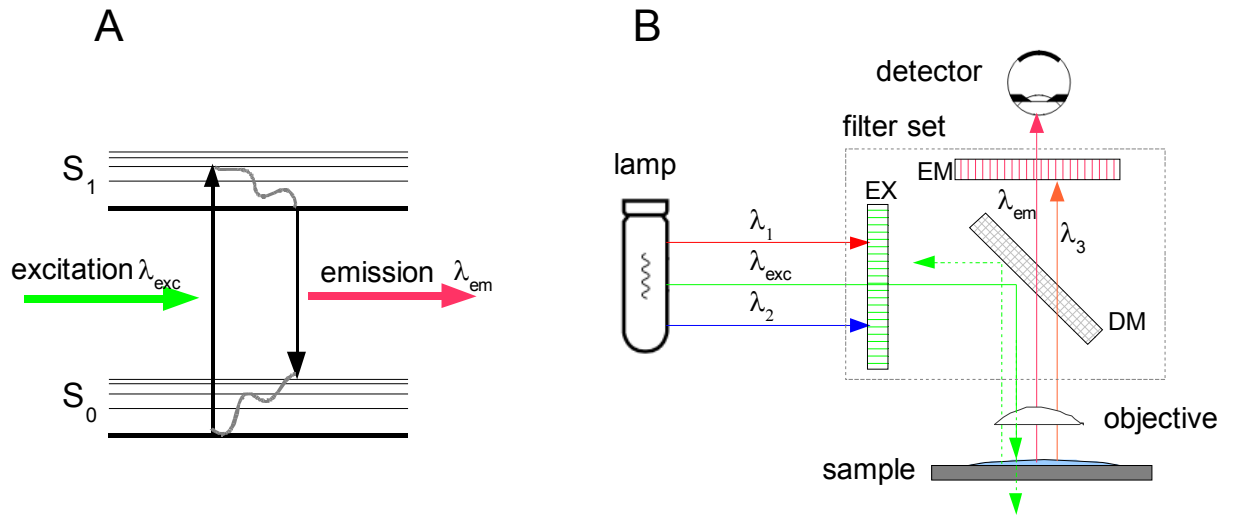


**Figure 3-10** Scheme of the electronic (thick lines) and vibrational (thin lines) energy states of a chromophore. B: Scheme of a fluorescent microscope in epi-illumination. The filter set comprises of an excitation filter (EX), an Emission filter (EM) and the dichroic mirror (DM).

Introductory literature: [75, 76]

Specialized literature: [81]

### 3.7 Atomic Force Microscopy

A very common and intuitive practice to determine forces is measuring the displacement of springs. It was Binnig et al. who invented a method that uses cantilever-shaped silicon springs to apply and measure forces in the nN regime on surfaces [82]. When using a very sharp cantilever tip, the force can serve as a feedback parameter to scan, i.e. to image the surface topography in atomic resolution. The technique is therefore known as Atomic Force Microscopy (AFM), or scanning force microscopy (SFM) for it belongs to the class of scanning probe techniques. In the first publication that presents an AFM as an imaging technique [83], its potential in biological research is acknowledged: *“The applications for the AFM should be quite general. We envision a system that will allow us to study such diverse areas as magnetic materials and biological samples.”* Indeed, its ability to study virtually any kind of solid- or even liquid interface in various media has made AFM one of the most important analytical tools in interface science, for both imaging and force measurements. In biophysics and apart from mere imaging, AFM is mainly used to study interaction forces of bio-macromolecules and mechanical properties of cells and organelles. The latter include for example studies on elastic or adhesion properties of cells and their membranes (see [84-86] for review articles) which are relevant for medical research as well [87]. Prominent examples of AFM force measurements on single molecules include protein unfolding experiments [88], or stretching of bio-macromolecules in general [89]. These studies allow insight in the conformation related energy states of these molecules and their possible biological functions.

Especially in life sciences, there exists a number of complementary methods to AFM as a tool for force measurements. Although the sensitivity is not comparable to AFM, micropipettes are frequently utilized to study mechanical properties of cells [90] and lipid membranes [91]. Here, when handling cells, vesicles or similar objects, the micromanipulation abilities of micropipettes can become advantageous over AFM. In the pN-force range, electric and magnetic field gradients can also be used to generate and measure forces. The corresponding methods are known as optical and magnetic tweezers, respectively. Optical tweezers for example have been utilized for cell sorting according to their size and refractive index [92]. Both optical and magnetic tweezers are often used in single molecule micromanipulation and force single molecule force spectroscopy.

py [93]. A comprehensive comparison between AFM, optical tweezers and magnetic tweezers can be found in [94]. Quite generally one can say that the tweezer-techniques are useful in the lower force regime and offer more degrees of (spatial) freedom for measurements and sample manipulation. Here, AFM is much more limited. Specimens examined with AFM must always be fixed to a solid support or the cantilever. However, AFM works in a broader force range ( $\approx 10 \mu\text{N} - \approx 10 \text{pN}$ ) and offers comparatively simple signal acquisition and data interpretation, as will be shown in the next section.

#### **3.7.1 AFM Working Principle**

The AFM detection system does not measure force directly, but it records the deflection of a flexible cantilever on which the probe is mounted. While the first AFM design [82] uses a STM to measure nm-scale cantilever deflections, today's generic AFMs use an optical lever technique [95]. In this arrangement a small deflection of the cantilever will tilt the reflected beam and change the position of the beam on the photo detector (see Figure 3-11). The AFM works in two fundamentally different modes: First, the imaging mode. The tip is scanned horizontally to the surface, while generating an image from the correction voltage at the z-piezo required to keep the sample-probe separation constant. Second, direct force measurements, which require vertical scanning of the tip relative to the substrate. In this case the signal is the voltage applied to the photo detector due to deflection of the cantilever caused by probe-sample interactions. AFM imaging is not part of this work. However, the components explained in the following are critical for both modes. Figure 3-11 shows the basic components of a generic AFM:

**Cantilever:** The key component of an AFM is the cantilever, the spring. The AFM cantilevers are lithography produced and part of a millimeter-sized on silicon chip that can be exchanged between different AFM experiments. The shapes and dimensions of the AFM cantilever vary with the field of application. Typical dimensions are  $(100-400) \times (20-40) \times (0.5-2) \mu\text{m}$ . Since the dimensions can be easily chosen over large intervals, the spring constants of AFM cantilevers may vary between four orders of magnitude, even for standard cantilevers:  $100 \text{ N/m} - 0.01 \text{ N/m}$ . Sometimes the back of the cantilever is coated with a thin film of reflecting material, in order to improve the reflection of the laser beam.

**Probe:** For imaging AFM the probe is a very sharp tip. Tip cantilever assemblies can be mass-produced with consistently-shaped, very sharp tips (radius between 5-50nm). These tips are integrated at the end of cantilevers which have a wide range of properties, designed for a variety of scanning technologies. Force measurements often use the so called “colloidal probe”. A detailed description of colloidal probe force probes can be found in paragraph 3.7.3.

**Detector:** The position sensitive detector consists of a 4-segmented photodiode. The photocurrents of the detector segments are fed into a differential amplifier. The segments are arranged as shown in Figure 3-11. Usually, when the cantilever is in its equilibrium position, the laser spot is centered at the intersection of the photodiodes. During the measurement, any change in the signal intensity difference between top and bottom segments represents a deflection perpendicular to the surface, the vertical deflection. Changes in the signal difference between left and right segments are due to lateral movement or torsion of the cantilever, the lateral deflection.

**Scanning System:** A fundamental component for AFM as an imaging device is the scanner. Depending on the design, the scanner may move the sample (sample scanning), or it may scan the probe over the sample (tip scanning). To accomplish the precision required, a piezoelectric tube scanner is used and can be controlled to provide subangstrom motion increments.

**Controller:** This unit connects the computer, the scanning system, and the probe motion sensor. It supplies the voltages that control the piezoelectric scanner, accepts the signal from the detector, and contains the feedback control system for keeping the force between sample and tip constant during scanning.

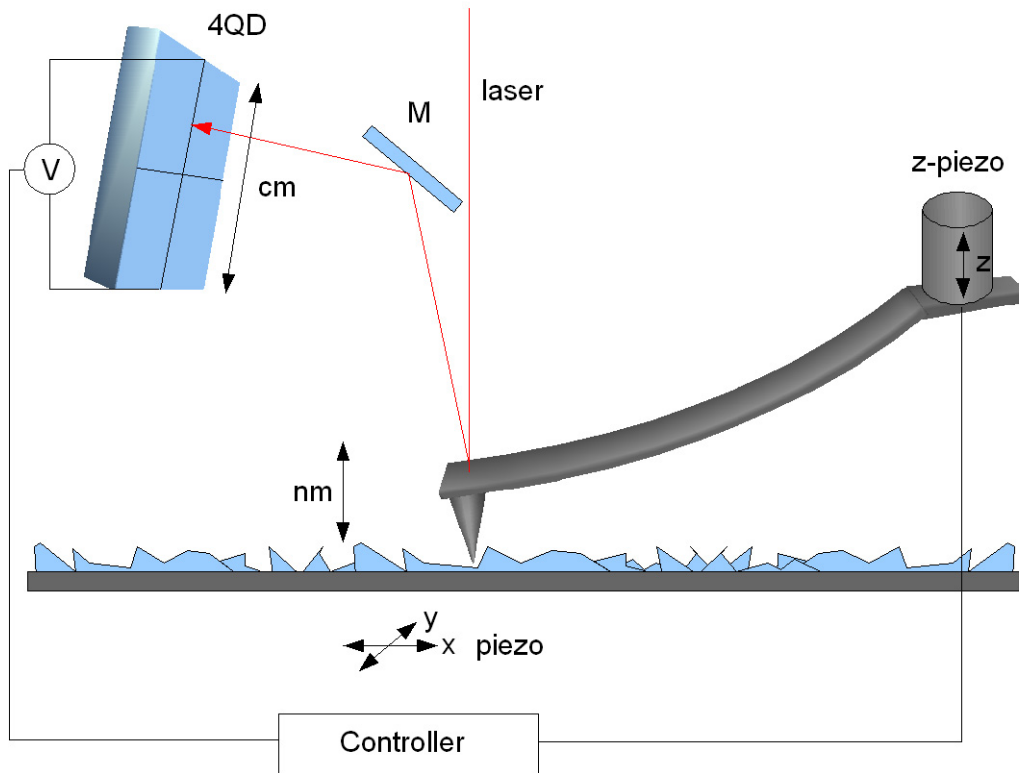


**Figure 3-11** Schematic description of an AFM design. 4QD: four-quadrant photo-diode which produces the raw-signal, M: mirror for positioning the laser on the detector. The optical lever principle allows to measure nanometer meter deflections of the cantilever by translating the cantilever deflection to large shifts of the laser spot on the photodiode.

Introductory literature: [96, 97]

Specialized literature: [98, 99]

### 3.7.2 AFM Force Measurements

The main part of this work deals with the measurement of force by expanding actin gels. The type of AFM experiment that allows insight in the forces generated by the actin system differs from conventional AFM force measurements in some ways. The first conventional AFM force measurements, also known as ‘force spectroscopy measurements’, were published in 1989 [100]. A major part of AFM force measurements is dedicated to study interaction forces of interfaces. These will only be discussed briefly, because the measurements performed here deal with the micromechanical analysis of colloidal objects, in which interfacial forces are not sensed deliberately. AFM mechanical studies have been done on numerous colloidal objects e.g. cells, thin films or artificial

capsules [99, 101, 102]. In this mode usually force-displacements curves, i.e. a plot of the applied force versus the probe-sample distance, are recorded. In the following we discuss the acquisition of such a plot and its meaning from a general viewpoint. In order to obtain a force displacement curve, the probe (or the sample) is displaced along the vertical axis, while the cantilever deflection  $C$ , as well as the z-piezo position is measured. To study mechanical material properties, like the sample spring constant  $k_d$ , it is required that the force imposed by the AFM probe actually deforms the sample. The force acting on the AFM cantilever  $F_c$ , is described by Hooke's law:

$$F_c = k_c C \quad \text{Eq. 3-22}$$

where  $k_c$  is the spring constant of the cantilever. Upon approaching the sample the probe will impose a force and a sufficiently compliant sample will deform by  $\delta = D_0 - D$  (Figure 3-12). Where  $D_0$  is the thickness of the uncompressed sample and the  $D$  thickness upon compression. The only distance that is controlled or measured in a force-displacement experiment is the z-piezo position and the cantilever deflection  $C$ . The sample deformation  $\delta$  can be calculated with  $C$  and with the z-piezo shift  $Z_D$ .  $Z_D$  is the z-piezo movement after first contact with the sample,  $Z_D = Z - Z_{contact}$ , where  $Z$  is the final approach position and  $Z_{contact}$  is the z-position at which the probe touches the surface only very slightly. The sample deformation then reads

$$\delta = D_0 - D = Z_D - C. \quad \text{Eq. 3-23}$$

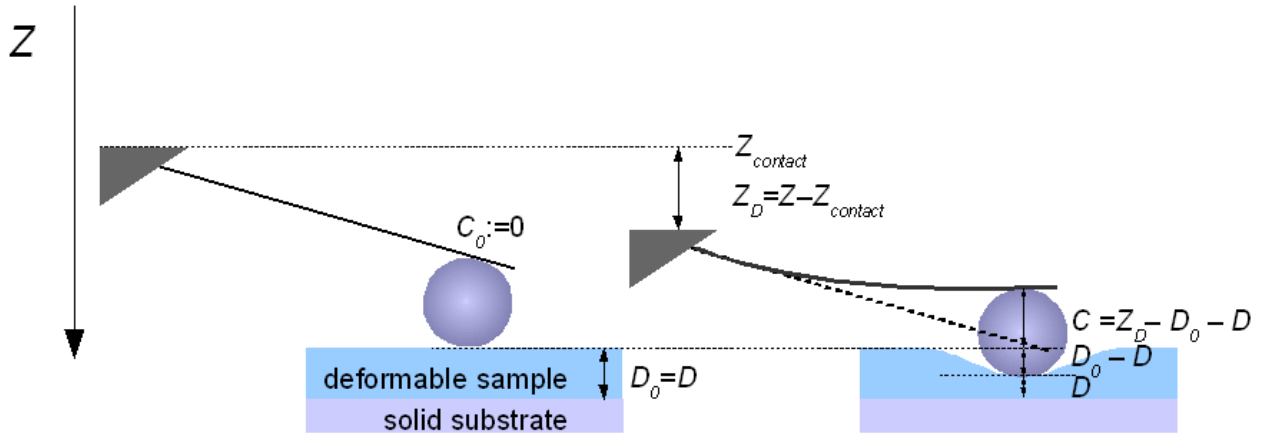


**Figure 3-12** The probe-sample system: Deformation and lengths upon deformation of the sample.  $Z$  is the vertical coordinate that is controlled by the  $z$ -piezo.  $D$  is the thickness of the soft sample

An AFM force-displacement curve reflects of two contributions: the tip-sample interaction and the spring force of the cantilever. This is schematically depicted in Figure 3-13A. Here the curve  $F(D)$  represents the tip-sample interaction force. At this point we assume a simple mechanical spring potential for the sample that is compressed by the AFM probe,  $V(D) = 1/2 k_D \delta^2$ , hence  $F(D) = k_D \delta$ . Note that the potential functions are usually more complicated in reality. The straight lines represent the elastic force of the sample  $F(D)$  and cantilever as expressed in Eq. 3-22. Upon driving the probe further down after probe-sample contact, the sample generates the restoring force  $F(D)$ . In mechanical equilibrium the total force acting on the cantilever is zero. That means for each piezo displacement  $Z$  the cantilever is deflected until the elastic force of the cantilever equals the tip-sample interaction force, that is:  $F_{total} = F(D) + F_c = 0$ . In equilibrium of forces and with a deformation of the sample  $\delta$ , plus a given cantilever deflection  $C$ , we can therefore write the basic equation of AFM force measurements:

$$F(D) = -F_c = -k_c C = -k_c (Z_D - \delta) \quad \text{Eq. 3-24}$$



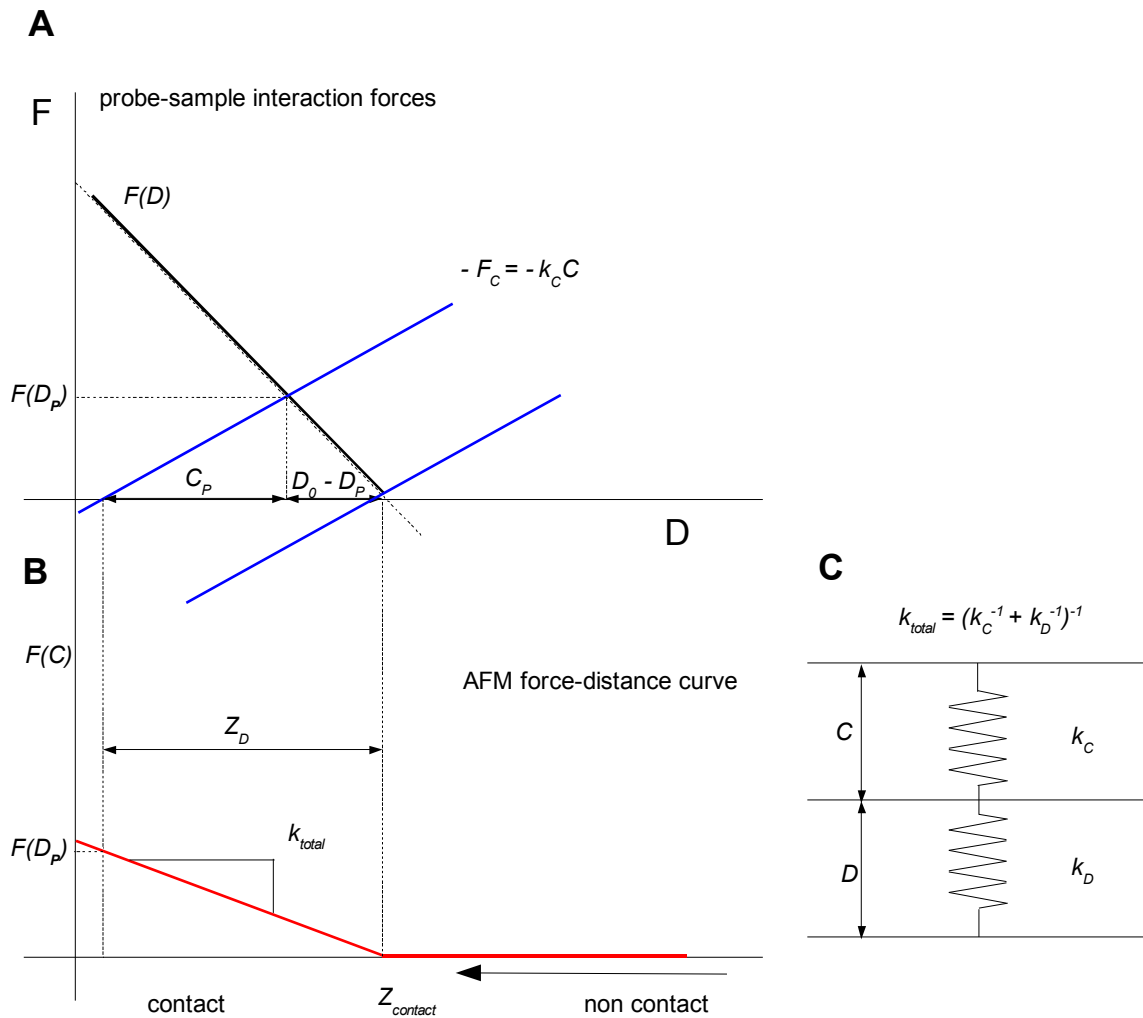


**Figure 3-13** A) The cantilever deflection  $C$  is, at every position, the result of two contributions: the probe-sample interaction  $F(D)$  (black curve) and the elastic force  $-F_c$  (blue line). In force balance, the two forces must compensate and give  $F_{total} = F(D) + F_c = 0$ . For an arbitrary intersection point P of  $F(D)$  and  $-F_c$ , there exists a deflection  $C_P$  and  $\delta_P$ , which represent the elastic force of the cantilever and sample. Both  $C_P$  and  $\delta_P$  are given by difference of the force curve intersections with the axis  $F = F_{total} = 0$  and  $Z_D$ . B)  $Z_D$  is the z-piezo motion to any equilibrium point (P in this case) after probe-sample contact at  $Z_{contact}$ . The graphical reconstruction shows the respective experimental force-displacement curve. C: The intersection of the force curves in A) can be seen as the combination of two springs of length  $C$  and  $D$  which is the thickness of the deformable sample. The total spring constant  $k_{total}$  can be calculated accordingly and is found the slope of the experimental force curve.

Force balance is given by the intersection points of  $F(D)$  with  $-F_c = -k_c(Z_D - \delta)$ , see Figure 3-13A. The relation between the tip-sample interac-

tion and the resulting deflection-displacement curve measured with AFM is shown by the graphical reconstruction in Figure 3-13B. The representative force curve shows that the sample is first approached by the probe ( $F=0$ ), then contact is made at the  $z$ -position  $Z_{contact}$ . Now, the two quantities recorded by an AFM are  $Z_D$  and  $C$ , while force balance is always given. Reading these two parameters allows calculation of the sample deformation  $\delta$  by using Eq. 3-24. As a prerequisite the spring constant of the cantilever has to be known, which is the case after calibration the cantilevers with for example the Sader [103] or thermal noise method [104]. For the simple elastic spring potential discussed here, knowledge of the sample deformation would directly lead to the apparent spring constant of the sample  $k_D$ . The total spring constant is represented as the slope of the force-displacement curve in Figure 3-13B. The graphical reconstruction descriptively shows how changes in the spring constants change the resulting deflections/deformations of the probe and sample as well as the slope of the force displacement curve.

A next step in the AFM force measurement procedure is relating the applied force with the sample deformation. With the appropriate model one obtains the mechanical properties of the sample, e.g. the elastic modulus of the material. This is a critical part in an AFM force measurement. Contradictory to the simple example shown in Figure 3-13, the force curves are in general not linear, already because the probe-sample contact area is changing as the sample deforms. For a perfectly elastic and planar sample that is deformed by a spherical probe the AFM experiments can be described by the Hertz model [99]. In any case, analysis of the force curves requires geometrical control of the probe – sample contact. In order to exclude uncertainties due to the probe geometry or the tilt angle between sample and cantilever, spherical colloidal probes (see paragraph 3.7.3) are very frequently used as AFM force probes. For the sake of simplicity the discussion of the force-displacement curves covered only the elastic forces of the probe and the sample. Typically there are a number of other sample-probe interactions, such as adhesion forces, that can be studied using with AFM force-displacement curves

#### **3.7.3 The Colloidal Probe**

In order to eliminate the problem of the unknown shape of the AFM probe, modified cantilevers with probes well of known, mostly spherical, geometry are used. This technique uses a custom probe of colloidal size attached to the apex

of the cantilever and is therefore known as colloidal probe technique. Colloidal AFM probes were introduced by Ducker and Butt in 1991 [105], and have since then been widely employed in AFM force measurements. The cantilever modification merely consists in gluing the colloidal probe at the end of a cantilever by means of epoxy resin, surface-melting or sintering. The radius of colloidal probes is on the order of 2-50  $\mu\text{m}$ . The size of the colloidal probe can be determined using optical microscopy, or when the radius and surface condition needs to be known precisely, via electron microscopy, see Figure 3-14. The advantage of this technique lies in the exact knowledge of the probe geometry and its increased sensitivity towards interfacial forces. In this work we use colloidal probes due to its well defined geometry and also exploit the ease of controlling the probe's surface chemistry.

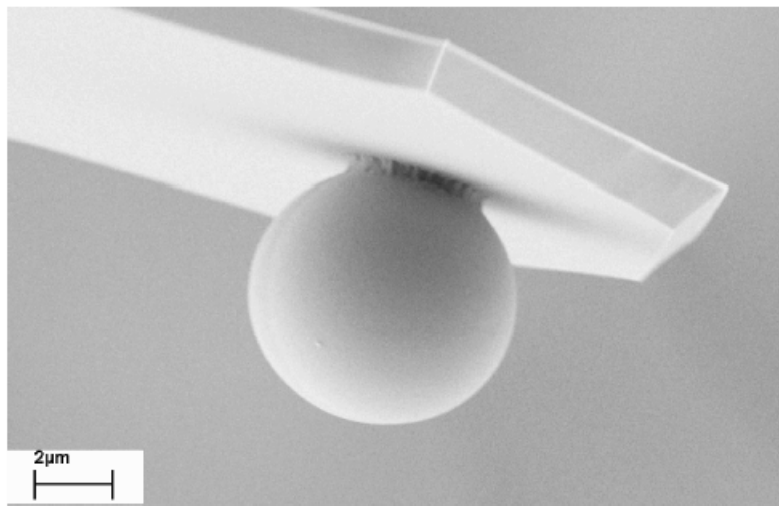


**Figure 3-14** Scanning Electron Microscopy image of a colloidal probe. Silica bead attached to an AFM cantilever using epoxy glue. The Image was taken from [106].

## 4 Preparation Procedures

### 4.1 Preparing the Actin In Vitro Medium

In the following the protein preparation and purification procedures will be shortly illustrated. Then, the different buffer systems and the preparation the actin medium will be explained. These procedures were conducted prior to the force and motility measurement in the actin in vitro medium.

**Actin:** Actin was purified from rabbit muscle according to the protocol by Spudich and Watt [107]. First 10 g of a powder-like acetone raw extract from the rabbit back and leg muscle is prepared. The powder was further extracted in Tris-Cl buffer (2mM Tris-Cl, 0.2 mM ATP, 0.5 mM  $\beta$ -mercaptoethanol, and 0.2 mM  $\text{CaCl}_2$ , pH 8.0) and coarsely filtered. The supernatant fluid was then centrifuged at 10.000g for one hour to obtain a clear solution. From this solution, the actin was allowed to polymerize by adding KCl to obtain 0.05 mM and  $\text{MgCl}_2$  to obtain 0.002mM in the solution. The following steps are identical to the actin cleaning procedure (centrifugation, pellet cleaning, and depolymerization see appendix 8.3).

Fluorescent actin was labeled with rhodamine-NHS (CAS Number [114616-32-9](#)) according to [108]. Rhodamine-NHS binds to lysines in the actin molecule. Labeling the actin with rhodamine-NHS heavily interferes with its polymerization properties. Therefore the degree of labeling was rather low, typically 0.8-1.2 lysines per actin molecule. The labeling reaction was performed in 50 mM PIPES buffer (pH 6.8), 50 mM KCl, 0.1 mM  $\text{CaCl}_2$ , 0.2 mM ATP, 0.3 mM rhodamine-NHS and 40-60  $\mu\text{M}$  F-actin. The degree of labeling was controlled by UV-VIS using the decrease of rhodamine-NHS absorbance at 567 nm, which occurs upon reaction with lysine. The reaction was stopped by adding excess of lysine if the desired degree of labeling was reached. The actin was then purified according to the protocol shown in appendix 8.3.

All g-actin solutions in were prepared and purified in M.-F. Carliers lab (LEBS-CNRS, 91198 Gif-sur-Yvette, France). The g-actin solution must not be frozen but kept on almost 0°C. Therefore, after shipping on ice, the g-actin solution was always stored on ice in a refrigerator. The g-actin buffer is termed “g-buffer” and contains ions that prevent actin polymerization (see subsection “buffers”). G-actin older than two month was either purified (see appendix 8.3) or replaced by freshly prepared actin.

**Supplementary Proteins:** Profilin was purified from bovine spleen [109]. Arp2/3 complex was purified from bovine brain [110] and for some experiments labeled with Alexa-488 maleimide. Human His-tagged N-WASP was expressed in Sf9 cells using the baculovirus system [110]. All proteins were stored at  $-80^{\circ}\text{C}$  in 5-10  $\mu\text{l}$  aliquots. After melting, the protein aliquots were used for one week at maximum. All the supplementary proteins were also a gift from the M.-F. Carlier lab and shipped on dry ice ( $-78^{\circ}\text{C}$ ).

**Buffers:** The actin medium consists of rather complex buffer media. The medium in its final state is a mixture of three buffer systems called “f-buffer”, “x-buffer” and “mix-buffer”, see Table 4-1. The f-buffer is nothing but the stock solution of g-actin (in “g-buffer”) that has been supplemented with KCl and  $\text{MgCl}_2$  and EGTA. In the f-buffer, g-actin is allowed to polymerize to form f-actin. This is because of the combined effects of removing calcium ions with EGTA and adding  $\text{Mg}^{2+}$  and ATP [10]. The mix-buffer additionally adds an oxygen scavenger (DTT), photo bleaching inhibitor (DABCO) as well as ATP and  $\text{Mg}^{2+}$ . The x-buffer is used to adjust the final concentration of actin and the supplementary proteins and also contains bovine serum albumin (BSA) to avoid non-specific protein interactions.

Since all actin assays start from a stock solution of actin in g-buffer, only the x-buffer and the mix-buffer have to be prepared prior to an experiment. Additionally, a solution of KCl,  $\text{MgCl}_2$  and EGTA has to be prepared to transform the g-buffer into an f-buffer. The exact final composition depends on the amount of supplementary proteins that are added for completing the medium. ATP,  $\text{Mg}^{2+}$ , DTT and DABCO concentrations may therefore vary, but this does not affect the actin polymerization. The composition of the buffers is shown in the table below.

#### 4. Preparation Procedures

<i>g-buffer</i>	<i>f-buffer</i>	<i>x-buffer</i>	<i>mix-buffer</i>	<i>final</i>
(g-actin stock solution)	(f-actin stock solution)			after adding all proteins
5 mM TRIS-HCl pH7.8	4.75 mM TRIS-HCl pH7.8	10 mM HEPES-NaOH pH7.8	24 mM MgCl <sub>2</sub>	pH 7.8
1 mM DTT	0.95 mM DTT	0.1 M KCl	12 mM ATP	0.1 M KCl
0.1 mM CaCl <sub>2</sub>	0.095 mM CaCl <sub>2</sub>	1 mM MgCl <sub>2</sub>	40 mM DTT	4-5 mM MgCl <sub>2</sub>
0.2 mM ATP	0.19 mM ATP	0.1 mM CaCl <sub>2</sub>	0.88 mM DABCO	2-3 mM ATP
0.01 % NaN <sub>3</sub>	0.009 % NaN <sub>3</sub>	1 mM ATP		≈6.7 mM DTT
	0.1 M KCl	10 mg/ml BSA		≈0.15 mM DABCO
	1 mM MgCl <sub>2</sub>	0.01% NaN <sub>3</sub>		≈5 mg/ml BSA
	0.2 mM EGTA			≈0.05 mM CaCl <sub>2</sub>
				≈0.005% NaN <sub>3</sub>
				<0.024 mM EGTA

**Table 4-1** Buffers composition and auxiliary components used for the actin polymerization medium.

Some details on the buffer stability: In liquid condition, the mix-buffer can only be stored for three days, as it contains DTT and DABCO which are reactive and decaying in solution. ATP, DTT, and DABCO solutions in water can be stored at -20°C for several months. After re-melting the frozen aliquots of ATP, DTT and DABCO, the mix-buffer was prepared. The x-buffer solution is used for one week at maximum. After one week a fresh x-buffer solution was prepared.

**Actin medium, final preparation:** For the sake of simplicity, it is sufficient to work with a fixed *total volume* of the medium (usually 24-48 μl).<sup>1</sup> This determines the amount of g-actin stock solution from which the final preparation

<sup>1</sup> As the added amount of the protein stock solutions vary, the concentrations of e.g. ATP and MgCl<sub>2</sub> also varies in the final mixture (see Table 4-1) but the effect on the network polymerization is negligible.

procedure starts. To obtain a reproducible behavior of the motility medium, the g-actin stock solution has to be supplemented with the auxiliary components always according to the same protocol. The three major steps in the protocol are:

**Step 1:** About one hour before the experiment a solution of KCl and MgCl<sub>2</sub> and EGTA were added to the g-actin solution to obtain an f-actin solution in f-buffer. With filamentous actin a constant pool of g-actin is available during the assay because of constant depolymerization of f-actin.

**Step 2:** Preparation of the “mix-buffer” such, that after addition of the mix buffer to the f-actin solution the desired amount of ATP, MgCl<sub>2</sub>, DABCO and DTT is reached in the final mixture.

**Step 3:** In the third step, the supplementary proteins are added. Here the concentrations vary for the individual experiments. Table 4-2, Table 5-2, Table 5-4 and Table 5-6 show the respective preparation conditions and the concentrations. The final volume (...and concentrations) is adjusted by adding x-buffer. Usually one half of the total medium volume stems from the x-buffer addition.

***Bead functionalization:*** To allow for actin recruitment on bead surfaces, the beads have to be functionalized with N-WASP. The following text depicts the corresponding protocol. Carboxylated polystyrene beads of different sizes (2-20 μm, Polybeads®) were obtained from Polysciences (Eppelheim, Germany). The carboxylated bead surface allows physisorption of N-WASP and formin (NPF). The NPF solution was diluted to the desired final concentration, usually 25 μl, with x-buffer. Then the bead stock solution was added, which contains 2.5 wt% beads (value given by the manufacturer). The final concentrations of beads and NPFs is specified for the individual experiments, see sections 4.2, 5.2.2 and 5.2.3. After dispersing, the beads were incubated for 60 min in the NPF solution at 4°C and under continuous agitation. After adding a 10 mg/ml bovine albumin serum (BSA) solution in x-buffer, the NPF-bead mixture was incubated for another 15 min in the 1 mg/ml BSA containing solution. The beads were centrifuged and washed to remove the NPF. The beads were then re-suspended in 0.1 mg/ml BSA in x-buffer. Generally, BSA is added to avoid un-specific interactions of the bead surfaces. The beads were stored on ice for one week maximum, without any noticeable changes in their behaviour.

## ***4.2 Preparation of the Bead Trajectory Assay***

## 4. Preparation Procedures

---

After preparing the actin medium and the N-WASP coated beads (see previous section) the trajectory or force assay can be initiated. Here we explain the preparatory steps for the trajectory assay starting with the exact composition of the motility medium for these experiments. Also the optical microscope and the preparation of the different bead motility cells will be explained.

**Motility Medium:** In this study the medium composition is not varied, except for the polystyrene particle sizes. To account for variations of the bead surface area, the volume of beads was adjusted so that the total solid surface area remained constant. This ensures that the N-WASP density on the surface is identical between beads of different sizes. Table 4-2 lists concentrations of the motility proteins for the bead trajectory assay. In this experiment methyl cellulose (CAS 9004-67-5; Sigma-Aldrich, Steinheim, Germany; 4000 cP in 2% aqueous solution at 20°C) was added to avoid Brownian motion of the beads, which would otherwise superimpose to the primary actin based motion.

bead preparation			medium composition (proteins, methyl cellulose)					
N-WASP	PS-beads		f-actin	ADF	profilin	gelsolin	ARP2/3	meth. cell.
concentration	$2.5 \times 10^9$	$\mu\text{m}^2/\text{ml}$	7 $\mu\text{M}$	9 $\mu\text{M}$	2.4 $\mu\text{M}$	0.1 $\mu\text{M}$	0.1 $\mu\text{M}$	0.2 mg/ml

**Table 4-2** Actin medium composition for the bead assays. The composition is optimized for fast motility of the beads [12]. The bead preparation column shows the N-WASP concentration and “concentration” of the bead surface during activation of the bead surface. The medium composition column only shows the concentration of the proteins. The bead concentration was adjusted according to the specific experiment, i.e. larger concentrations for smaller beads, for example.

**Setting up the microscopy study:** Before tracking the actin propelled beads, the measurement cell, which is the medium chamber the beads move in, has to be prepared carefully. Usually proteins interact with surfaces nonspecifically, i.e. they may bind to the surface and lose their function. Therefore, in vitro glassware is coated with bovine serum albumin (BSA) to passivate the glass surface to minimize unspecific protein interaction. Before adding the actin medium solution to the microscope glass slides, the slides were washed and coated with 1 mg/ml BSA solution. A droplet of the BSA solution was left on the glass surface for about 10 min to allow for BSA adsorption. Then, a 5  $\mu\text{l}$  (for the 6  $\mu\text{m}$  beads) or a 3  $\mu\text{l}$  (2 and 3  $\mu\text{m}$  beads) droplet of the motility medium was spread between the object slide and a 20 x 20 mm coverslip. The heights of the



liquid volume were then 12.5 and 7.5  $\mu\text{m}$ , respectively. That is, the beads are allowed to move in a quasi 2d geometry. To avoid evaporation, the glass coverslip was sealed with VALAP at 70°C (vaseline, lanolin, paraffin / 1:1:1). VALAP forms a solid wax at room temperature around the edges of the coverslip, which ensures that the cell is completely sealed.

Optical microscopy was performed on an inverted Zeiss Axiovert200 using phase contrast optics, a 20X objective (N.A. 0.75) and an AxioCam HRm camera. Images were captured at 30 sec intervals for approximately 8 hrs, at room temperature. Over that period the bead velocity gradually goes down by a factor of 1.5 to 2. This is most likely due to changes in the motility medium, probably due to consumption of ATP, unspecific protein interaction or denaturation.

**Structured substrates:** The micro channel structures were fabricated by casting an elastomer precursor in a photolithographic mold and curing. Prior to the casting process the photolithographic molds (GeSim, GroBerkmannsdorf) were hydrophobized with a fluorinated silane (Heptadecafluoro-1,1,2,2-tetrahydrodecyl)dimethylchlor, ABCR GmbH, Karlsruhe, Germany). The silane was deposited by vacuum on the mold in an exsiccator for 24 hours. After deposition the molds were rinsed with isopropanol. Next, the elastomer polydimethylsiloxane (PDMS) Sylgard 184 (Dow Corning, Wiesbaden), with a polymer-crosslinker ratio 10:1, was deposited on microscope slides. After that the mold were pressed on the PDMS covered slides so that all air bubbles are pressed out of the PDMS precursor mixture between the slide and the mold. When applying vacuum, remaining air bubbles can be removed. The PDMS was then cured by heating to 65°C for 4 hours. After peeling from the mold, the PDMS structures were plasma treated to ensure complete wetting of the surface with the aqueous motility solution. For the same reason the structured surfaces were not treated with BSA, unlike to the smooth glass surfaces.

### **4.3 Force Assay Preparation Procedures**

Standard AFM procedures had to be adjusted in order to allow for reproducible force measurements with the complex behavior of the actin in-vitro medium. Here we present a method that allows for controlled actin gel growth at the apex of a cantilever and quantitative force measurements on the expanding actin gel. Several other methods were tested in this work giving additional in-

formation on the behavior of the gel for different force probe geometries and surface chemistry (see section 5.2.1). The biggest challenge for controlled experiments is to restrict actin the actin gel growth to the tip of the cantilever. One possible way is to limit the surface deposition of nucleation promoting factors (NPFs) to the probe at the tip of the cantilever. In standard applications such a spatially limited surface modification this is not needed. Usually the whole AFM chip with the force probe can be functionalized, without affecting its behavior during measurement. In this case all parts of the cantilever that contain NPFs would initiate gel growth which makes the force measurements hard to interpret. We tested a number of possible procedures that ensure spatially limited actin gel growth at the cantilever. Others used the controlled flow of micropipettes to activate the bead attached at the force probe only [55]. A method that allows actin gel growth confined to the AFM colloidal probe will be shown in the following, as well as other steps in the force measurement procedure.

***Actin Medium:*** For the force measurements, the bead size as well as the protein composition in the medium were varied. Apart from that the medium was prepared as described in 4.1. The protein concentrations are specified in the respective result sections (see 5.2.1- 5.2.3). During bead functionalization, the amount of beads was adjusted such that the total surface of solid per unit volume of solution was always  $1 \times 10^9 \mu\text{m}^2/\text{ml}$ , independent of the diameter of the beads. This ensures that the NPF density on the surface is identical between beads of different sizes. The N-WASP concentration was adjusted to  $0.5 \mu\text{M}$  during bead functionalization.

***Force Probe Preparation:*** AFM cantilevers with a nominal spring constant of  $0.03 \text{ N/m}$  were obtained from  $\mu\text{Mash}$ , Estonia. In order to avoid signal drift associated with protein adsorption, only uncoated cantilevers were used (termed “CSC12 no Al”). The measurements were performed on a “Nanowizard I” AFM (JPK Instruments AG, Berlin, Germany) in a liquid cell (“Small Cell”) by the same company. The AFM is combined with an optical microscope Axiovert 200 (Carl Zeiss AG, Germany), which allows fine position control when maneuvering the cantilever during the preparation. Before mounting the liquid cell on the AFM, the glass slide bottom of the liquid cell was dipped into a solution of  $10 \text{ mg/ml}$  BSA to passivate the glass surface. The spring constants of the cantilevers were determined using the thermal noise method [104] or the Sader method [103]. Both methods agreed within 10%, and values of the spring constants were in the range reported by the manufacturer. After cantilever calibration, the

tip of the AFM cantilever is dipped into fast curing epoxy (UHU Barbed endfest 300, UHU GmbH & Co.KG, Germany). Due to the small time frame given by epoxy glue, which hardens within 10 min, the cantilever chip was mounted in the liquid cell already before dipping the cantilever into the epoxy glue. (The procedure of mounting the liquid cell and cantilever into the AFM head would take too much time and the glue would be hardened before bead attachment.) This also means that all cantilever maneuvering has to be done manually with the AFM stage. This however can be done in sufficient ( $\mu\text{m}$ -) precision. Next, the NPF-functionalized beads in buffer suspension (usually 25  $\mu\text{l}$ ) were added to the liquid cell. The beads were then allowed to sediment to the glass cover slide bottom of the liquid cell. Next, using the AFM software-controlled stepper motors one of the sedimented beads was attached to the tip of a cantilever in liquid (Figure 4-1). After complete hardening of the epoxy glue the optical lever sensitivity [99] is determined.

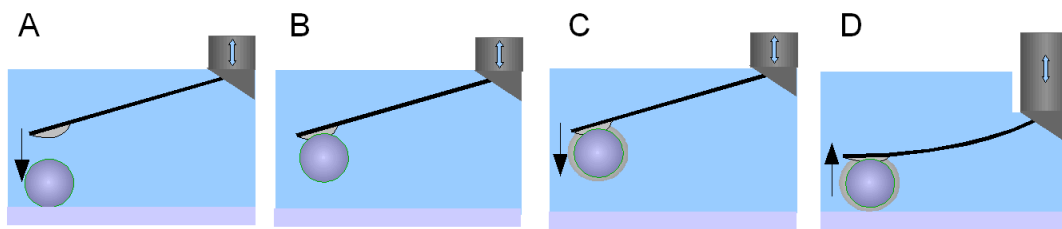


**Figure 4-1** Initiation of a force measurement. A) Bead (NPF coated) attachment to the tip of an AFM cantilever with epoxy in the bead suspension. B) Retraction of the cantilever as the bead is adhered to the cantilever, curing of the epoxy and optical lever sensitivity determination C) Addition of the actin medium, initiation of the gel growth, approach to the surface D) After reaching the setpoint (preset cantilever force) the height is held constant

It should be noted that this process does not require removing the NPF coated force probe out of the buffer. More common colloidal probe attachment procedures are performed externally with a micromanipulator, and not directly in the AFM fluid cell. The crucial flaw in the common procedure is that the colloidal probe inevitably dries when changing the AFM chip from the micromanipulator to the fluid cell. We observed that upon drying the highly functional NPF bead surface is spoiled, so that it does not recruit actin anymore.

**Force Measurements:** After curing of the glue and determination of the sensitivity the actin medium was injected into the liquid cell using a microliter syringe. Figure 4-2 show a picture of the measurement setup with the actin me-

dium injection method. The syringe with the actin medium was directly inserted into the liquid cell. This ensures that dead volume of the liquid cell tubing is minimized, which allows to work with very small volumes in the cell (48  $\mu\text{l}$  in total). The volumes of the actin medium in the syringe and in cell (the bead suspension) were adjusted such, that the desired concentration of the components (actin and auxiliary agents) is reached in the liquid cell (see Table 5-2. After two minutes waiting for thorough mixing and equilibration the colloidal probe was approached to the surface. With the AFM feedback controls an initial force of 5 nN was applied on the colloidal probe. The force data collection is started thereafter with the z-piezo position kept at constant height (closed loop enabled).

**AFM head in measurement position**

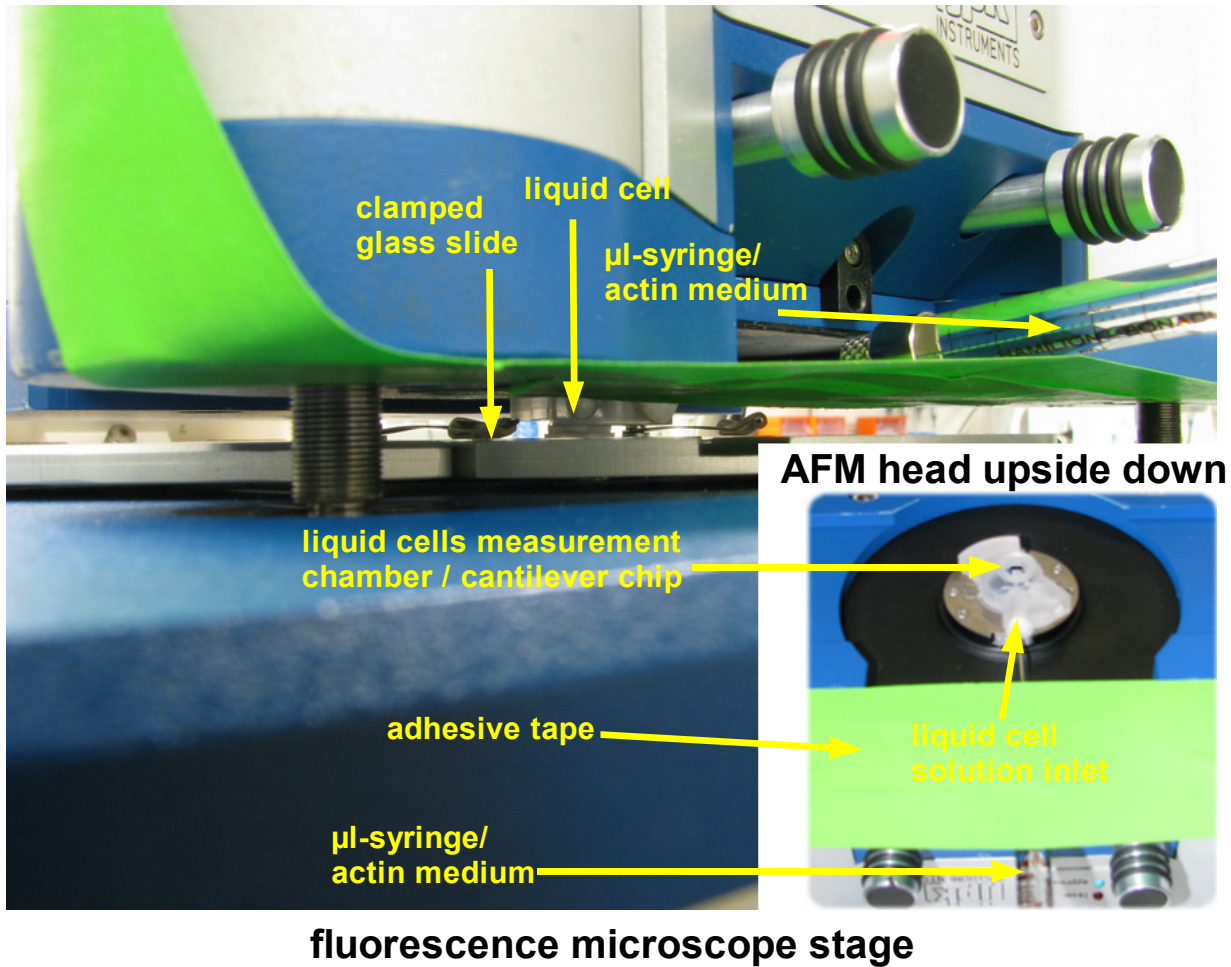


**Figure 4-2** Picture of the setup in measurement position and in liquid cell mounting position (inset).

**Fluorescence Imaging:** The AFM is mounted on an inverted Zeiss Axiovert 200 equipped with a AxioCam HRm digital camera (Carl Zeiss AG, Germany). Rhodamin labeled actin was visualized using a Plan Achromat objective 20x 0.75. n.a.(Zeiss). AxioVision software (Zeiss) was used for image acquisition and ImageJ (<http://rsb.info.nih.gov/ij/>) was used for computation and digital processing.

## 5 Results and Discussion

In the previous chapters the current understanding of the underlying mechanisms of force generation, as well as experimental methods aiming to test these models have been illustrated. From this rather broad perspective, we have the impression that a throughout agreement in the different experiments and modeling attempts is not yet achieved. For example, the Tethered Ratchet [41] model agrees well with observation of *Listeria* or beads in media of different viscous drag [54] [48], while fails to explain the force velocity relationship measured by micromanipulation [55]. On the other hand, the elastic models [5, 25] indeed explain the such force-velocity behavior. However, the reason for force generation and motility in elastic models are strained gels. The strain in these gels is due to curvature, which marks a geometric prerequisite for generation of force and motility in the framework of the mesoscopic elastic models. The flaw in these models became apparent when experiments showed that a gel curvature is *not* essential since actin polymerization also drives flat surfaces forward [69, 111]. For *Listeria* like propulsion of these flat surfaces the gel curvature remains zero.

The puzzling differences in experimental results and theories on actin force generation require detailed experimental examination and complementary testing of the existing theories. With the analysis of actin driven beads we aim to validate the microscopic Tethered Ratchet model on mesoscopic, i.e. observable, parameters. We also present experiments that show the motile behavior of actin propelled beads in confinement and compare the results to self driven colloidal beads with a slight misalignment of their propulsion direction [112].

Another major part of the work is dedicated to direct measurement of force generated by actin polymerization. AFM force measurements on actin networks were pioneered in the lab of D. A. Fletcher [57]. Here we go beyond pure force data acquisition and correlate AFM data with quantitative fluorescence measurements of the gel dimensions and density. Furthermore, the actin in vitro medium allows us to test composition effects of actin gels on their ability to generate force. In the following sections data on the trajectories of motile beads, as well as AFM force measurements in combination with fluorescence microscopy will be presented and discussed.

### 5.1 Trajectories of Actin Propelled Beads

A relatively overlooked aspect of actin-based movement, with very important consequences for *Listeria* or *Shigella* bacteria spreading and efficient cargo delivery, is the directionality of the movement. The question is, how does the bacterium or bead change its direction and what trajectory does it follow? Understanding the shape of the trajectory also gives important insight in the underlying microscopic processes and their regulation. For example Cameron et al. investigate the bead trajectories and find that the curvature of beads in cytoplasmic extracts decreases with the beads size and extract concentration [113]. *Listeria* typically follows very regular, periodic trajectories, that have been explained recently with a phenomenological kinematic model [114]. Actin-propelled beads follow more random trajectories, that have not yet been analyzed in great detail. A theoretical study considers the curvature of the comet tail resulting from random variations in the locations of pushing actin filaments [115]. The local curvature is predicted to have a Gaussian probability distribution, but this distribution has not been measured experimentally. In the following section, we present a statistical analysis of the trajectories of a large number of actin-propelled beads of different diameter. We show that the curvature distribution deviates significantly from a Gaussian distribution, indicating that the microscopic processes that determine the trajectories are not governed by simple random statistics. Furthermore, a stochastic model that relies on the characteristics of the Tethered Ratchet model (see section 3.4.2) is proposed and tested on the experimental data at hand.

From a more general perspective the motion of the actin propelled beads strongly resembles those of self-propelled swimmers in which the propulsion does not perfectly coincide with the bead orientation. Even a slight orientational misalignment of the propulsive machinery will result in circle swimming, which is thus the generic case of self-propulsion. Circle swimming is in fact a very common phenomenon in nature. For example, when confined to two dimensions, circular trajectories are observed for many bacteria and spermatozoa [116]. In the second part of the trajectory analysis we identify propagation modes of actin propelled beads in confining channels. Then the propagation modes are compared to those of a common circle swimmer which can be described analytically [112]. This part is limited to a qualitative comparison of the bead wall interactions. We also perform a quantitative study on how the channel width affects the end-to-end distance of the confined motion.

### **5.1.1 Curvature Distribution of the Bead Trajectories**

We now set out to study actin propelled beads of different sizes moving in quasi 2D without further confinement. After adding N-WASP coated beads to the in vitro medium actin monomers are recruited at the bead surface to form an actin-gel around the bead. After a stage of homogeneous growth, the actin shell breaks open (see paragraph 3.5.1) and the beads start moving in curved trajectories, propelled by a comet tail of actin filaments (Figure 5-2 and Figure 5-3). The aim is to analyze the curvature distribution produced by a large number of bead trajectories. This data will then be compared to simulations based on the Tethered Ratchet model. Hence, one way to look at the experiment is a test of validity for the Tethered Ratchet model. As a first step, we explain stepwise how the curvature data is extracted from the bead trajectories.

**Acquisition of the curvature data:** In Figure 5-2 the different steps in curvature acquisition are exemplified graphically for a representative bead trajectory.

**Step 1:** The underlying experimental data, a time-series of the motile beads, is acquired using phase contrast microscopy with the setup and procedure described in section 4.2.

**Step 2:** Before tracking the beads the images were pre-processed to remove artifacts due to inhomogeneous illumination and to increase the tracking accuracy. In phase contrast microscopy the tracked beads appear very bright with respect to the background, so the signal to noise ratio is unproblematic in this case. However, for automatic tracking we had to account for a) a brightness gradient in each image due to inhomogeneous illumination and unclean optics, and b) changes in brightness over time due to long time image acquisition. Issue a) was solved by normalizing each image with a background reference image, which was taken in a section of the specimen that contains no objects, see Figure 5-1. The “null” normalization was done by subtracting each element of the background image matrix from the time-series image matrices using image processing software (ImageJ, <http://rsbweb.nih.gov/ij/>). Problem b) can be resolved by measuring the mean grey value of each image and subsequent normalization of each image with its corresponding grey value. The result is a time series of images with a constant background. It should be noted that for normalizing images using ImageJ it is advantageous to use 32 bit images, where the elements of the image matrix are represented by real numbers. This ensures “lossless” image processing.



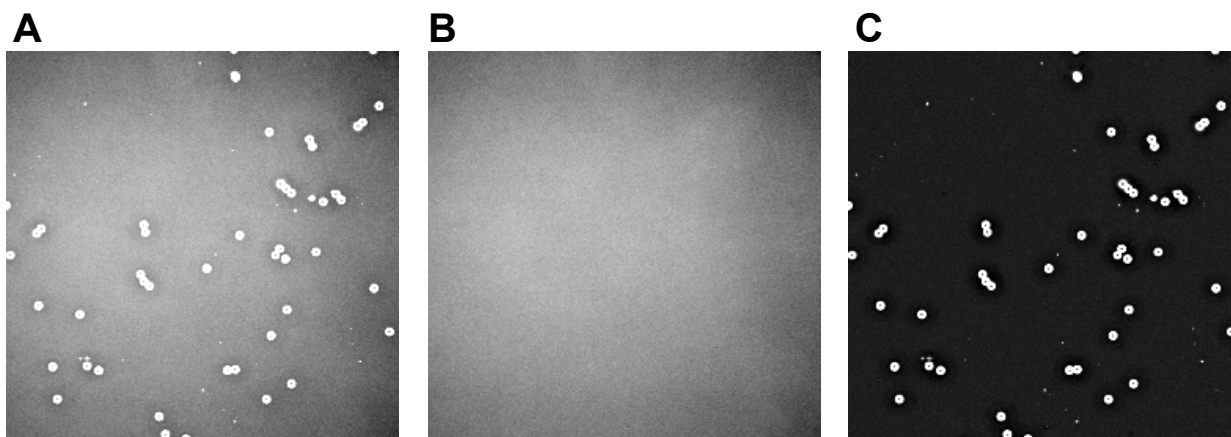


**Figure 5-1** Image background correction: A) Original image, note that the background is illuminated unevenly. In image (A) the beads at the upper right corner have a lower grey value than beads in the center, due to inhomogeneous illumination. However any bead detection algorithm works best if all beads have the same grey value. B) Region of the sample without any beads. This image serves as background reference. C) Background-corrected image after subtraction of the reference image from the original image. The background now appears completely homogeneous and has a grey value of 0. This guarantees reliable automated bead detection.

**Step 3:** The constant background makes it easy to define a threshold in order to differentiate the beads from the background. Usually the lower threshold-grey value, that defines what is considered a bead, is a factor of two larger than the mean grey value of the image. Individual beads are tracked using an algorithm that finds the center of mass of each bead in the successive images<sup>2</sup>. The pixel size of the images is 0.17  $\mu\text{m}$ . In case of the smallest beads (2  $\mu\text{m}$  in diameter) the center of mass calculation was averaged over circa already 100 pixels. Following [117] we obtain a spatial accuracy of a few tens of nanometers by tracking the beads.

**Step 4:** To characterize the bead trajectories, we analyze the local curvature of the trajectories, which can be calculated as  $\kappa = (\dot{x}\ddot{y} - \dot{y}\ddot{x})/(\dot{x}^2 + \dot{y}^2)^{-3/2}$  where  $x$  and  $y$  are spatial coordinates and each dot denotes differentiation with respect to time  $t$  [118]. In order to avoid possible artifacts due to er-

<sup>2</sup> ImageJ particle tracking plugins that detect the mass center of the particles can be found under <http://valelab.ucsf.edu/~nico/IJplugins/MTrack2.html> or <http://weeman.inf.ethz.ch/particletracker/>

## 5. Results and Discussion

rors in the position determination and amplification thereof by the numerical differentiation of the  $xy$  data, the trajectories are first numerically smoothed using a least squares polynomial smoothing procedure, in which a quadratic function was fitted locally to the data in a moving window corresponding to a path length of  $10\ \mu\text{m}$ . In this way, only radii of curvature larger than roughly  $1\ \mu\text{m}$  are considered, much larger than the error in the position determination (a few tens of nanometers, see above).

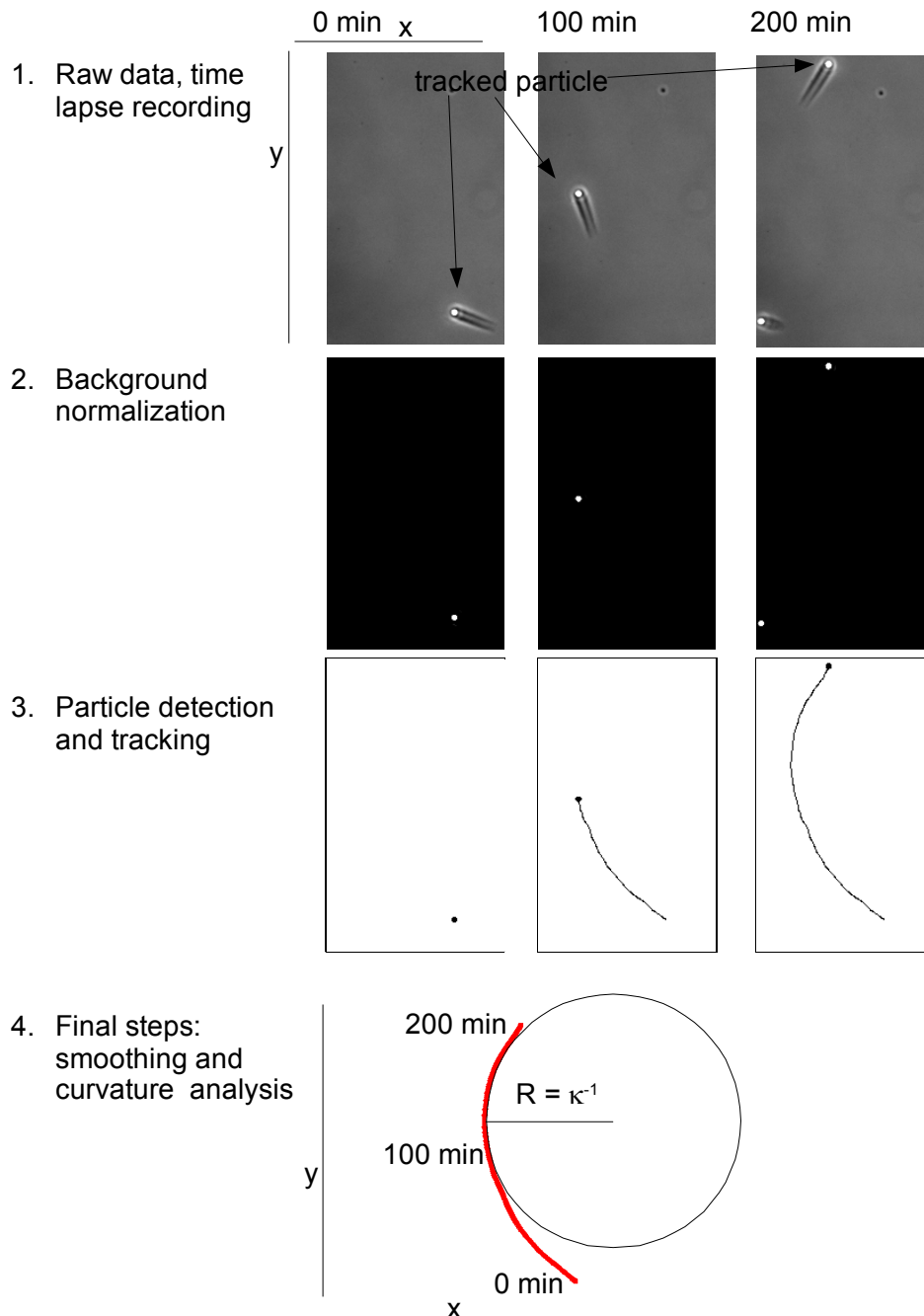


**Figure 5-2** Summary of the bead trajectory analysis procedure.

**Experimental findings:** The trajectories of individual beads may vary strongly in shape and curvature. The typical radius of the observed circular motion is on the order of 50 to  $<1000 \mu\text{m}$ . Thus, on the length scale of the imaged area, the motion of the beads appears to be non random. Rather, the beads resemble a circular swimmer behavior, seemingly perturbed by Brownian noise, which is superimposed on the self-generated motion. The speed of the beads is on the order of  $2.5 \mu\text{m}/\text{min}$  for beads with a radius of 1 and  $1.5 \mu\text{m}$ , while beads of  $3 \mu\text{m}$  radius move more slowly at approximately  $1.2 \mu\text{m}/\text{min}$ . After several hours the speed of the beads starts to decrease gradually, and after 8 hours it is about 20 percent of the initial speed.

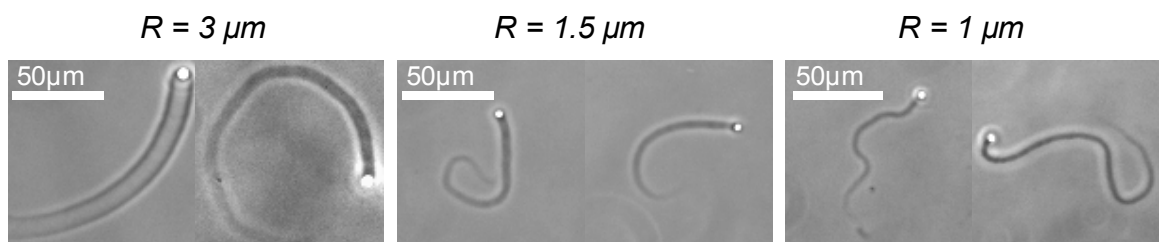


**Figure 5-3** Randomly chosen phase contrast images of  $3 \mu\text{m}$ ,  $1.5 \mu\text{m}$ ,  $1 \mu\text{m}$ , radius beads. About 80% of the tails are hollow for  $R = 3 \mu\text{m}$ , while for  $R = 1$  and  $1.5 \mu\text{m}$ , all tails appear homogeneous. Note, that the actual trajectories are much longer, because the tail depolymerizes from the back.

The bead velocity is governed by the polymerization speed of the actin filaments. The bead principal motion is predetermined by the speed and direction of the actin filament polymerization, while the Brownian motion is superimposed to the principal motion. The Brownian motion may therefore lead to a change in direction by which a curvature is introduced into the path of motion. In first approximation the curvature is correlated with the bead velocity: The larger the bead velocity, the smaller are Brownian effects and hence the curvature is reduced. In a first experiment we test this hypothesis. Figure 5-4 shows a plot of the measured (smoothed) curvature at each time frame as a function of the corresponding velocity for all three bead sizes. Clearly, there is no correlation between the curvature and the velocity, which suggests that the trajectory curvature is not merely a kinematic phenomenon. Rather, pushing and pulling filaments could be randomly distributed along the bead surface and thereby introduce the trajectory curvature. However, considering the persistent circular motion of some beads, it seems that the molecular processes underlying in actin based motility are not random. We are going to test whether these processes are

purely stochastic by analyzing the curvature distribution of a large number of bead trajectories.

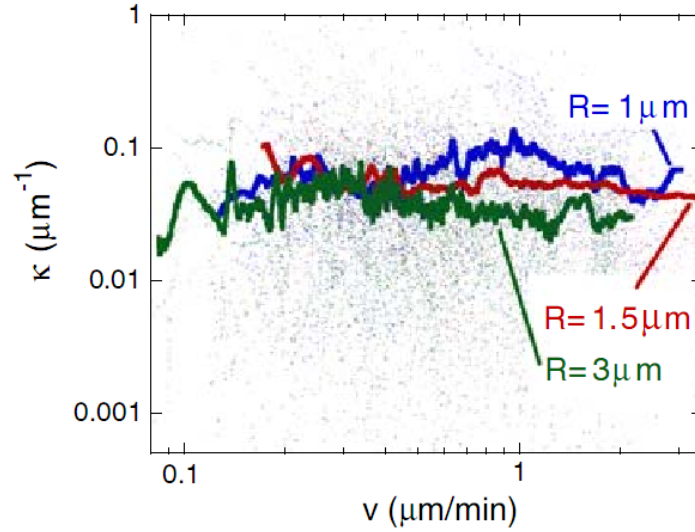


**Figure 5-4** Local curvature ( $\kappa$ ) as a function of bead velocity ( $v$ ) for different radii. The lines are moving averages (period of 250 points) that clearly show that there is no correlation between  $\kappa$  and  $v$ .

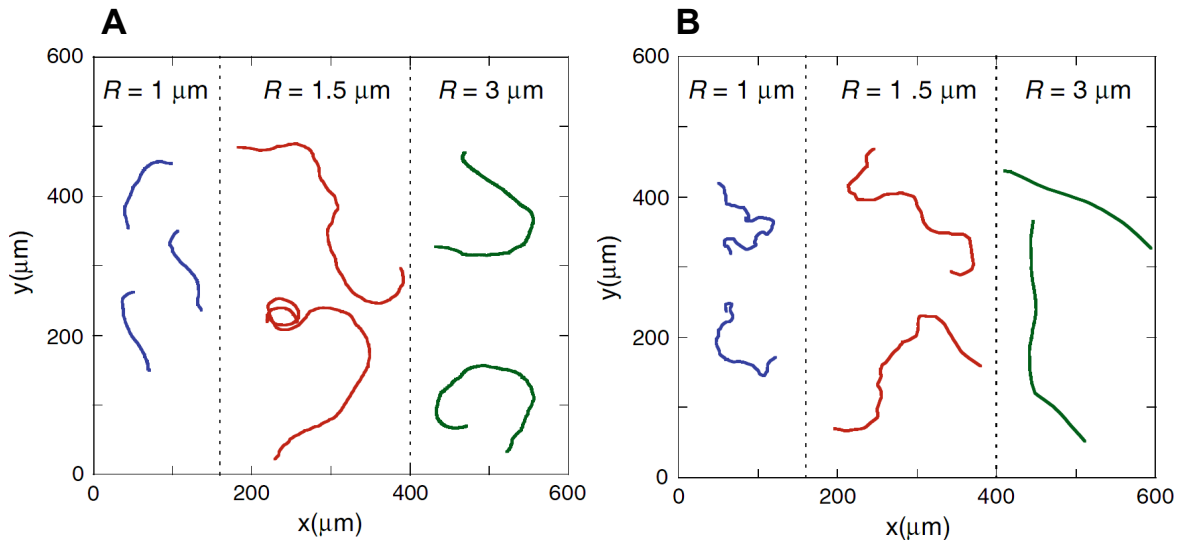


**Figure 5-5** Experimental (A) and simulated trajectories (B) for three bead sizes. Time taken for trajectories is 120 min for 1  $\mu\text{m}$  beads and 300 min for 1.5 and 3  $\mu\text{m}$  beads.

As shown in Figure 5-6 (blue squares), the root mean-square curvature decreases slightly with increasing bead size, from  $0.13 \mu\text{m}^{-1}$  for  $R = 1 \mu\text{m}$  to  $0.08 \mu\text{m}^{-1}$  for  $R = 3 \mu\text{m}$ . Then the probability distribution  $P(\kappa)$  is constructed, where  $P(\kappa)d\kappa$  gives the relative frequency of curvatures between  $\kappa$  and  $\kappa + d\kappa$ ,

and the cumulative distribution function  $CDF(\kappa)$ , obtained by ranking the absolute values of the experimental  $\kappa$  from low to high and plotting their ranking number (divided by the total number of data points) as a function of  $\kappa$ . We note that changing the window size or order of the smoothing filter or using a cubic splines algorithm did not change the shape of the curvature distribution, although the absolute values of  $\kappa$  shift towards smaller curvatures if a larger smoothing window is used (doubling the window size decreases  $\langle\kappa\rangle$  by about 10–20%). Also, restricting the analysis to the first hours of the trajectories, where the speed is more or less constant, did not affect the shape of the curvature distribution.

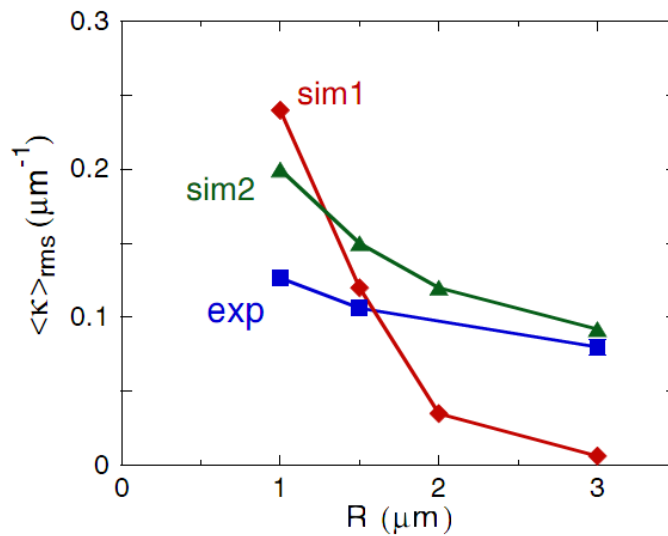


**Figure 5-6** Root-mean-square curvature as a function of bead radius: experimental (exp), simulations (sim1, homogeneous actin comets), and simulations with a nucleation probability that decreases exponentially with increasing distance from the tail edge (sim2, hollow actin comets) (see text).

Figure 5-7A and B show the measured  $P(\kappa)$  and  $CDF(\kappa)$ . After normalizing the curvature by the root-mean-square curvature, the data for different radii all collapse onto one curve (apart from small deviations for the smallest beads at small curvatures). The dashed black lines in Figure 5-7A and B resemble a Gaussian distribution, as predicted by [115]. For small curvatures, the Gaussian distribution fits the experimental data reasonably well, but for larger curvatures there are strong, systematic deviations for all three bead sizes: large curvatures occur much more frequently than would be expected for a Gaussian distribution. (An empirical fit that gives an accurate description of the experimental distribution is a modified log-normal distribution,  $P(\kappa) = cst \cdot \exp[-(\ln(a|\kappa|)/\langle\kappa\rangle +$

1))<sup>2</sup>] with  $a = 2.32$ ). The specific aim of this investigation is to develop a model that reproduces the experimentally found non-Gaussian curvature distribution.

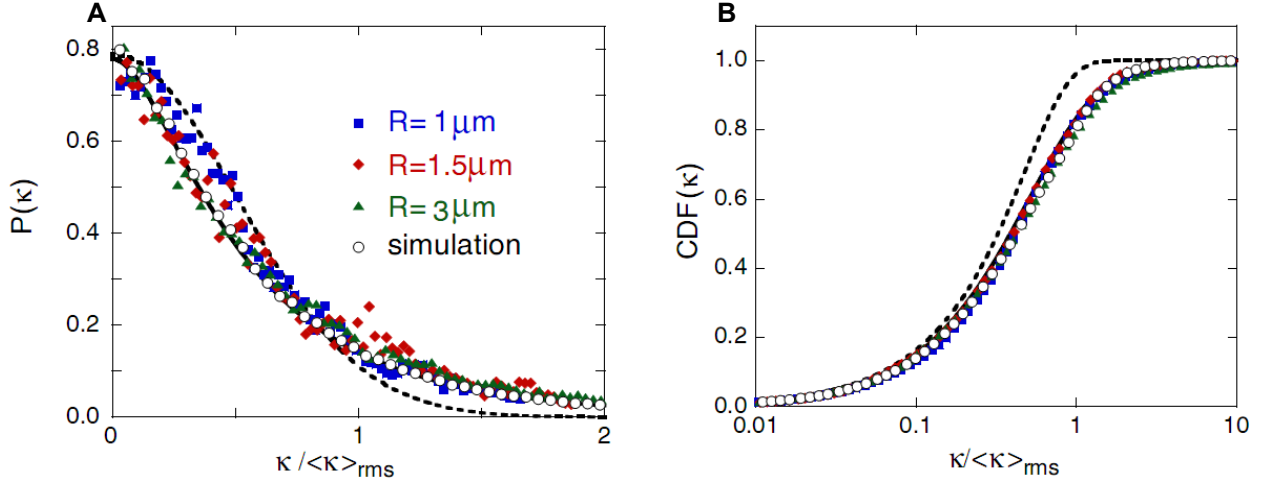


**Figure 5-7** Results of trajectory curvature analysis A) Curvature probability distribution and B) cumulative curvature distribution function for different radii. The curvatures have been normalized with respect to the root-mean-square curvature. The dashed black lines correspond to a Gaussian distribution and the solid black lines to an empirical, modified log-normal distribution  $\mathbf{P}(\kappa) = cst \cdot \exp[-(\ln(a|\kappa|/\langle \kappa \rangle + 1))^2]$

First of all, according to the central limit theorem [119], a combined effect of many additive random processes always results in a Gaussian distribution. Therefore, the non-Gaussian distribution of curvatures cannot be explained by models that derive curved trajectories from independent random variations in microscopic parameters (such as the local filament density, as in Rutenberg and Grant [115]). To explain the relatively high probability of finding large curvatures, a coupling mechanism between the curvature of the trajectory and the microscopic processes is required. In the following a stochastic model is proposed, based on the known details of polymerizing actin networks, that incorporates such a coupling. The stochastic simulation includes nucleation, dissociation, polymerization, and capping of actin filaments.

**The model:** To test for curved trajectories (in two dimensions), we let the filament density vary in one direction along the bead surface. Nucleation (by the Arp2/3 complex, which is activated by surface-bound N-WASP) is restricted to one-half of the bead surface and occurs with equal probability (rate constant  $k_n$ )

all over the hemispherical surface (in the following, we will consider a case where nucleation is inhomogeneous). Experimental evidence shows that the actin comet tail is firmly attached to the bead surface, indicating that at least a part of the actin filaments is linked to the surface [55, 56, 64]). To account for this attachment, we follow the “Tethered Ratchet” Model by Mogilner and Oster (see section 3.4.2, where it was argued that an actin filament is attached to the surface when it is nucleated, associated to the proteins on the bead surface in a complex with Arp2/3, N-WASP and actin. Figure 3-4 (p. 24) illustrates the working principle of the Tethered Ratchet and the assumptions made here. After some time, the filament dissociates from this complex (with the rate constant  $k_d$ ) and is able to grow and push against the bead surface, until it is capped by the capping protein gelsolin (with rate constant  $k_c$ ) and loses contact with the surface. At every instant, there is a population of attached filaments that have just been nucleated and a population of free filaments that grow. The attached filaments are in tension, because the link between the bead and the filament is stretched as the bead moves forward, resulting in a force  $f_a^i = k_a x^i$  resisting bead movement. Here,  $k_a$  is the spring constant of the attachment link and  $x^i$  is the extension of link  $i$  (equal to the trajectory length of that particular link from the moment that the link is generated). At the same time, the dissociated, growing filaments are in compression and generate the propulsion force. We assume that the filaments can be modeled as elastic rods with a bending rigidity  $k_f$ . The bending rigidity depends on the length of the filament, but for simplicity we assume here that  $k_f$  is equal for all filaments. The elastic force exerted by a compressed filament is  $f_w^i = k_f \Delta^i$  where  $\Delta^i$  is the distance between the equilibrium (free) position of the tip of filament  $i$  and the bead surface ( $\Delta^i < 0$  and  $f_w^i < 0$  for compressed filaments). If  $\Delta^i > 0$ , the filament does not touch the surface and  $f_w^i = 0$ . As a result of the pushing and pulling forces exerted by all attached and growing filaments, the bead moves towards an equilibrium position in which the sum of forces equals zero, as well as the sum of moments (we assume that all forces are in the forward direction):  $\sum_i f_a^i + \sum_j f_w^j = 0$  and  $\sum_i f_a^i r_i + \sum_j f_w^j r_j = 0$ , where  $r_i$  is the location of the filament in the direction perpendicular to the direction of movement. The dissociation rate  $k_d$  of filaments from the bead surface depends on the force acting on the link: pulling on a bond lowers the activation barrier and enhances dissociation. This has been observed experimentally by Marcy et al. [55] who showed that the comet tail could be de-

tached from the bead by pulling on it. The Tethered Ratchet model suggest that relation between the dissociation rate and the force can be approximated by an exponential equation [65]  $k_d = k_{d,0} \exp(f/f_b)$  where  $k_{d,0}$  is the dissociation rate for an unloaded link and  $f_b$  is the strength of the attachment link. The polymerization rate constant  $k_+$  of actin filaments may also depend on the force acting on the filament [41], but for simplicity we assume here that the polymerization rate is constant.

The key feature of the model is a positive feedback loop: The ratio of pushing/pulling filaments is allowed to vary on the bead surface. At sites with larger pushing forces the filament dissociation is increased, generating more pushing filaments. This results in an even larger pushing force that promotes itself in a site-specific manner, e.g. left side or right side of the bead. Hence a persistent torque would act on the bead rendering the curvature distribution non Gaussian.

**Simulation:** We analyze the model by performing stochastic simulations, using the algorithm of [120]. In every simulation step, a new filament can nucleate somewhere on the bead surface, or existing filaments can detach, polymerize, or be capped, with relative probabilities given by the respective rate constants. After each microscopic reaction, the bead position and orientation are updated (by translation and rotation) to restore mechanical equilibrium, and the forces acting on the attached and free filaments are recalculated. The values for the different parameters used in the simulations are listed in the appendix, see Table 8-1 (p. 141). Values for  $k_+$  [10] and  $[A_g]$  [121] were obtained from literature data, and  $\delta$ ,  $k_{d,0}$ ,  $k_c$ ,  $k_a$ , and  $f_a$ , were estimated in [41]. For the bending rigidity  $k_f$  of an actin filament, we use 0.3 pN/nm, which corresponds to a filament length of a few hundred nanometers [63], and for the nucleation rate  $k_n$  we use  $0.8 \text{ s}^{-1} \mu\text{m}^{-2}$ . With these parameters, the filament density is around 100 per  $\mu\text{m}^2$ , about 5–10 percent of which is attached. The resulting average bead velocity is  $1.5 \mu\text{m min}^{-1}$ , similar to the experimental velocities.

**Simulation results, homogeneous actin comets:** Here we assume a homogeneous actin comet with a constant density of actin filaments along its cross-section. Figure 5-6 (p. 69) displays simulated bead trajectories for all three different bead sizes. The curvature of the simulated trajectories is analyzed in the same way as the experimental trajectories. The resulting curvature distribution is shown in Figure 5-7A and B (p. 70), together with the experimental data. Although the absolute values of the curvatures differ between experiments and si-



mulations, the shape of the simulated curvature distribution is in excellent agreement with the experimental curve. The non-Gaussian shape of the distribution is reproduced in the simulations as a result of the coupling between the force acting on the attachment bonds and the detachment rate, see Eq. 3-5. Indeed, if this coupling is turned off (by taking  $f_b$  infinitely large in Eq. 3-5), the simulated curvature distributions become Gaussian, as would be expected for independent, additive random processes. The physical reason for the non-Gaussian curvature distribution and the relatively high frequency of large curvatures is a positive feedback mechanism. When the bead bends off to the right, attachment bonds on the left (in the outer lane) are more strongly stretched than those on the right (in the inner lane). According to Eq. 3-5, this leads to faster detachment on the left and thus to more detached, pushing filaments on the left and an increase of the torque inducing curvature to the right. This positive feedback explains the relatively high propensity for high curvatures observed in the experiments and simulations.

***Simulation results, hollow comets:*** Figure 5-6 (p. 69) displays the root-mean-square curvature as a function of bead size (red diamonds). As seen in the experiments, the mean curvature decreases with increasing bead radius, probably because larger beads have more filaments, so that fluctuations are relatively less important. However, the effect of the radius is much stronger in the simulations than in the experiments: between  $R = 1 \mu\text{m}$  and  $R = 3 \mu\text{m}$   $\langle \kappa \rangle$  decreases by a factor of 40 in the simulations and only by a factor of 1.5 in the experiments. A possible explanation for this difference may be that the reaction rates on the bead surface are inhomogeneous, due to slow diffusion of proteins through the comet tail. Such diffusion limitation is indeed suggested by our observation that the speed of the beads decreases by about a factor of two when  $R$  increases from 1.5 to 3  $\mu\text{m}$ , see [121]. Due to hindered diffusion through the dense actin network, a concentration gradient of proteins arises in the comet tail, with the lowest concentration in the middle of the tail. This effect is much stronger for large beads than for small ones, because of the larger diffusion distance. The ARP2/3 concentration gradient leads to a nucleation probability that is lower in the middle of the bead than at the edges, which leads, in turn, to a lower filament density in the middle. Indeed, about 80% of the comet tails for the 3  $\mu\text{m}$  beads appeared hollow (see Figure 5-3, p. 67). To test the effect of inhomogeneous nucleation on the shape of the trajectories, we did simulations with an inhomogeneous nucleation probability, keeping all other reaction rates homogeneous. The

concentration of the ARP2/3 complex decreases exponentially from the edges to the middle of the hollow comet  $[ARP] \propto \exp((r - R)/(D/k'_n))$ . Here  $r$  is the position perpendicular to the direction of movement,  $R$  the radius of the bead,  $D/k'_n$  is the characteristic diffusive layer length<sup>3</sup>. In Figure 5-6 (p. 69) the result for  $D/k'_n = 0.5 \mu\text{m}$  results are shown (green triangles). Clearly, inhomogeneous nucleation leads to a radius-dependence that is closer to the experimental trend, although still not completely the same. In practice, of course, also the polymerization and capping rates will be affected by protein diffusion, each with their own diffusive layer. So in principle, the simulation could be adjusted further to account for the diffusion of all reactants. However, diffusion of the involved reactants to the bead surface has not yet been determined by experiments. Therefore we stop the discussion at this point and note that diffusion might lead to increased curvatures of actin propelled beads.

**Autocorrelation function:** Another consequence of the feedback mechanism is that the beads typically maintain a certain curvature for times much longer than expected from the microscopic rate constants. The persistence time can be assessed by analyzing the curvature autocorrelation function,  $ACF(\tau) = \langle \kappa(t)\kappa(t + \tau) \rangle / \langle \kappa^2 \rangle$ . The experimental autocorrelation function was calculated from the complete set of curvature data available. A large number of simulated trajectories were generated to calculate simulated autocorrelation function. The experimental and simulated autocorrelation functions are shown as a function of the delay time  $\tau$  in Figure 5-8. In both cases, the ACF decays to zero in approximately 10 minutes, implying that the bead maintains its curvature for about 10 minutes, indeed much longer than the average life time of a filament  $k_c^{-1} \approx 10$ . Here the initial decays of the experimental and simulated correlation functions are in excellent agreement. The experimental autocorrelation function shows additional features: It becomes negative after the initial decay and is non-zero at even after one hour. The negative values indicate that the sense of curvature for some trajectories is changing regularly, which means that these beads do not run persistently in a circle but rather in a sinuous fashion. On the other hand, some beads seem to run in a circle of constant curvature, as indicated for the non-zero values at large  $\tau$ . Both, sinuous and circular motion is often found for *Listeria* bacteria moving in cell extracts [114]. We assume that per-

---

<sup>3</sup>At steady state the diffusive flux of ARP2/3 can be described as  $J_D = D\delta[ARP]/\delta r$ , which is equal to the ARP2/3 consumption per unit area  $J_S = k'_n[ARP]$

sistent circular bead motion could be due to an irregular surface distribution of pushing actin filament, caused by inhomogeneous NPF surface coating. Such inhomogeneities result in a constant torque on the bead and induce circular motion. Sinuous motion could be caused by additional rotation of the bead. Similar longitudinal rotations of the elongated *Listeria* bacteria also explain why the pathogen often moves in regular sinusoidal patterns [122].

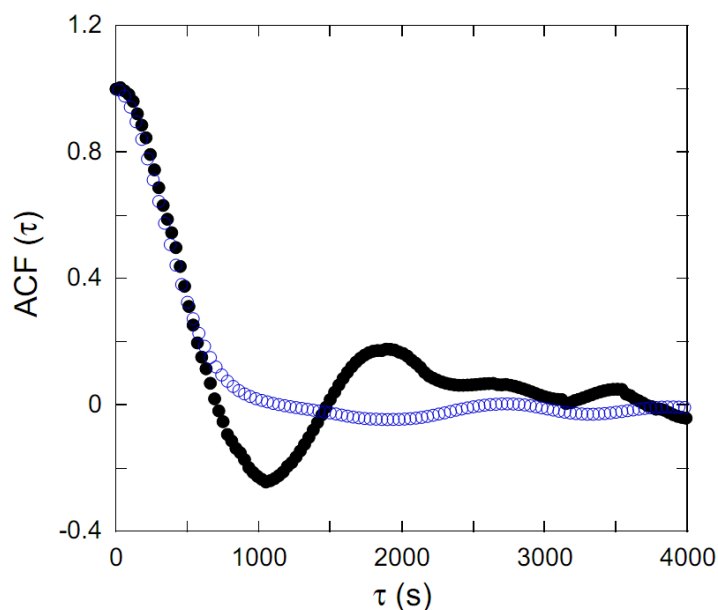


**Figure 5-8** Experimental (filled circles) and simulated (open circles) curvature auto-correlation function.

**Summary:** The main finding is that the actin-based movement of biomimetic colloids is characterized by a non-Gaussian curvature distribution. The stochastic kinetic model nicely reproduces the non-Gaussian shape of the experimental curvature distribution. The model provides strong support for a force-dependence of the microscopic reactions involved in actin-based motility and thus validates the “Tethered Ratchet” Model. However, only the detachment rate was assumed to depend on the force, but in practice also the polymerization rate could be force-dependent, leading to an additional positive feedback mechanism. Also, diffusion limitations alter the spatial distribution of force producing polymerization reactions on the bead surface. Such additional effects were not entirely considered in the stochastic simulations. Quantitative measurements on the polymerization force dependence and diffusion effects are required. Measurements with a varying medium composition or different bead geometries could reveal such effects. Also deliberate asymmetric bead coatings

could be used to mimic and reveal the more persistent nature of *Listeria* trajectories.

### **5.1.2 Trajectory Analysis in Confining Channels**

In vivo the motion of actin propelled pathogens like *Listeria* is confined due to obstacles in cells such as organelles and the cell membrane. In the previous chapter we have found that actin propelled motion favors large curvatures which could be advantageous for pathogens in that they avoid running into obstacles. It is worthwhile to test such assumptions in an assay where actin propelled beads move in confining geometries. Here we analyze the motion of actin propelled beads in confining channels of varying width and test how the traveled distance is affected.

## 5.1 Trajectories of Actin Propelled Beads

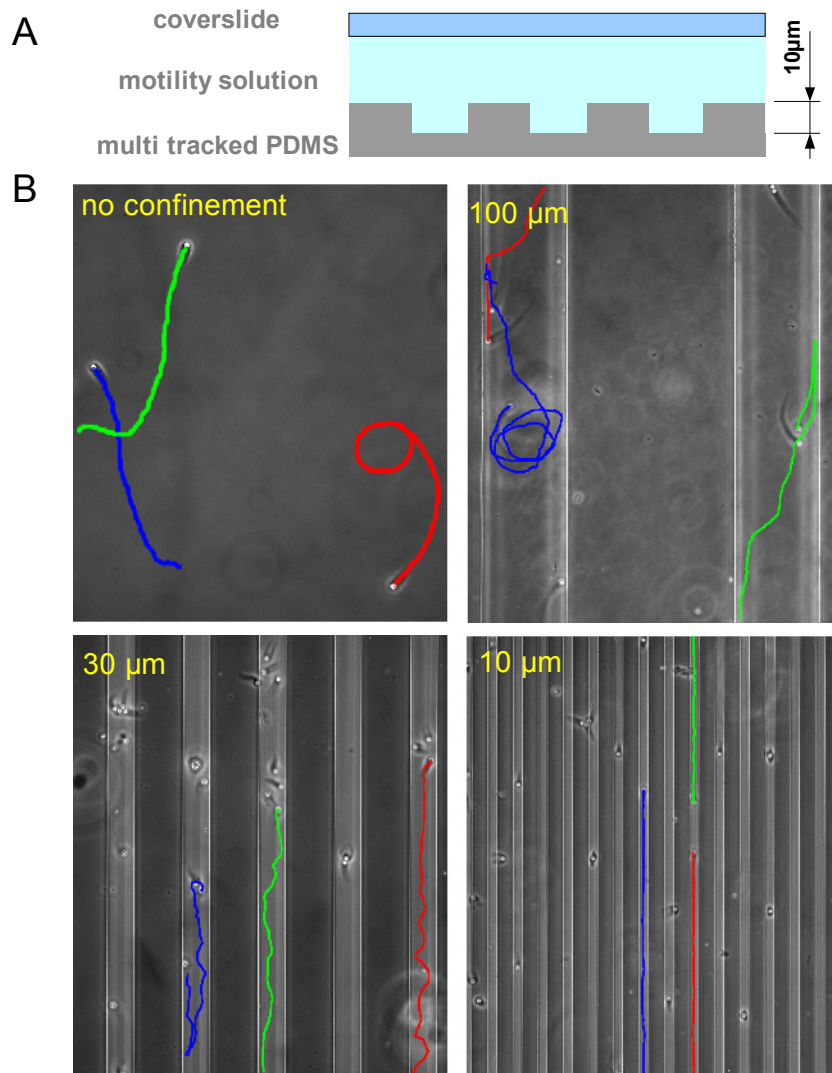


**Figure 5-9** A) Cross section of the confining channels embossed into PDMS via soft lithography. B) Actin propelled beads with  $R=3 \mu\text{m}$  in multiple channels, trajectories are visualized in color. Trajectories in  $100 \mu\text{m}$  channels show all possible modes of bead wall interactions. green: turning with the torque, blue: turning against the torque, red: persistent sliding along the wall.

If we confine the beads between micro-structured substrates and cover slides, a fraction of the beads is moving in the channel structures that are embossed in the substrates (Figure 5-9A). The beads are trapped in the channels and remain there until they interact with the channel wall, i.e. by running against the channel, or by running into each other (see Figure 5-9, the  $10 \mu\text{m}$  channels, the red and green trajectory). Therefore, the bead motion can be confined and oriented along the channel (Figure 5-9B). It is interesting to note, that the beads remain in the channel if their motion is unobstructed. This implies that they move preferentially along the substrate. In the previous section we showed that the num-

ber of left and right turns are fairly equal, so there is no preference of direction in the  $x,y$  plane. The apparent preference in the  $z$ -direction could be due to the following reasons: a) gravity or b) a smaller polymerization speed of the network side facing the substrate. The gravitational force is in the sub-pN regime, which is much lower than the driving force of actin polymerization (nN-regime). But since there is no inherent preference of the actin machinery to move in a certain direction, such small gravitational forces are sufficient to bias the direction persistently. The polymerization effect considered in b) works as follows: Once a bead is near the substrate, the diffusion of g-actin or ARP2/3 to the bead surface that faces the substrate is reduced, while there is no reduced diffusion to the bead top-side. Hence, the polymerization at the bottom-side is weaker as compared to the top-side. This generates a persistent torque that pushes the bead to the substrate, and hinders upward motion.

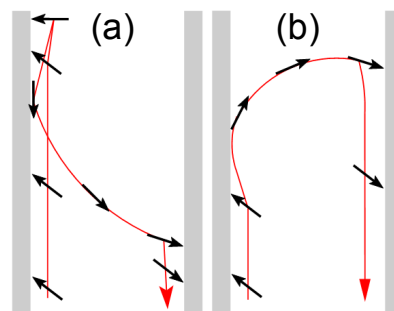


**Figure 5-10** The paths governing the bead-wall interaction (a) turning with the torque, (b) turning against the torque.

We now analyze interaction modes of the self-propelled beads with the channel wall qualitatively. When a bead hits the channel wall it may a) move out of the channel b) undergo persistent sliding along the wall or c) turn away from the wall. For example, the cases b) and c) respectively occur for the red and blue trajectory shown in Figure 5-9B in the  $100\ \mu\text{m}$  channel. We suspect, that the curvature of the bead trajectory, its speed, and the angle between trajectory and wall control how the bead acts as it runs against the channel wall. Small angles, low speeds and large curvatures increase the probability of sliding along the wall. Turning away from the wall, c), occurs in two different modes: 1) turning in the direction of the torque, or 2) turning against the direction of the torque. Figure 5-10 shows these two modes schematically. Both modes occur often in the experiment, e.g.: In the micrograph taken for the  $100\ \mu\text{m}$  channels.

Here the blue trajectory indicates turning in the direction of the torque, while the green trajectory indicates turning against the direction of the torque. Van Teeffelen et al. [112] predict such behavior in models that reproduce the motion of circle swimmers in confined geometries. They found, that the probability of mode 1) increases at higher curvatures, while the probability of 2) decreases in this case. This is in agreement with our experimental observations. A more quantitative analysis of trajectory speeds, angles and curvatures could be used to test the existing circle swimmer models. Such a modeling approach could be used to quantify the torque acting on the actin propelled beads and to predict the motion of the bead in different channel geometries.

Upon varying the channel width from 10  $\mu\text{m}$  to 100  $\mu\text{m}$  we observe an influence on the straightness of the bead trajectories. For the smallest channel width (10  $\mu\text{m}$ ) and using beads 6  $\mu\text{m}$  in diameter any curvature in the trajectories is eliminated. The beads move at a mean velocity of 2.5  $\mu\text{m}/\text{min}$ . Interestingly the bead velocity remains unchanged even for the smallest channel width. Here the bead and the comet should be in permanent contact with the channel wall which adds to friction resisting the forward motion (usually the comet is curved and even thicker than the bead [64]). Obviously the driving force of the actin machinery is much larger than the additional drag added by the channel walls.

We analyze the end-to-end distance,  $d_{e2e}$ , of the bead trajectories for a varying width of the confining channels. Figure 5-11 shows individual end-to-end distances, while Figure 5-12 depicts the averaged curves for each channel width. Comparison with a computed random walk (grey curve Figure 5-12) with the same contour velocity shows that actin based motion is clearly non random in the scale of observation (500  $\mu\text{m}$ ). The slope  $\log d_{e2e} / \log t$  for a pure random walk is 0.5, while for the beads in the end to end distance range  $d_{e2e} < 200 \mu\text{m}$ ,  $\log d_{e2e} / \log t \approx 1$ . This means that the bead motion is clearly non-random, which is a consequence of self propulsion. At increased channel width the slopes of the  $d_{e2e}$  curves decrease earlier, while smaller channels further reduce the degree of randomness, i.e. we obtain larger  $d_{e2e}$  values in particular at longer tracking times.

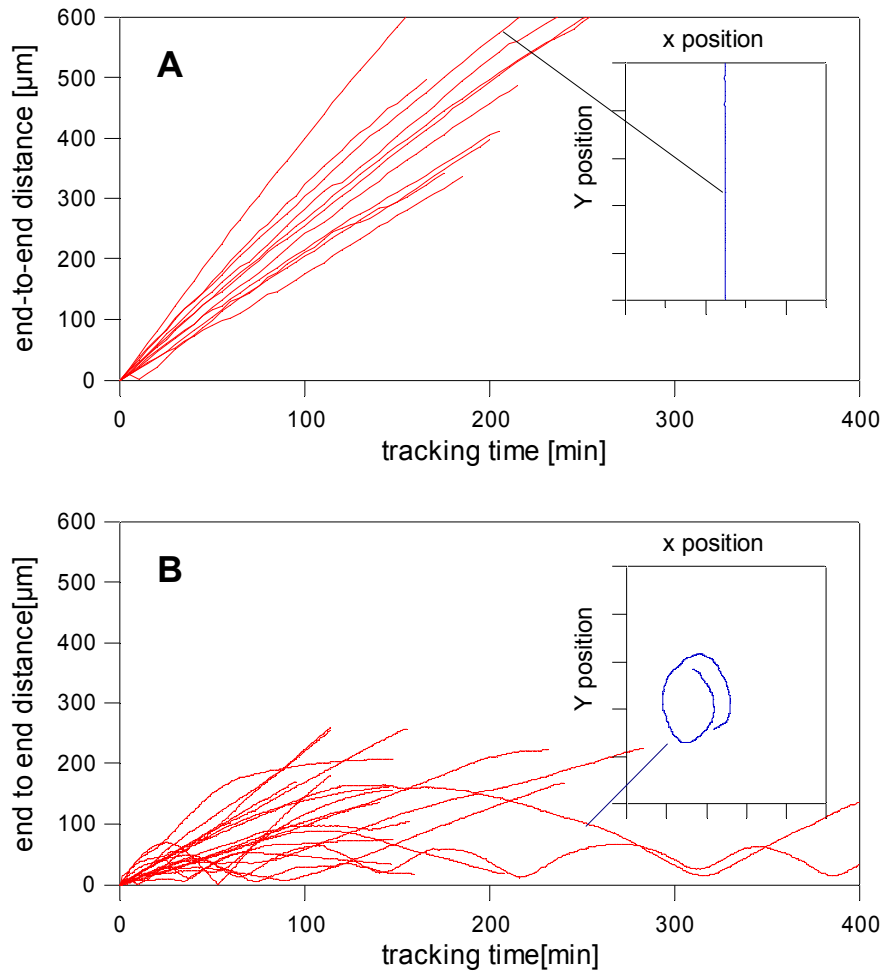


**Figure 5-11** A) End-to-end distances of individual bead trajectories in channels of 10  $\mu\text{m}$  width. B) End-to-end distances in channels of 100  $\mu\text{m}$  width.



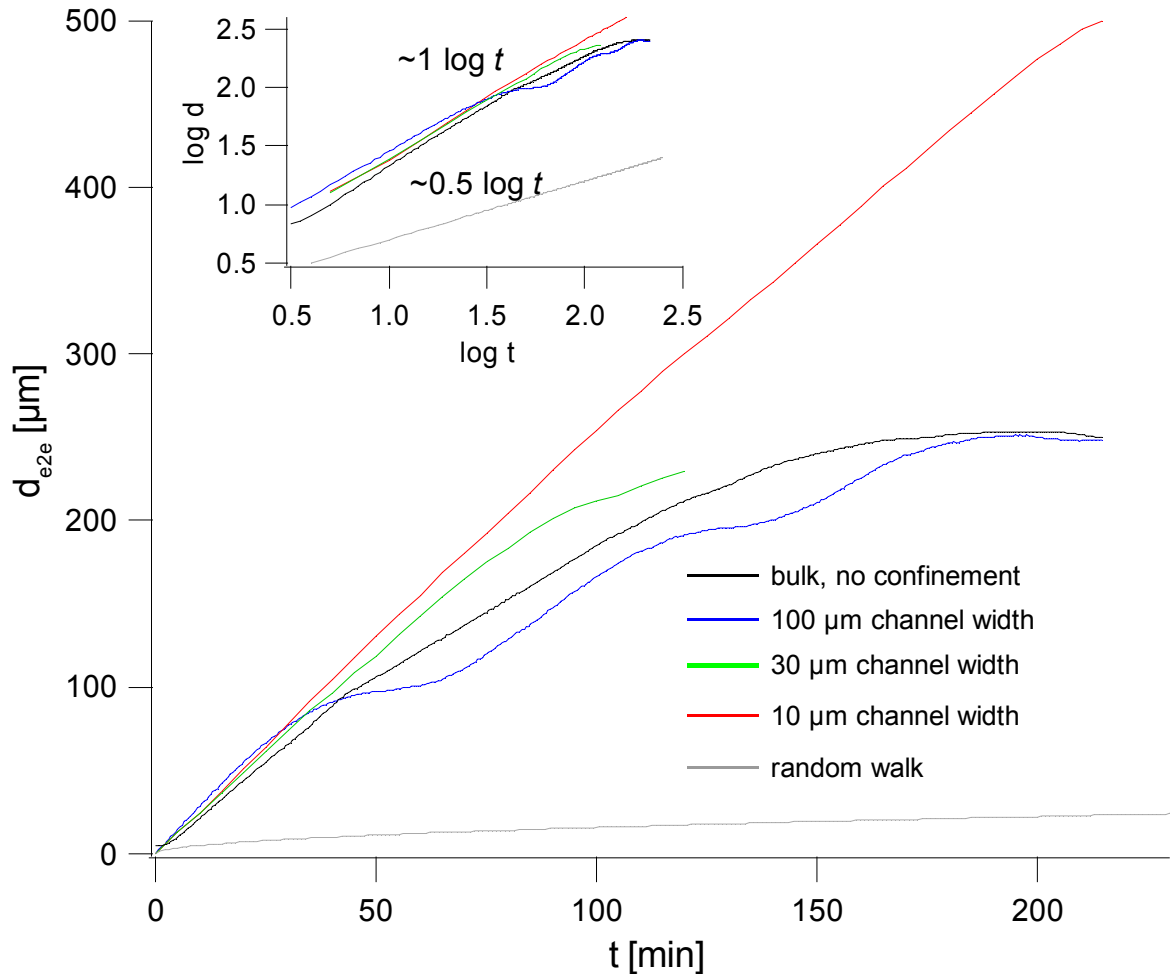


**Figure 5-12** Average end-to-end distances  $d_{e2e}$  of the beads in confining channels of varying width. Comparison with a pure random walk (grey). For and increasing channel width the slope of the  $d_{e2e}$  curves decreases. The exponent in the log-log plot for the random walk is 0.5 and 1 for the beads. This shows that the beads are indeed self-propelled and not driven by mere diffusion.

**Perspectives:** In future studies one could further analyze the bead-wall interaction and also vary the channel geometry with the aim of fractioning the beads according to their trajectory curvature. In this preliminary experiment we already saw that the beads in the 100 μm channels show some self-fractioning according to their curvature, see end-to-end distances in Figure 5-11B. If the trajectory curvature is on the order or smaller than the half of the reciprocal channel width, the beads move fast along the axis of the channel, at larger curvatures they move considerably slower. For an improved particle fractioning we suggest to use more efficient geometries than plain linear channels. A corresponding

study has been published by Hulme et al. [123], where *Escherichia coli* is sorted by its length in spade-like structures.

## **5.2 AFM Force Measurements**

As shown in paragraph 3.3, there already exists a few of approaches to measure the forces due to polymerization of actin in vitro. In contrast to the already described direct force measurement approaches [55, 57], the actin polymerization in the experiments explained here is limited passively, i.e. by the actin gel itself, and not by the probing force directed against the direction of polymerization. The passive polymerization limitation is mainly due to mechanical stresses in the gel which are a result of surface bound monomer insertion on a curved substrate and filament crosslinking, see section 3.5. This effect is well known and has been analyzed by TEM-imaging and modelling [6, 70]. The magnitude of the limiting stress that keeps the actin gel from extending has not yet been directly measured. Here, our colloidal probe AFM technique now allows estimating the internal stresses in the gel. As shown in the following chapter, we find that the limiting forces generated by our setup are an order of magnitude smaller than the maximum forces generated by natural actin gels. This can be discussed as resulting from the convex-curved gel geometry here, while actin gels in nature, e.g. the elongated comet propelling *Listeria*, attain different geometries with the filaments polarized against the external force. This shows that geometric constraints are crucial for the force generating capabilities of the actin gel.

Besides investigating the influence of the substrate geometry, we also prepare different actin gel compositions and test their ability to generate forces against a load. In cells the gel composition and its microstructure is varied via actin binding proteins. Their effect on the force generation potential has not yet been directly studied. Here we vary for example the degree of branching via modulation of ARP2/3 in the network and find that the stiffness and limiting force increases with the degree of branching. Actin networks formed via the formin mechanism show an even lower ability to generate forces. These networks of only unbranched, linear filaments show a magnitude lower maximum force compared to branched networks. Capping of filaments barbed ends via gelsolin has an opposite effect. When increasing the gelsolin content the stiffness and maximum forces are decreased. We furthermore test the effect of a very potent drug, phalloidin, which alters the flexibility and polymerization properties of actin filaments. Small concentrations of phalloidin slow the network growth but increase its stiffness. To be able to perform the AFM based

measurements, a suitable setup has to be developed in the first place, which is subject to the discussion in the following paragraph.

### **5.2.1 Development of the AFM-Experiment**

Measurement of force on active gels is not a standard AFM procedure. Therefore, a new measurement technique has to be developed, allowing for quantitative collection of force data on the mechanically weak actin gels. This section describes several experiments that were conducted in order to find a suitable measurement technique. The following AFM related issues and their solution will be described in detail in the forthcoming subchapters:

**5.2.1.1 Cantilever passivation**, p. 84. A cantilever preparation procedure has to be developed ensuring that all growing actin gel is confined between the apex of the cantilever and the substrate (as sketched Figure 4-1, p. 59)<sup>4</sup>. In the course of development we direct the actin gel growth by controlling the surface chemistry of the force probe (surface passivation).

**5.2.1.2 Thermal drift of the setup**, p. 86. The thermal drift of the AFM setup must be determined to estimate the error of the method.

**5.2.1.3 Quantitative Fluorescence Measurements**, p. 88. Development of a Quantitative Fluorescence Measurement Method in Combination with the AFM Experiment.

**8.2 Force measurement on actin comets at the colloidal probe**, p. 142. The bending/sliding behavior of the confined actin gel *after* symmetry break was tested upon compression with the AFM cantilever.

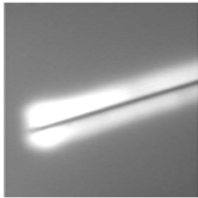
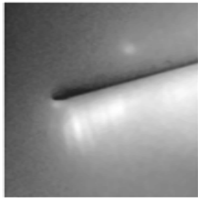
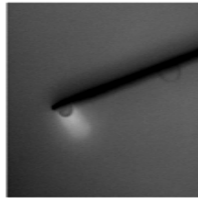


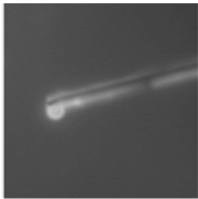
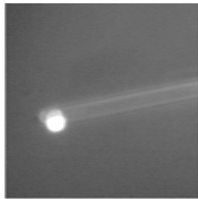
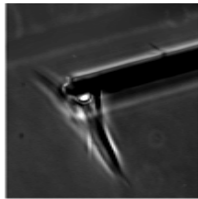
#### **5.2.1.1 Cantilever passivation**

For controlled force measurements it is mandatory to adsorb the actin polymerization factor N-WASP onto the colloidal probe exclusively. N-WASP must be avoided on the rest of the cantilever chip; otherwise the gel would grow in an uncontrolled manner on the entire chip (see Table 5-1). We decided to passivate the complete cantilever to make it protein repellent. After passivating, the probe can be attached to the cantilever, followed by incubation of the chip in N-WASP as usual (see section 4.1.). The passivating agent on the cantilever surface is then supposed to hinder N-WASP adsorption and actin gel growth on the

---

<sup>4</sup> Note, that the optimum technique was already thoroughly described in section 3.3. Here we present the experiments that lead to the optimum technique.

cantilever, while adsorption at the colloidal probe is still allowed. For biocompatible applications protein repellent surfaces are typically coated with BSA or PLL-PEG [124]. We study the effect of both agents, as well as different bead attachment methods in order to restrict actin polymerization to the colloidal probe. For attaching the probe, polystyrene beads are either glued or melted onto the cantilever. When gluing the bead is attached using epoxy glue. For attachment by melting, the polystyrene bead is heated above TG after placing the bead on the tip of a passivated cantilever by micromanipulation (melting at 120°C for one hour in a drying oven). Table 5-1 shows the resulting actin network growth on cantilevers prepared with the different procedures.

surface modification	none	BSA	PLL-PEG	none
sintered probe				
epoxy-glued probe				 (phase contrast)

**Table 5-1** AFM-cantilevers with N-WASP coated colloidal probes (10  $\mu\text{m}$  diameter) in the actin medium. The actin network is visualized via fluorescence or phase contrast (lower right image) 15 min after placing the cantilever in the actin medium. Effect of BSA/PLL-PEG passivation and the probe attachment procedure on actin polymerization: Although there is a passivating effect of BSA, actin polymerization is not completely inhibited on the cantilever surface. PLL-PEG passivation against actin polymerization was successful though. Best results are obtained when attaching the colloidal probe in buffer, which does not require cantilever passivation in order to hinder actin polymerization at the cantilever (see text).

As expected, the non-passivated cantilever adsorbs N-WASP and therefore recruits actin monomers over the entire area. Cantilevers coated with BSA show incomplete passivation towards N-WASP, especially at the bare silicon face of

the cantilever (no aluminum coating here). Passivation with PLL-PEG works well at both sides of the cantilever. Also the bead attachment methods affect the actin gel formation. Beads that were glued via epoxy in air show limited ability of actin network growth on the bead surface. In both cases no extended actin network formed within 15 min in the actin medium, while beads molten on the surface produce gels that grow in fast rates, about 2  $\mu\text{m}/\text{min}$ . It seems that the carboxyl-surface functionalization of the bead is damaged in close proximity of the epoxy glue due to volatile glue components. This results in reduced N-WASP adsorption, and therefore weak actin recruitment at the bead surface. Hence, attaching the bead in air with epoxy glue does not allow conducting the force measurement.

The combination of PLL-PEG passivation followed by of probe attachment via melting works reasonably well. Here an actin gel grows at the cantilever exclusively. However, a less laborious way to achieve actin polymerization is gluing N-WASP coated beads directly in solution. During this procedure a non-passivated cantilever can be used, as the N-WASP coated beads can be attached in a buffer solution that contains *no free* N-WASP. That is, the cantilever remains completely N-WASP free and the actin is allowed only to polymerize at the attached N-WASP beads. Also impurities due to the volatile components in the glue seem be less poisonous when attaching the N-WASP beads in solution. In fluid the release of the glue impurities might be diminished, which helps to remain the N-WASP coated surface active for actin recruitment. To summarize:

- a) Passivation of the cantilever in works with PLL-PEG, while BSA passivation is unreliable. However, the problem remains to keep the probe surface clean during gluing, or having to deal with laborious melting of the probe onto the cantilever instead of gluing.
- b) As a solution, we glue the N-WASP coated beads onto the cantilever in buffer. This method avoids glue-impurities being deposited on the bead and it does not require cantilever passivation either. The detailed procedure is described in 4.3.

### **5.2.1.2 Thermal drift of the setup**

AFM force-distance measurements have facilitated quantification of forces of single molecules down to the pN regime. However, sensitivity and stability issues owing to the thermal drift often limit AFM-based methods to quantify

systems that generate forces over long time. In other words, the sensitivity of force-time measurements is limited owing to the thermal drift of the setup. The thermal drift includes for example the thermal expansion/contraction of the glass slide, the AFM head or the piezos. This drift is hard to control and cannot be corrected with our setup. Here, it is mandatory to quantify the magnitude of the thermal drift because the AFM force-time measurements on actin networks take 10-20 minutes. In this time span the cantilever/glass slide distance must be constant. To evaluate the magnitude of the thermal drift we performed a number of reference measurements using the same experimental configuration as for the experiments with actin. We use the same buffer, liquid cell, cantilever type, colloidal probe, illumination source and intensity. We also apply the same instrumental steps with the AFM as during “real” measurements (see paragraph 4.3). Figure 5-13 shows some representative drift measurements. The measurements are performed in the x-buffer solution containing 1 mg/ml BSA and 7 $\mu$ M g-actin. This is the standard medium as used in the actual actin force measurements. The medium merely lacks the auxiliary proteins and the N-WASP coating of the colloidal probe. As can be seen from Figure 5-13 the upper limit of the cantilever deflection drift is 25 nm/min. The actin induced cantilever deflection rate is usually a magnitude larger, typically 300 nm/min. Therefore the contribution of the thermal drift to the measurement with the actin network can be considered negligible.

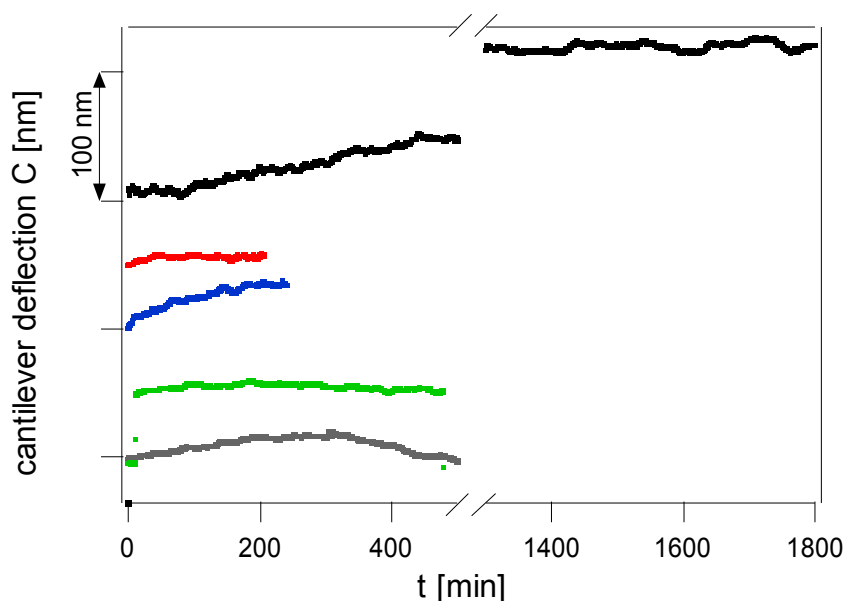


**Figure 5-13** Cantilever drift measurements. At  $t=0$  min, the cantilever is set to the surface to obtain an initial deflection of about 300 nm. Due to the thermal drift, the deflection of the cantilever is changing over time. The change in cantilever deflection over time is shown in the figure, which gives a direct measure of the thermal drift.

We also find that the drift is stronger in the beginning of an experiment. A possible reason could be protein adsorption onto the cantilever [125] after injecting the actin/BSA mixture to the liquid cell. Typically, this type of drift is visible from  $t = 0$  to  $t = 300$  sec. However, also the growth rate of the actin network in the first minutes of the experiment is larger (600 nm/min) than the average growth rate. This minimizes the error caused by the increased drift directly after injection of the actin. In addition to protein adsorption the hydrodynamic drag or depletion forces might perturb the equilibration of the cantilever as the colloidal probe approaches the surface. However, these are short-time perturbations and also many magnitudes smaller [99] than the forces generated by actin polymerization. The creep of the z-piezo does not contribute to the observed drift because piezo positions are closed-loop corrected.

### 5.2.1.3 Quantitative Fluorescence Measurements

Quantitative fluorescence measurements served as a measure for the actin density in the gels. Although in epifluorescence image artifacts due to unclean optics are only a minor problem, the images have still to be processed with re-



gard to these artifacts. This is mainly to ensure that the fluorescence intensity measurements of the labeled actin gels are reproducible and comparable among each other. So in principle the same image correction procedures as for particle tracking apply here (section 5.1.1). However, for fluorescence imaging in conjunction with AFM measurements, it is impractical to perform a background correction as the measurement procedure leaves no time for finding a blank specimen section. Also, due to actin gel growth and the resulting increasing fluorescence intensity in the image area, a time averaged mean grey value cannot be used for normalizing the time series. As an alternative, for each of the successive images a section is chosen that defines the background intensity, followed by normalization of the full image with the mean grey value of the chosen section. Figure 5-14 summarizes the procedure as a step-by-step chart. The individual steps are explained in the following.

**Step1:** After the images stacks are taken via time lapse recording, the time-stacks are normalized using an internal grey value reference, i.e. the reference is already in the image to be normalized. We use the cantilever area (see Figure 5-14, step1) as an internal reference, because a) the volume of fluorescent under the cantilever is constant during the experiment, whereas in the bulk solution there is always the chance for changes in height and disturbances due to air bubbles; b) the cantilever is always centered in the image, therefore the illumination is similar in different experiments. For the computation part of the normalization and ImageJ macro was written (see appendix 8.2.)

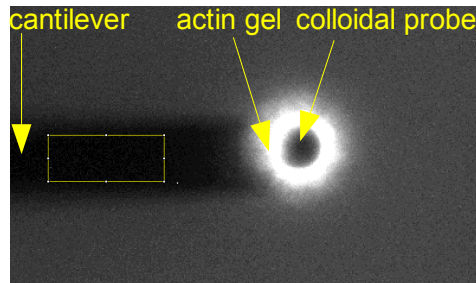
**Step2:** Next, the fluorescence intensity profiles from the normalized images are plotted. The profiles are always plotted radially from the probe center to the outer gel boundary. However, instead of averaging over the complete gel circumference, only the profile plots remaining in the cantilever area are collected (see Figure 5-14, step2). This is again due to better reproducibility of the fluorescence signal in the cantilever section.

**Step3:** Finally the lateral gel thickness  $h_l$  is calculated using the fluorescence intensity vs. radial distance plots (radial profile plots). Here the actin gel density and the fluorescence intensity decrease gradually from the bead surface. This means, there is no sharp gel boundary. Therefore, we have to define the gel boundary by taking into account the maximum intensity at the bead surface and the minimum intensity in bulk. We define the gel boundary at the radial position where the maximum fluorescence intensity is decreased to 25%. This is a well defined criterion that does not require absolute intensities and therefore also

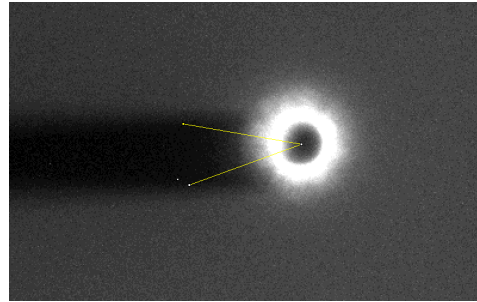
## 5. Results and Discussion

works when comparing different gel compositions (varying densities and branching). Some issues in qualitative fluorescence measurements remain. For example the focus positions are not precisely met between different experiments. Also, if the gel thickness in z-direction (focal axis) is increased the gel appears to be denser, because more light from other focal planes is detected.

1. Choosing the reference section (yellow rectangle at the cantilever) and normalization of the whole image with the reference section mean grey value.



2. Generating the radial profile plot via integration over all profile plots in the highlighted angular section under the cantilever.



3. Evaluation of the profile plot, (grey value vs. radius). The outer gel lateral boundary is defined at the position where the grey value has decreased to 25% of its maximum. The lateral gel thickness  $h_l$  is then calculated by subtraction of the bead radius from the outer boundary.

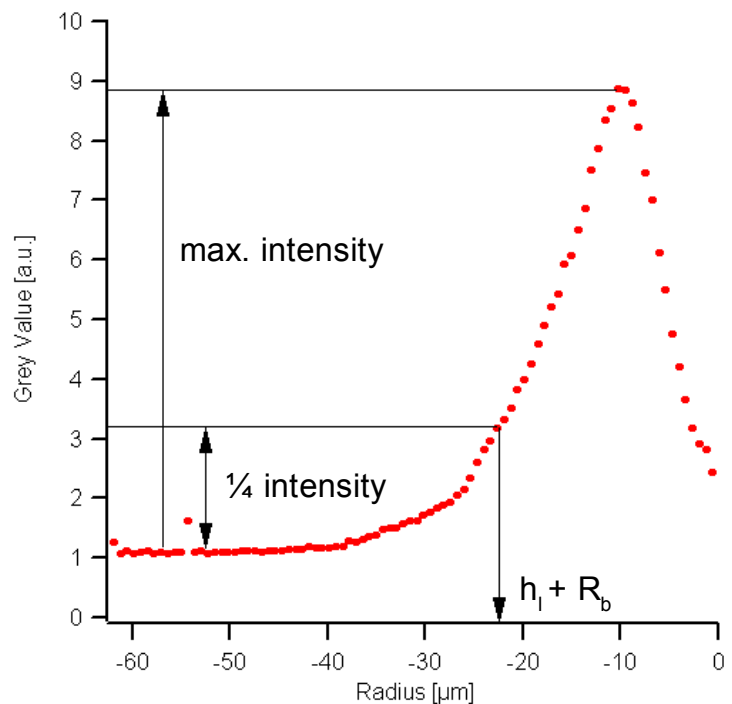


**Figure 5-14** Step-by-step chart of the fluorescence image analysis procedure.

### ***5.2.2 AFM Force Measurements for Varying Gel Size and Curvature***

In this study we aim for measuring the force generated by actin polymerization directly. More specifically, we strive to understand scaling of the force with the gel size and the effect of the geometry (curvature) of the gel. The colloidal probe radius controls the curvature of the nascent gels. It is known that, the gel curvature affects the internal mechanical stress of the expanding gels [6, 67, 71], as shown in section 3.5. Furthermore, it is argued that the mechanical stress counteracts the generation of force by limiting the gel growth [6]. Here we want to directly test this hypothesis and measure the force associated with the gel-growth limitation due to the mechanical stresses. First we describe the experiment, and then we present the results and finish with the discussion section. The following list shows the structure of the subchapters:

#### **Experimental Results**

- 5.2.2.1 Measurement Conditions, p. 91
- 5.2.2.2 Qualitative observations, p. 94
- 5.2.2.3 Force measurements, p. 97
- 5.2.2.4 Fluorescence intensity measurements, p. 100
- 5.2.2.5 Fluorescence intensity measurements to test for force induced gel deformations, p. 103
- 5.2.2.6 Detecting Mechanical Stresses in the Gel, p. 105

#### **Discussion**

- 5.2.2.7 Scaling of the Maximum Forces with the Gel Size, Estimation of the Y-Module, p. 106
- 5.2.2.8 The Generation of Force is Limited by Internal Stresses , p. 109
- 5.2.2.9 Perspectives, p. 112
- 5.2.2.10 Summary, p. 115

#### ***5.2.2.1 Measurement Conditions***

Table 5-2 shows the exact actin medium composition and the different beads used as colloidal probes in this AFM study. When preparing and initializing the experiment as described in section 4.3, the actin filaments start to grow at the (g-actin|ARP2/3|N-WASP) complex bound to the surface of the colloidal probe. The resulting actin network remains localized at the N-WASP coated surface by transient bonds between the filaments and the surface bound N-WASP. There-

fore the actin gel is allowed to grow only between the flexible cantilever and the glass substrate (Figure 5-15). This is achieved by a N-WASP coated probe attached at the apex of the cantilever, see previous section. So in our experiment, the entire actin gel is held steady to the flexible cantilever by its filament barbed ends connected to the activated bead, which itself is fixed at the cantilever apex. The composition of the actin medium is chosen such to allow for fast expansion of the gel ( $\approx 1\mu\text{m}/\text{min}$ ) and to overwhelm the thermal drift of the setup ( $<20\text{ nm}/\text{min}$ ).

components	bead preparation		medium composition (proteins)				
	N-WASP	beads	F-actin	ADF	profilin	gelsolin	ARP2/3
concentration	0.8 $\mu\text{M}$	$2.5 \times 10^9$ $\mu\text{m}^2/\text{ml}$	7 $\mu\text{M}$	2.3 $\mu\text{M}$	2.4 $\mu\text{M}$	0.1 $\mu\text{M}$	0.1 $\mu\text{M}$
probes (names)	21 $\mu\text{m}$	10 $\mu\text{m}$	5 $\mu\text{m}$				
exact diameter	21.2 $\pm$ 0.5 $\mu\text{m}$	9.65 $\pm$ 0.39 $\mu\text{m}$	5.47 $\pm$ 0.39 $\mu\text{m}$				
bead material	silica	PS	PS				

**Table 5-2** Actin in-vitro medium composition for the experiments with varying bead radius. The concentration in the “bead” column represents the surface concentration of the beads in the N-WASP solution during incubation. In this text the probes are named according to their rounded diameter. The term “PS” denotes polystyrene beads.

In the course of the experiment the cantilever bound gel grows around the colloidal probe, increasing its thickness. The actin gel between the colloidal probe and the glass substrate will extend against the cantilever and deflect it, see Figure 5-15. The force that is exerted by the extending gel is measured using the actin growth-related cantilever deflection, which is accessible in nanometer precision by the AFM’s optical lever technique. This AFM colloidal probe setup provides a well controlled sphere/plate geometry that avoids ambiguities by the tilt angle of the cantilever and uncontrolled directionality of actin network growth. The versatility in colloidal probes allows us to easily vary the probe size. Hence we can control the surface curvature of the actin recruiting surface and so the curvature of the gel. In parallel with the force measurement, the setup permits recording of the dye-labeled actin gel using epifluorescence microscopy. In combining fluorescence microscopy and AFM we are able to determine

of the lateral gel extension ( $h_l$ ) and the deflection of the cantilever which corresponds to the vertical gel extension ( $h_v$ ), see Figure 5-15C.

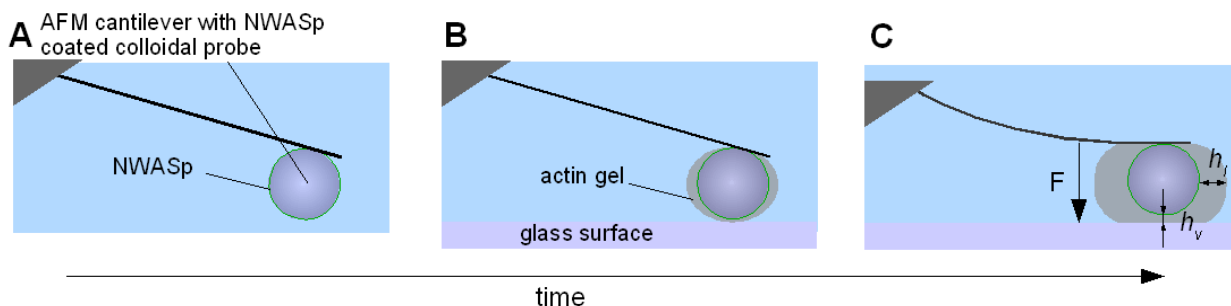


**Figure 5-15** Actin gel growth from an AFM colloidal probe and force generation (A-C) schematic presentation of the measurement procedure. A) An N-WASP coated colloidal probe is glued in liquid to a tipless AFM cantilever; B) After addition of the actin medium the probe is approached to the glass slide surface; C) As the actin gel extends from the colloidal probe, it deflects the cantilever, which is used as a measure of force. The restoring force of the cantilever is directed against vertical growth of the actin gel. During force data collection; the cantilever position is kept at constant height. The parameters  $h_l$  and  $h_v$ , respectively denote the lateral and vertical gel thickness.

We decided to perform force assays on spherical gels to gain insight into the role of geometry induced mechanical stresses. Also the sake of reproducibility it is advantageous to perform the force measurements on *spherical* actin gels growing radially around the colloidal probe. This ensures that force-induced sliding of the gel is prevented, thus rendering the measurement more reproducible. For *comet-shaped* actin gels (*Listeria*-like) at the colloidal probe, we observed sliding of the gels even at very small compressions (experiments shown in appendix 8.2, p. 142). The smallest force at which we observed comet sliding is on the order of  $0.05 \text{ nN}/\mu\text{m}^2$ , which is more than two orders of magnitude less than the potential polymerization force of actin networks [55, 57]. Therefore, the AFM force measurements on actin networks will not give any insight in the polymerization forces, unless the gel sliding is hindered. Consequently, we aim to perform the experiment such that the gel geometry stays spherical. If the gel does break, gel sliding would occur under immediate breakdown of the forces. The conditions allowing us to produce spherical actin gels, and further means to sort out sliding gels, are shown in the following.

### 5.2.2.2 Qualitative observations

To avoid gel sliding, we focus on the timeframe where the actin gel does not form a comet, but stays uniformly growing around the probe. Therefore we use larger beads, where the actin gel needs a longer time to reach the critical thickness where breaking occurs [71]. However, for the gel composition used in this experiment we still observe premature gel breaking for about 50% of the beads. We use the term “premature” because these gels break before they have generated their characteristic maximum force. We can differentiate between two different cases: a) breaking gels, not suitable for force measurement, and b) stable gels that generate reproducible force data.

a) Gel breaking immediately leads to a drop in the force generated by the gel, because the broken gels starts to slide under the compression of the cantilever. Crack induced gel sliding is shown for one example in Figure 5-16. Here small dents in the gel grow larger over time, leading to a crack that crosses from the outer boundary through the center of the gel, see Figure 5-16 at times  $t = 25$  and  $t = 37$  min. This finally leads to motion of the gel and formation of twin-comets. In our conditions the occurrence of a gel break has a stochastic character and the respective runs are not considered for the data evaluation. In many ways the observed gel breaking is similar to the symmetry breaking of free beads in bulk solution, see section 3.5.2. In contrast to the symmetry break of beads in bulk, the symmetry of the cantilever bound gel is already broken. At the attachment point of the cantilever the gel thickness vanishes and therefore forms a symmetry break. This predetermined symmetry break generally reduces the mechanical stress in the gel as compared to an actin gel in a state of perfect spherical symmetry. We have to consider such effects if we model the stress distribution in actin gels.

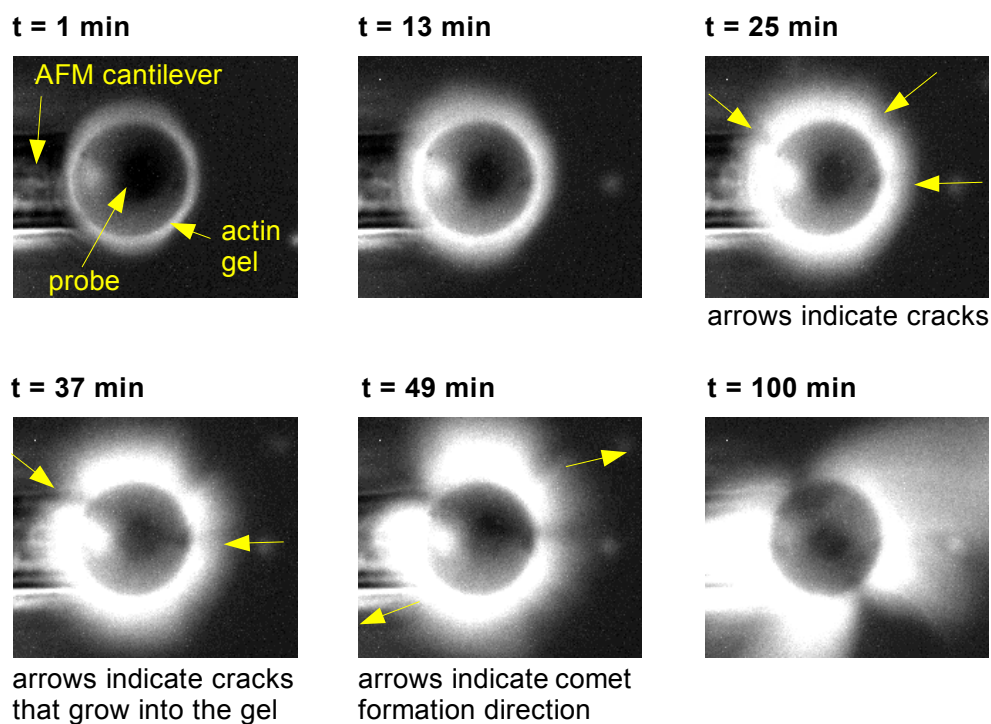


**Figure 5-16** Fluorescence micrograph of an evolving crack. The actin gel first grows radially at a silica probe with a radius of  $21 \mu\text{m}$ . At the point ( $t=37$  min) where the crack propagates to the center of the imaged bead, which is the section between the bead and the surface, the force detected by the cantilever drops immediately (data not shown). This kind of “force stalling” is due to crack induced motion of the gel. The occurrence of a crack has a stochastic nature. Therefore, measurement runs where these events occur are *not* considered for further data evaluation.

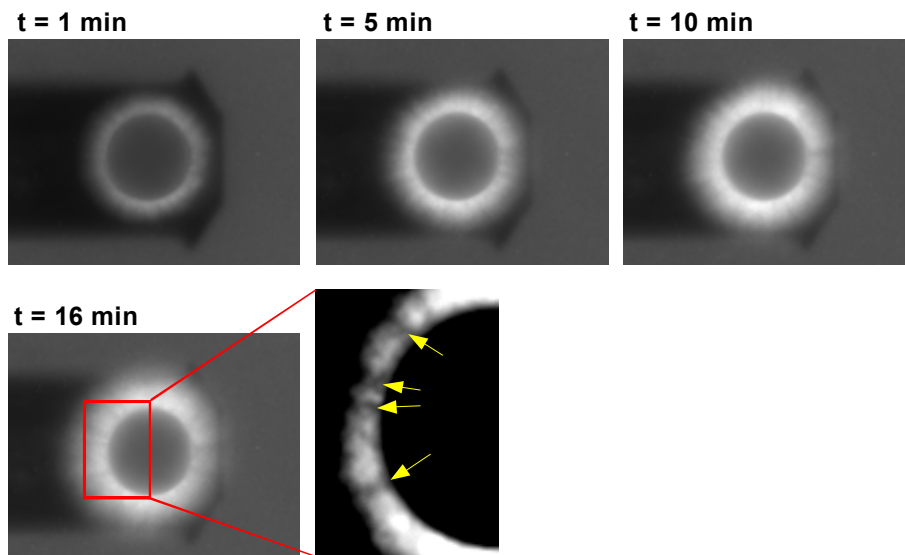


**Figure 5-17** Fluorescence micrograph of a stable, radially outwards growing actin gel. Note, there exist flaws in the gel (indicated by arrows) that however do not lead to gel breaking. The corresponding force and lateral gel thickness curves for the gel shown here level off at about 14 min, see Figure 5-18.

b) Stable gels grow regularly around the colloidal probe and do not break (Figure 5-17). Here the forces do not collapse by sliding of the gel under the compression of the cantilever. Therefore, the force curves generated by these gels are reproducible and can be drawn on to analyze the mechanical properties of the actin gel. Note however, that stable gels are still not homogeneous. The inset of Figure 5-17 reveals small cracks crossing the gel radially. Such defects might be crucial for the mechanical properties of the gel and have to be considered when analyzing elastic constants for example.

The question is whether the breaking/non-breaking behavior of the gels can be traced back to experimental parameters. We find that the different bead types (the probes) show a different propensity towards gel break. 75% of the 21  $\mu\text{m}$  probes (silica surface) and 30% of the 5  $\mu\text{m}$  probes break prematurely, while no breaking occurs for the 10  $\mu\text{m}$  probes (both 5 and 10  $\mu\text{m}$  bead surfaces are carboxylated polystyrene). Hence, the 21  $\mu\text{m}$  beads show a much higher gel-breaking probability, which could be due to a larger amount of defects on their surface. Another explanation could be a denser N-WASP coating on the silica surface. This, in turn, results in a denser and stiffer gel, having a higher propensity is to break in course of the measurement [71]. While the first explanation stems from mere microscopic observation of the silica beads, the latter explanation is in agreement with the results of the force and fluorescence measure-



ments, as shown in the following. Thus, there is indication that the gel grown from the silica beads is indeed denser as compared to the gels grown on carboxylated polystyrene beads. After the following section, fluorescence intensity measurements are presented to enlarge upon this topic.

### 5.2.2.3 Force measurements

The force data collection is started after addition of the actin and equilibration for a short time (2 min). The gels are approached to the glass substrate and compressed by an initial force of 5 nN. Once this initial compression is reached, the distance between bead and substrate is kept constant. Figure 5-18 shows one representative force measurement where we record the force  $F$  generated by the actin network and the lateral gel-thickness  $h_l$ . The force curve represents the deflection  $C$  of the cantilever in the vertical direction. Hence, gel growth in the vertical direction,  $h_v$ , can be also read from the force curve because:  $C = h_v$ . This measurement, and in fact the whole set of measurements, shows two distinct regimes. First, we observe a regime of constant force generation, i.e. a linear increase of the force. This suggests that the gel deflects the cantilever steadily and keeps growing constantly against increasing forces. At increased restoring forces of the cantilever *and* increased thickness of the actin gel, the stalling regime is reached, where the force generation diverges from the linear behavior. In this regime both, the force generation rate and the velocity of the vertical gel growth against the cantilever decreases. Finally, the force as well as the vertical gel growth generation stops completely. We find that  $h_v$  is decreased by a factor of 6 to 8 with respect to  $h_l$ . But the change of  $h_v$  and  $h_l$  coincides well with each other. This is reflected by the excellent match of  $h_v$  and  $h_l$  as function of time. The plot of  $F = k_c \cdot h_v$  against the  $h_l$  gives a straight line (Figure 5-18B inset), with  $k_c$  the spring constant of the cantilever. This confirms that the generated force  $F$  scales linearly with the lateral gel thickness  $h_l$  (Figure 5-18 inset).

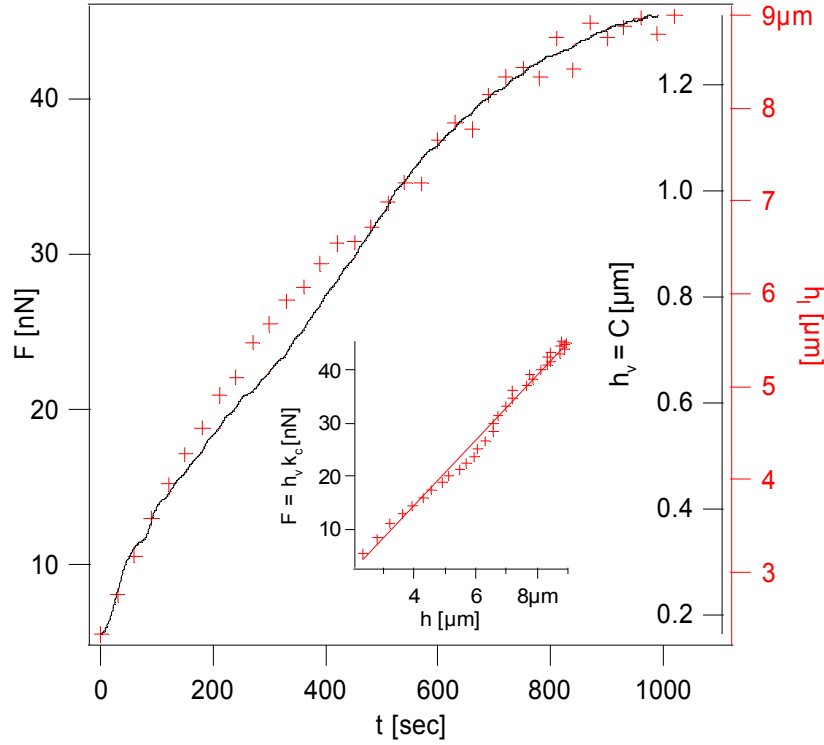


**Figure 5-18** The force curve (black line) and the gel thickness (red markers) to the growing actin gel shown in Figure 5-17. The second black axis on the left side of the graph shows the cantilever deflection  $C$  or the vertical thickness  $h_v$  of the gel. The force curve can be divided in a linear regime from  $t=100$  sec to  $t=600$  sec and a force stalling regime from  $t=600$  sec to  $t=1000$  sec. The same regimes are apparent in the lateral gel thickness curve  $h_l$  against time. Inset: Plot of force vs. lateral actin gel thickness  $h_l$  with a linear fit ( $R^2=0.994$ ) shows that force scales linearly with the gel thickness in the lateral direction.

We now proceed with testing the effect of different gel sizes on the force generation characteristics. We will see that all measurements, regardless of the bead size give the same qualitative behavior as the single measurement presented above. The gel size can be easily controlled by variation of the bead size. Here we measure the forces on colloidal probes with 5.5, 9.7 and 21.2  $\mu\text{m}$  radius. The maximum gel lateral thicknesses  $h_l^{max}$  are 5.8, 10.6 and 26.5  $\mu\text{m}$ , accordingly. The results of the force and lateral thicknesses  $h_l$  measurements are shown in Figure 5-19A and B, respectively.

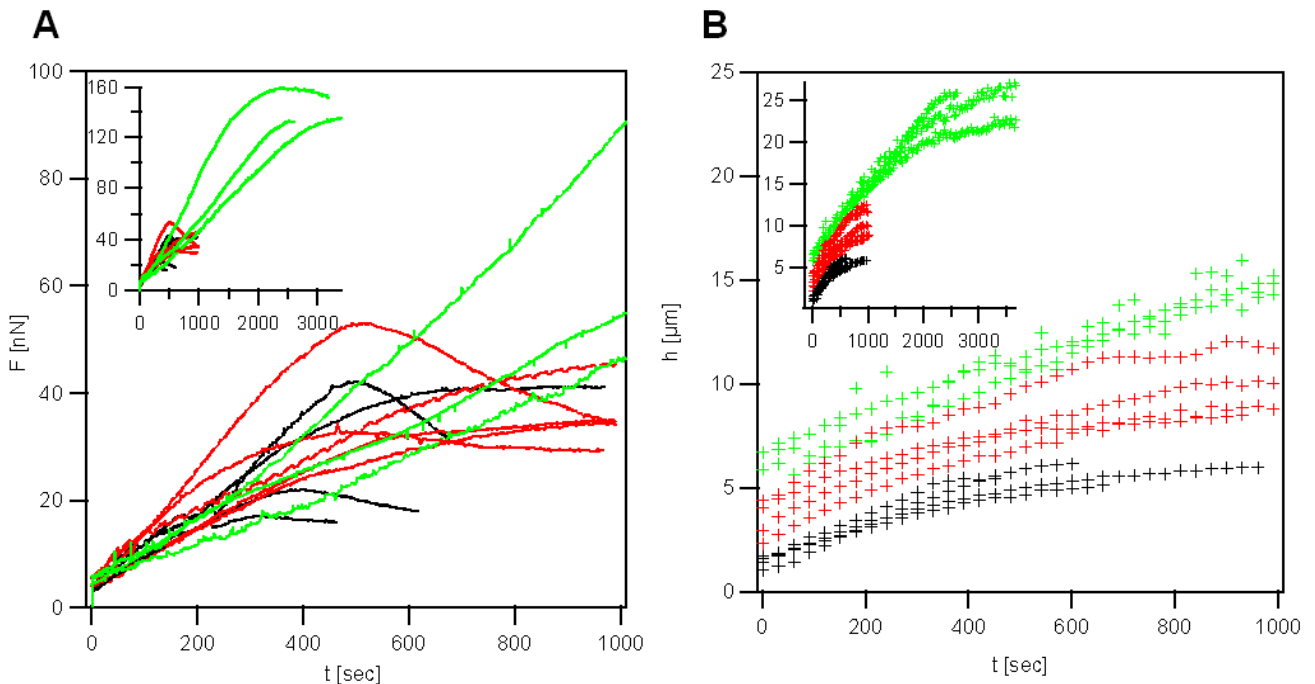


**Figure 5-19** A) Force vs. time plot for different probe radii: black 5  $\mu\text{m}$ , red 10  $\mu\text{m}$ , green 21  $\mu\text{m}$ . The inset shows the complete force range for the 21  $\mu\text{m}$  beads. B) Lateral actin gel thicknesses for the different probes. The gel growth speed is reduced at increased gel thicknesses and vanishes at the end of a measurement

The main observations from the force measurement and the corresponding lateral gel thicknesses measurements are emphasized in the following list:

- 1) All force curves, regardless of the bead size, show a linear regime initially, meaning that the force generation rate and the vertical gel growth rate are constant. The linear regime is followed by the force stalling regime, where both rates decrease and finally become zero.
- 2) Measurements performed in the same condition scatter significantly. For example, the stall force  $F^{max}$  may vary up to  $\pm 50\%$ , for the same type of bead. However, the slope in the linear regime is constant ( $6.9 \pm 1.7$  nN/sec), and clearly independent from the size of the gel.
- 3) The initial gel growth rate in the lateral direction varies between 0.9 – 1.4  $\mu\text{m}/\text{min}$ , where the rate is independent of the probe size. Contrary to the size-invariant initial growth rate, the time at which the growth rate starts to decrease clearly varies with the probe size. The growth rate leveling off occurs faster for smaller beads, see inset of Figure 5-19B. We observe no fur-

ther lateral gel growth after  $\approx 8$  min for the smallest and after  $\approx 30$  min for the largest probes.

- 4) For all force measurement runs, the lateral gel thickness  $h_l$  scales linearly with the force  $F$ . Thus, we also find the linear regime and the (force) stalling regime in the  $h_l$  vs. time plots, as shown in Figure 5-19B. Indeed, the  $h_l(t)$  and  $F(t)$  curves always match, see Figure 5-18 or Figure 5-21 for two representative examples.
- 5) A trend in the scaling behavior of the stall force  $F^{max}$  with the size of the gel is hardly visible due to the large scattering of the curves. That is to say, beyond the linear regime, the shape of the force curves becomes incoherent. Yet, it can clearly be seen that gels formed by the large 21  $\mu\text{m}$  beads produce also the largest stall forces ( $F^{max} = 142 \pm 14.3$  nN, averaged), which means that here the gels grow more persistently in the vertical direction and therefore obtain the largest vertical gel thicknesses  $h_v^{max}$ .
- 6) Differences in  $F^{max}$  and duration of the linear regime between the 10 and 5  $\mu\text{m}$  beads are not obvious:  $40.2 \pm 8.4$  nN for 10  $\mu\text{m}$ , and  $30.2 \pm 12.4$  nN for 5  $\mu\text{m}$  beads (both averaged). We may have to consider the actin density and the total number of actin filaments to explain the scaling of  $F^{max}$  with the gel size. To determine the effect of the varying gel density we perform fluorescence intensity measurements on the actin gel, as shown in the next subsection. The force scaling is discussed thereafter.

#### ***5.2.2.4 Fluorescence intensity measurements to determine the gel density***

We measure the fluorescence intensity to determine the density of the actin filaments with the aim to normalize the maximum force  $F^{max}$  for the different measurement runs. The force measurements are performed on different types of colloidal probes: silica 21  $\mu\text{m}$ , carboxylated polystyrene 10  $\mu\text{m}$  and 5  $\mu\text{m}$  (numbers indicate the radius). The different probe batches may possess a different surface chemistry. Clearly, there is a difference in surface chemistry for the silica and polystyrene probes. But even the two polystyrene probe-types may come with a different degree of carboxyl functionalization, which is often introduced by a not so well controlled carboxyl-surfactant/particle interaction during bead synthesis. In order to compare the polymerizing actin networks recruited by the different probe surfaces, we need to determine the effect of the surface

chemistry. As a test parameter we use the fluorescence intensity. The intensity may serve as an estimate for the density of the actin gel, and the quality of the surface functionalization. The purpose of this investigation is to normalize the obtained forces with the gel density, because the gel density is connected to the number of force generating actin filaments.

First we measure the area normalized intensity,  $I$ , of the gel that does not lie within the circumference of the colloidal probe (Figure 5-20B). Actin gel that protrudes over the cantilever is also not considered for data analysis as the background fluorescence of the bulk would otherwise spoil the measurement. The fluorescence intensity decays from its maximum value at the bead surface to the background value at the outer gel perimeter. We have to define a gel boundary, because the intensity decays gradually, showing no sharp boundary. The boundary, as shown in Figure 5-20B, is defined at the line where the intensity decays to 25% of the maximum intensity at the probe surface. The measurement procedure is explained in detail in section 5.2.1.3 (p. 88). Figure 5-20A shows the fluorescence intensity against time of the whole set of force curves. All fluorescence intensity vs. time curves grow steeply in the first 4 min after actin injection to the measurement cell. At a certain point in the experiment the fluorescence signal reaches a plateau value. The increase in fluorescence intensity indicates that the actin network does not only grow, but also densifies simultaneously. The final density of the actin network depends on the polymerization and depolymerization kinetics as well as on the degree of probe functionalization. As can be seen in Figure 5-20A, the plateau values scatter significantly for one probe type. Nevertheless, the differences between the probe types are larger, meaning that the probes indeed possess a varying degree of surface functionalization. This systematic change of actin density with the probe type has to be considered when comparing their force measurements.

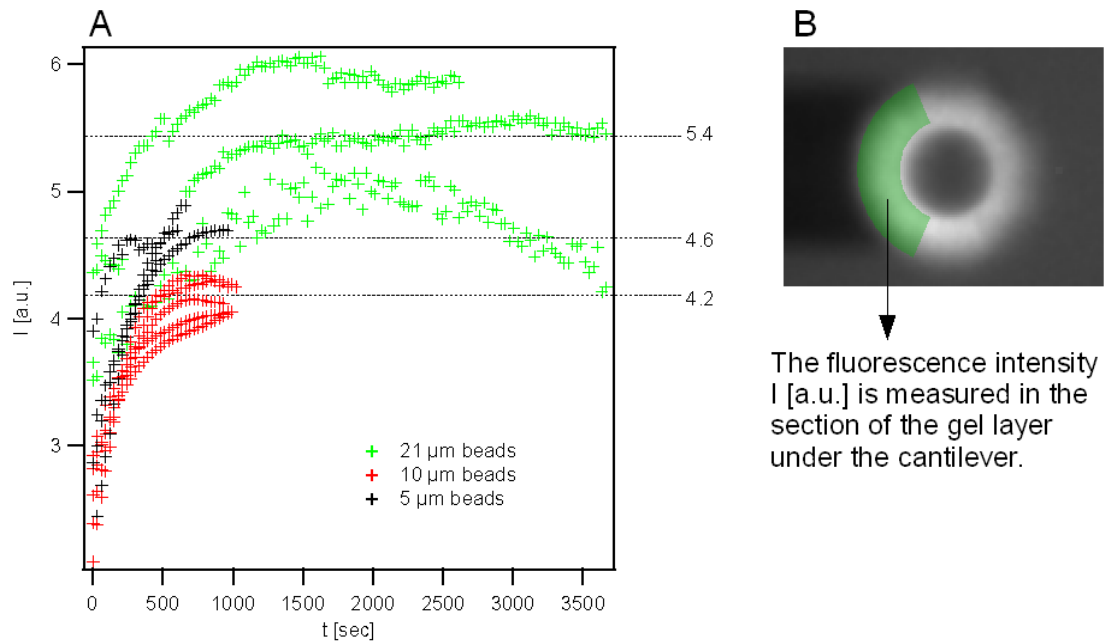


**Figure 5-20** Fluorescence intensity determination ( $I$ ) in the section that lies not in the circumference of the colloidal probe. This is a measure for the actin gel density during gel expansion. A) For all gels the fluorescence intensity increases over time and reaches a plateau value. As the actin gel polymerizes it does not only extend but also increases its density up to the plateau value. The plateau values, shown to the right of A, differ for the different probe types. The  $10\ \mu\text{m}$  probes show smallest densities, while the  $21\ \mu\text{m}$  silica probes show the largest densities. B) indicates the area the fluorescence intensity measurement.

The actin density indicates the number of force generating actin filaments. Indeed we observe that the density of actin affects the maximum generated force  $F^{max}$ :

- a) The  $10\ \mu\text{m}$  polystyrene probes generate gels with lower fluorescence intensity ( $I = 4.2$ ) as compared to the  $5\ \mu\text{m}$  polystyrene probes ( $I = 4.6$ ). The fluorescence intensity data suggests that the actin gels generated by  $10\ \mu\text{m}$  beads are less dense and therefore mechanically weak. This could explain why the maximum force that gels of both types generate is in the same range ( $F^{max} \approx 30$  and  $\approx 40$  nN, see above). In a simple picture this is not expected, because the  $10\ \mu\text{m}$  bead should possess four times more pushing actin filaments than the  $5\ \mu\text{m}$  beads and therefore generate four times larger forces.
- b) The silica probes,  $R_{bead} = 21\ \mu\text{m}$ , show the largest fluorescence intensity value of  $I = 5.4$ . These gels also produce the largest forces ( $F^{max} = 142$  nN): If simply scaling with the number of actin filaments, the  $21\ \mu\text{m}$  probes

should produce forces four and eight times larger forces than the 10 and 5  $\mu\text{m}$  probes, respectively. We find such a scaling behavior for the 10  $\mu\text{m}$  probes, but not for the 5  $\mu\text{m}$  probes, even after normalizing with the fluorescence intensity. Thus, here again the simple force/bead-surface scaling does not apply.

The fluorescence intensity measurements suggest that the actin gels are not evenly dense at different probes and even at probes of the same type. This explains the large shifts of  $F^{max}$  for gels growing at the same probe type. The normalized forces  $F^{max}/I$  do not scale with the surface area of the probe ( $\propto R_{bead}^2$ ) but rather with the square of the gel size  $R_{gel}^2$ , as will be shown in subsection 5.2.2.6.

#### ***5.2.2.5 Fluorescence intensity measurements to test for force induced gel deformations***

Although the actin gels seem stable at first glance, we have to test whether the gels hold their position at increasing compressions by the cantilever during gel expansion. It is possible that the gel stops to extend against increased cantilever restoring forces simply because the most stressed part of the gel (at the apex of the probe) starts to deform and is pushed away from the apex of the probe. This would directly decrease the force against the cantilever, because the cantilever could resile to the position of the deformed gel. Such a behavior resembles a stress induced-material failure of the actin gel.

Using the fluorescence micrographs, the actin gel density is evaluated in the section between the colloidal probe and the glass substrate. Consequently, the evaluated section lies within the circumference of the colloidal probe, as shown in Figure 5-21B. Averaging over this section gives the “inner” fluorescence intensity  $I_{in}$ . This fluorescence measurement shows whether the actin gel is moving due to the increasing compressive force imposed by the cantilever. For increased compressions, the actin gel could move radially outwards (with respect to the probe apex). The gel density as indicated by the fluorescence intensity would then decrease accordingly. If this actin filament transport takes place, the forces would decrease as if exceeding the yield point of a strained material.

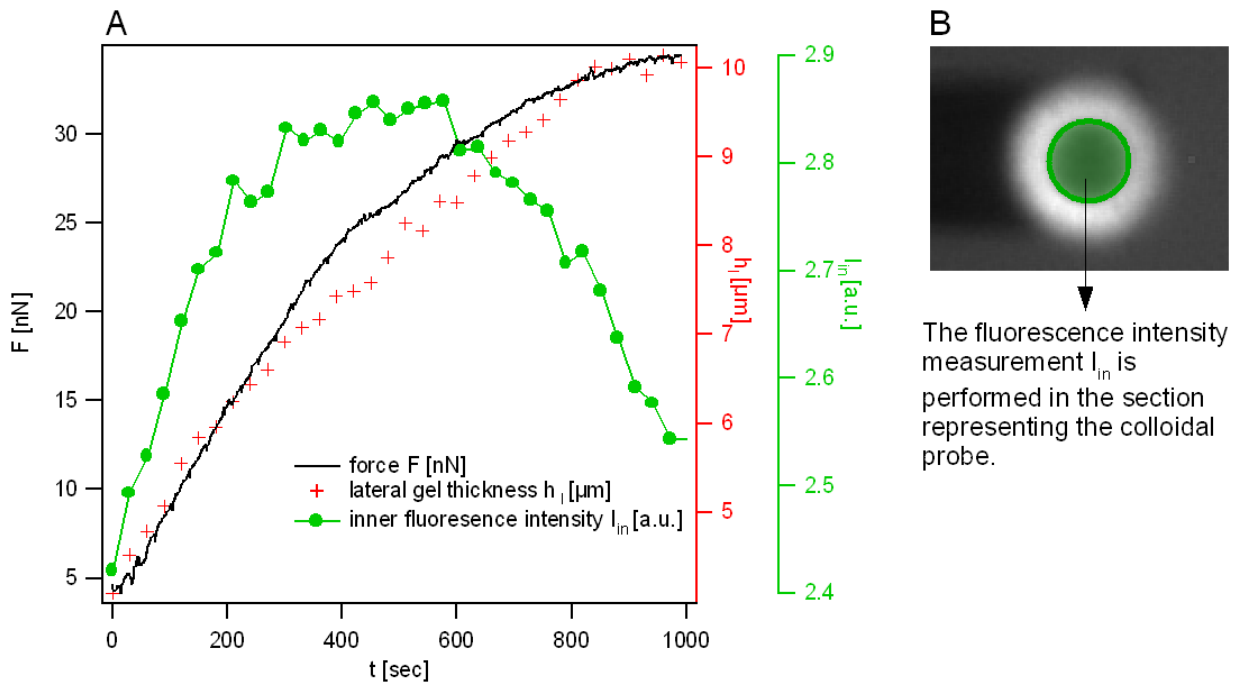


**Figure 5-21** Fluorescence intensity evaluation within the boundary of the colloidal probe ( $I_{in}$ ) for growing actin gels. The respective section is highlighted in B. A) Another typical force curve (black) with the corresponding measurements of the lateral gel thickness  $h_l$  (red markers) and fluorescence intensity  $I_{in}$  (green line with markers). Note, that  $h_l$  agrees well with the force curve, while  $I_{in}$  does not.

Figure 5-21A shows  $I_{in}$  as a function of the time  $t$  after starting the actin polymerization. As can be seen,  $I_{in}$  first increases and reaches a maximum at 400 sec before it decreases until the end of the measurement. We explain the increase in  $I_{in}$  early in the measurement as due to actin network densification caused by actin polymerization. This was also observed for the previous fluorescence intensity measurement, conducted outside of the probe circumference. The decrease in fluorescence intensity after 600 sec means that gel density decreases, which could indeed be interpreted as stress induced transport of actin to the outer shell of the gel. However, the effect is rather small,  $I_{in}$  changes by only 20% in the course of the measurements. Furthermore, at the time where  $I_{in}$  starts to decrease the force still increases, so that the effect of the possible material transport on the force  $F$  is negligible. This is also reflected by the fact that the force curve does not match with  $I_{in}$  as can be clearly seen in Figure 5-21A. Hence, the force stalling is not due to deformation of the gel. This was proven



by measuring only small changes in  $I_{in}$  and finding no agreement between  $I_{in}(t)$  and  $F(t)$ .

#### **5.2.2.6 Detecting Mechanical Stresses in the Gel**

Due to their spherical geometry the actin gels might generate stresses as they expand, see section 3.5 p.28. These internal stresses could be responsible for the limitation of the gel growth and generation of force. Another possibility for growth constraints are diffusion limitations of monomers to the bead surface. To distinguish between these two possibilities it is necessary to test whether the actin gels are under mechanical stress.

First we perform a direct test on a gel that has generated its maximum force, being unable to move the cantilever further. In this situation, we quickly withdraw the cantilever over a defined distance and measure the response of the gel. Figure 5-22A shows a force curve of a 5  $\mu\text{m}$  of bead that stops growing at a vertical gel thickness of 1  $\mu\text{m}$ . As seen in the previous experiments, the lateral gel extension is 6-8 times higher. If we now withdraw the z-piezo by 1  $\mu\text{m}$  upwards, the cantilever deflection  $C$  decreases as expected by roughly 1  $\mu\text{m}$ . In the following, the actin gel extends very fast in the vertical direction,  $C$  and  $h_v$  increase instantaneously by 200 nm after withdrawing the cantilever. The gel literally snaps back which can only be explained by fast elastic gel expansion and not by slow actin polymerization. However, the actin gel does not fully recover to the 1  $\mu\text{m}$  cantilever deflection, as it extends only by 0.5  $\mu\text{m}$  in  $h_v$  after cantilever withdrawal. For that reason the apparent strain in the vertical direction ( $h_l^{max} - h_v^{max}$ ) cannot be completely explained by the compression of the cantilever. Seemingly, the diffusion of actin monomers to the volume between the glass slide is reduced with respect to gel compartment facing to the surrounding actin medium. This keeps the vertical gel thickness  $h_v^{max}$  small compared to the lateral gel thickness  $h_l^{max}$ . Nevertheless, the results so far clearly show that the gel is in a state of elastic tension.

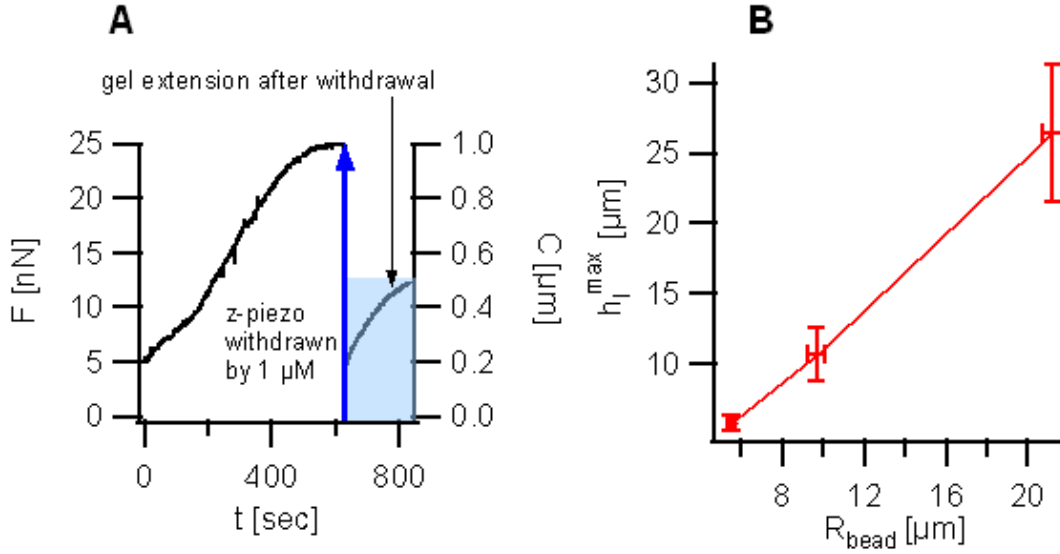


**Figure 5-22** The actin gels are governed by internal elastic stresses. A) Actin force generation stops due to cessation of the vertical growth. The gel shows fast vertical expansion after withdrawal of the cantilever due to release of mechanical tension. The gel pushes the cantilever by 200 nm instantaneously after withdrawal. The final vertical gel extension  $h_v^{\text{max}}$  is 1.5  $\mu\text{m}$ , from  $h_v = 1 \mu\text{m}$  before cantilever withdrawal plus  $\Delta h_v = 0.5 \mu\text{m}$  after withdrawal B) Maximum (stationary) gel thickness in the lateral direction  $h_l^{\text{max}}$  as function of the bead radius shows a linear behavior. This shows that  $h_l^{\text{max}}$  is limited by elastic stresses, not by diffusion limitation.

Another indication for elastic tension can be found by analyzing the scaling of maximum lateral gel thickness  $h_l^{\text{max}}$  with bead radius  $R_{\text{bead}}$ . If the gel growth was diffusion limited,  $h_l^{\text{max}}$  would be insensitive towards changes in  $R_{\text{bead}}$ . In case of elastic limitation,  $h_l^{\text{max}}$  scales linearly with  $R_{\text{bead}}$ , see Eq. 3-17, p. 34. Here we find such a linear scaling as shown in Figure 5-22B where  $h_l^{\text{max}}$  is plotted against  $R_{\text{bead}}$ . This proves that  $h_l^{\text{max}}$  is limited by elastic stresses rather than limited by diffusion. Such a linear behavior was already found in previous studies [67, 71], where symmetry breaking and comet formation were studied in similar conditions.

### 5.2.2.7 Scaling of the Maximum Forces with the Gel Size, Estimation of the Y-Module

As the actin gel grows it generates a force against the cantilever, while the cantilever imposes a restoring force on the actin gel. This restoring force compresses the network and therefore reduces the vertical gel thickness  $h_v$ . In con-

trast to  $h_v$ , the lateral gel thickness  $h_l$  remains unaffected by cantilever compression. Hence,  $h_v$  and  $h_l$  represent the gel in a compressed and uncompressed state, respectively. We now treat the gel as an elastic spring that is compressed by  $h_l - h_v$  and test if the gel shows an applied force-size scaling similar to that of a homogeneous elastic body. We start with discussing elastic relations of the cantilever and the actin gel. The elastic deformations in the AFM experiment can be described in the same way as in paragraph 3.7.2, which presents a basic AFM experiment on an elastic substrate. The elastic potential of the complete system, deformed cantilever with actin gel, can be described as a series of two springs:

$$V = \frac{k_c}{2} C + \frac{k_g}{2} (h_l - h_v) \quad \text{Eq. 5-1}$$

where  $C$  is the deflection of the cantilever,  $k_c$  its spring constant,  $k_g$  the apparent stiffness of the actin gel with  $h_l - h_v$  the gel deformation. In mechanical equilibrium ( $V = 0$ ) and since  $C = h_v$  we can solve for  $k_g$ :

$$k_g = \frac{k_c h_v}{h_l - h_v} \quad \text{Eq. 5-2}$$

Assuming the gel is a homogeneous elastic body, the elastic modulus of the gel is  $Y = k_g L / A$ , where  $L$  is the length of the gel and  $A$  its cross-sectional area [126]. If we further assume  $L = h_v$  and  $A \propto (h_l + R_{bead})^2$  the elastic modulus  $Y$  can be written as:

$$Y \propto \frac{k_g h_v}{(h_l + R_{bead})^2} \quad \text{Eq. 5-3}$$

With  $F = k_g (h_l - h_v)$  and  $R_{gel} = h_l + R_{bead}$  the scaling of the force with  $R_{gel}$  is:

$$F \propto Y \cdot R_{gel}^2 \frac{h_l - h_v}{h_v} \quad \text{Eq. 5-4}$$

Hence, the force  $F$  scales with the square of the gel radius  $R_{gel}^2$ . The ratio between  $h_v^{max}$  and  $h_l^{max}$  is roughly constant between all experiments,  $h_l^{max}$  is 6-8

times larger than  $h_v^{max}$ . Also the gel composition was kept constant throughout the measurement, meaning  $Y$  is a constant too. Therefore Eq. 5-4 allows us to combine the individual measurements in form of a master plot, depicting maximum forces  $F^{max}$  against the square gel maximum radius  $R_{gel}^{max\ 2}$ . Figure 5-23 shows that this plots results indeed in a linear curve as predicted by Eq. 5-4. This shows that all the different measurement runs can be expressed by linear elastic deformation of the actin gel due to its self-generated force.

It is tempting to extract the Young's Modulus  $Y$  from the plot in Figure 5-23, or from the ratio of  $h_v$  and  $h_l$ . However, the gel geometry is not exactly known as it does not show a sharp boundary (section 5.2.2.4). Therefore we can only estimate the apparent modulus, which is on the order of 30 Pa. This value is two orders of magnitude smaller as compared to measurements on actin comets [55] in similar medium composition. The error due to the gel diffuse boundary should account for errors that change the modulus by a factor of 2. Hence, an enormous difference between the  $Y$  estimation here and on actin comets remains. However, the  $Y$ -module in actin comets is anisotropic as the filaments are polarized, which is not the case here (see Figure 3-2, p.15). The  $Y$ -module as measured by [55] must be larger because it was measured by longitudinal comet deformation, parallel to the filaments. Furthermore, due to volume conservation, the actin comets are denser than spherical gels. Also the observed defects in the gel (Figure 5-17, p. 96) should render the gel more compliant.

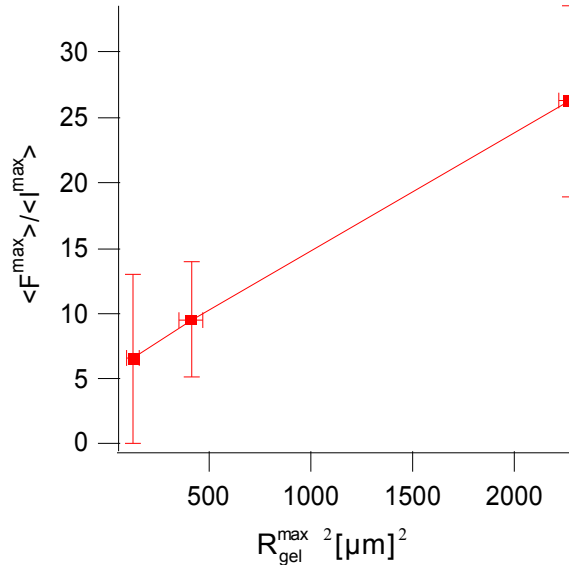


**Figure 5-23** The maximum normalized forces  $F'^{max}$  is plotted against the square gel maximum radius  $R_{gel}^{max 2}$ . We find that  $F'^{max}$  is proportional to  $R_{gel}^{max 2}$ . The data points are averages over different runs with the same type of bead. The error bars represent the respective standard deviations.

We should also consider that actin networks are elastic materials and therefore polymerization at the colloidal probe results in both compression of the supporting gel and deflection of the cantilever. Therefore the force measured by the AFM is not the total force produced by the gel, but only the fractional amount transduced to the cantilever. The fractional amount can be calculated according to  $k_g / (k_g + k_c)$ , where  $k_g$  is the spring constant of the gel and  $k_c$  the spring constant of the cantilever. According to Eq. 5-4  $k_g$  is on the order of 0.006 N/m, a factor of 5 smaller than  $k_c$ , meaning that only 17% of gel growth is transduced into cantilever deflection. For estimating the stresses in the gel one should consider this fact. Stiffening the gel via increasing its density greatly increases the ability of the gel to generate forces against a load, as will be shown in 5.2.3.

#### ***5.2.2.8 The Generation of Force is Limited by Internal Stresses due to the Spherical Gel Geometry***

As already described, the force curves are linear first before reaching the stall regime. The lateral gel extension shows the same behavior, it slows at the same time as the force generation. This raises the question whether the slowed

actin gel growth is the reason for the limitation of force. The experiments show that we can rule out other force-limiting mechanisms:

a) The actin gel is *not* pushed away by compression forces of the cantilever. As shown section 5.2.2.5, the gel density stays constant even at the site of largest compression which is the apex of the probe facing the substrate. This means, the gels are stable and the cantilever is not allowed to resile to the position of displaced gel, which would otherwise appear as breakdown of forces (see appendix 8.2).

b) The vertical gel growth is *not* hindered by the restoring forces imposed by the cantilever. If this was the case, the gel would keep growing in the lateral direction as (vertical) force production is limited. This is because the lateral direction is unopposed by the restoring forces of the cantilever. However the lateral ( $h_l$ ) and vertical ( $h_v$ ) gel extension stop simultaneously.

In fact, both parameters  $h_l(t)$  and  $h_v(t)$  agree very well, for the whole time-frame of the experiment (see Figure 5-18 or Figure 5-21). Therefore, the generation of force ( $F(t) = h_v(t)k_c$ ) must be limited passively, namely by the gel growth as indicated by  $h_l(t)$ .

Now we want to clarify the physical reason for the limitation of the gel growth. A limitation in gel growth and force production arises if the rate of monomer insertion is smaller than the depolymerization of the actin filaments. This is a very generic explanation and it applies even without forces directed against the growing network. In such a situation the gel growth could be limited by diffusion as argued by Plastino et al. [70]. However, it has also been shown that actin gel growth can be force dependent [6, 55]. Also the mathematical models on actin based force generation consider the gel growth as being force dependent. The Thermal Ratchet models (section 3.4) for example use the fact that at increased forces the probability of a gap large enough to insert an actin monomer is decreased, and so the gel growth is slowed.

There are two possible reasons for gel growth limitation, monomer diffusion and forces directed against the network growth. The experimental results indicate a force dependence of the gel growth. Figure 5-22A (p. 106) shows that the actin gel snaps back after releasing the compression. This points towards elastic gel tensions imposed by the cantilever. Also, the actin gel is able to polymerize vertically after releasing the compression. The best indication for mechanical stresses in the entire gel is given by the linear scaling of the lateral gel extension  $h_l^{max}$  with the radius of the bead  $R_{bead}$ . The origin of the stress is the spherical

geometry of the gel (Figure 5-24): New actin gel layers form at the bead surface, pushing previously grown layers further away from the probe. The layers are then stretched and impose a tangential stress  $\sigma_{\perp\perp}$  that grows with increasing distance from the bead surface. The tangential stress results in a radial stress that is maximum for the gel close to the bead surface. The associated forces of this internal stress are responsible for the cessation of gel growth at a limiting gel thickness  $h_l^{max}$ . This applies specifically for the lateral gel compartment that is not compressed by the cantilever which is why the gel growth can be considered stress-limited. For a free spherical actin gel, without an applied external force, this phenomenon has been described using linear continuum mechanics [6]. In the framework of this model the limiting gel thickness  $h_l^{max}$  was found to be scaling linearly with the bead radius  $R_{bead}$ . The plot of  $h_l^{max}$  vs.  $R_{bead}$  (Figure 5-22B) shows a linear scaling as well, proving the gel growth at the colloidal probe is limited by mechanical stresses.

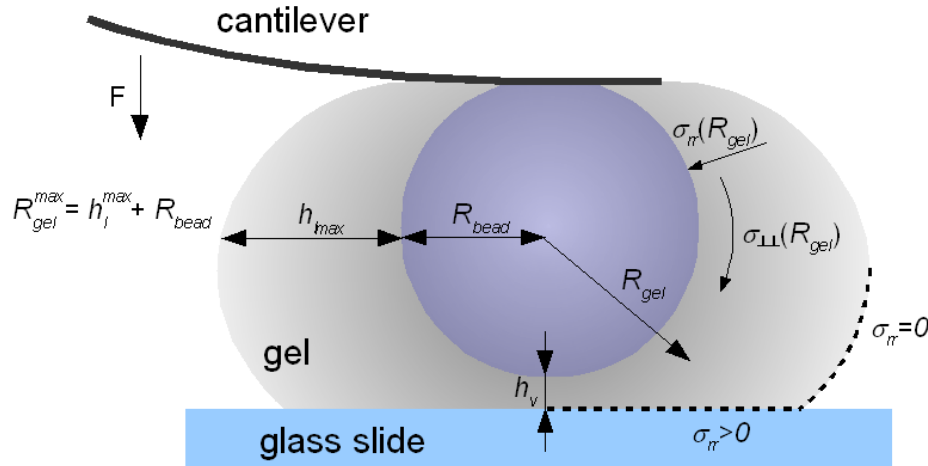


**Figure 5-24** Sketch of the mechanical stresses  $\sigma_{\perp\perp}$ ,  $\sigma_{rr}$  and other parameters used in the text to describe the state of an actin gel growing against a cantilever.

The mechanical situation of an actin gel grown on a spherical surface can be roughly compared to a pressurized vessel, see Figure 5-24. The tangential component  $\sigma_{\perp\perp}$  are estimated as [66]:  $\sigma_{\perp\perp}(R_{gel}) = Y(R_{gel} - R_{bead})/R_{bead}$ , meaning  $\sigma_{\perp\perp}$  is maximum at the gel surface and vanishing at the bead surface and proportional to the bead curvature  $1/R_{bead}$ . The radial stress  $\sigma_{rr}$  behaves the other way around, maximum at the bead surface, vanishing at the gel surface:  $\sigma_{rr}(R_{gel} = R_{gel}^{max}) = 0$ . However, this equation is only valid for the uncompressed gel compartment that grows laterally with respect to the cantilever.

For the gel compartment that grows vertically, the external force imposed by the cantilever compresses the gel and gives rise to  $\sigma_{rr}$  at the glass slide/gel contact area (Figure 5-24). This shows that the colloidal probe measurements yield the internal stresses  $\sigma_{rr}$  (due to spherical geometry) by the expanding actin gels. The actin gels generate pressures against the cantilever on the order of  $0.15 \text{ nN}/\mu\text{m}^2$ . Other groups obtained  $2 \text{ nN}/\mu\text{m}^2$  by measuring the forces on non-spherical, stress free, gels [55, 57]. This indicates that in our case the force production is counteracted by the internal gel stress, otherwise larger forces would be imposed by the actin gel against the cantilever. To assess these different results we would need to model the complete stress state,  $\sigma_{rr}(R_{gel})$  and  $\sigma_{\perp\perp}(R_{gel})$ . The force measurements conducted here give a first estimate of  $\sigma_{rr}$ .

### 5.2.2.9 Perspectives

We have seen that here the maximum forces reach only  $0.15 \text{ nN}/\mu\text{m}^2$  while theories [4, 5] and experiments [55, 57] arrive at stalling forces on the order of  $2 \text{ nN}/\mu\text{m}^2$ . So obviously the spherical, convex geometry of our force probes causes elastic stresses that keep the gel from generating larger forces. Such stresses appear also in actin gels generated in cells. For example the propulsion of the rod-shaped *Listeria* bacteria is based on radial stresses, generated by an actin gel with broken symmetry [5]. However in these gels there exists internal stress not contributing and even counteracting the propulsive force. It is argued that regulation of these stresses allows adjusting the propulsive force which could be advantageous for such organisms [5]. It is therefore worthwhile to map the complete stress state of the force generating gels studied here.

In this work however, we can only roughly estimate the internal elastic stresses. As a starting point we calculate the stalling stress of the gel at the point where it stops to expand and compare this stress with the linear elastic theory of actin network growth. For the experimental estimation we use the following observables: The maximum force  $F^{max}$  and the contact surface of the gel with the glass substrate  $A^{max}$ . The ratio  $F^{max}/A^{max}$  is the component of the stress which is transformed into deflection of the cantilever. We obtain stresses on the order of  $10^1$ - $10^2$  Pa, varying with the bead size, see Table 5-3. Theoretical examination now allows us to calculate the total stress that acts on the bead surface  $\sigma =$



face  $\sigma = \sigma_{rr}(R_{gel} = 0)$ , the derivation can be found in section 3.5. For the sake of convenience we repeat the final equation here.

$$\sigma = 2Y \left[ \frac{R_{gel}^2}{R_{bead}^2} \left( \frac{R_{gel}}{3R_{bead}} - \frac{1}{2} \right) + \frac{1}{6} \right] \quad \text{Eq. 5-5}$$

Here  $R_{gel}$  is the distance from the probe center and the edge of the gel and  $R_{bead}$  is the radius of the bead. Both  $R_{gel}$  and  $R_{bead}$  are determined by microscopy. We assume an elastic modulus of  $Y = 1000$  Pa of the actin gel as determined in [55] and [59]. Note, that we do not discriminate between the tangential  $\sigma_{\perp\perp}$  and the radial component of the stress  $\sigma_{rr}$  as we calculate the total stress acting on the bead surface, where  $\sigma_{\perp\perp} = 0$ . Table 5-3 shows the values for the inner stress that acts on the bead surface.

Bead (probe)	$F^{max}/A^{max}$ [Pa] (experiment)	$\sigma^{max}$ [Pa] (theory)
5 $\mu\text{m}$	94	2000
10 $\mu\text{m}$	39	2100
21 $\mu\text{m}$	25	2800

**Table 5-3** Estimation of the experimental internal stress and comparison to the theoretical value calculated using Eq. 5-5 with  $Y = 1000$  Pa and  $R_{gel}^2$  and  $R_{bead}^2$  taken from the measurement.

We find that the experimentally determined stresses are at least an order of magnitude smaller than the experimentally determined stresses. An agreement between both estimates cannot be expected because the theoretical estimation relates to the radial component of the stress directed on the entire bead surface, while the experimental estimation  $F^{max}/A^{max}$  yields the “outer” radial stress which is caused only by the external force  $F^{max}$ . In case of perfect symmetry (no external forces and compression of the gel) the outer radial stress vanishes. There are two factors explaining the significant differences between theory ( $\sigma^{max}$ ) and experiment ( $F^{max}/A^{max}$ ):

- 1) The stresses of the gel compartment not growing against the cantilever are not detected by the measurement, hence  $F^{max}/A^{max}$  is smaller than  $\sigma^{max}$ .
- 2) As discussed in 5.2.2.7 the apparent elastic modulus is a factor of 30 smaller than the elastic modulus used for the calculations here. Although the

true elastic modulus cannot be evaluated (uncertain gel geometry), it should be clear that the modulus of the spherical here is smaller than  $Y \approx 1000$  Pa, as obtain from actin comet deformation measurements. The main reason is that the filaments are not polarized against the compression force as is the case for actin comets with  $Y \approx 1000$  Pa.

Nevertheless, the comparison between theory and experiment gave a reasonable first result, namely, the stress against the cantilever is smaller than the total stress acting on the bead. One could extend the theoretical considerations to put the experimental results in a greater context. In order to achieve this, the following modeling efforts and questions have to be tackled:

1. The determination of a conversion factor to between  $F^{max}/A^{max}$  and the total actin on the bead surface stress  $\sigma^{max}$  would be a good starting point for further theoretical analysis. This would allow us to compare the elastic modulus of the actin gel with values obtained in the literature [19, 55, 59].
2. In doing so, the stress distribution should be modeled to understand which part of the internal elastic stress of the actin gel is acting on the cantilever.

Also, the force-velocity relationship gives further insight into actin based force generation. Here we can provide a qualitative comparison with force-velocity relationship obtained from the existing mathematical models.

a) The *Tethered Ratchet model* predicts a steep growth velocity decrease for increasing forces [41]. At increased forces more filament barbed ends bind to N-WASP probe surface, which reduces the number of pushing filaments. The thermal ratchet model also predicts that for increased forces the probability of a gap large enough to insert an actin monomer is decreased. Hence the growth velocity is reduced even for small forces (see Figure 3-5, p. 27)

b) *Mesosopic models* treat the actin gel as elastic material [5] and predict a much less steep decrease in growth velocity for increasing loads (see Figure 3-7, p. 33). The reason is that the gel generates strong antagonistic forces which almost compensate each other, even at no applied external force. Regulation of the antagonistic forces enables the gel to maintain its growth velocity as it grows against the external force.

In our measurement, the forces increase linearly with time, at least for the first 2/3 of a measurement run (Figure 5-19). Hence the force generation and growth velocity against the load in this regime is independent of the load. This

indicates, that the elastic model is a more appropriate description of the experiment than the Tethered Ratchet models.

There are also experimental issues that have to be understood or controlled in the future:

1. On a closer look the actin gels formed during gel expansion contain many flaws, i.e. regions with a reduced actin density. The question is whether the actin gels can be compared to the more homogeneous comet-like gels or gels that have been produced on a flat substrate [55, 57]. It might well be that due to the flaws the modulus of our gel is significantly reduced.
2. The composition of the gels varies quite strongly between the different measurements. The fluorescence intensity data Figure 5-20 shows that the 5  $\mu\text{m}$  and 21  $\mu\text{m}$  beads are denser in actin than the 10  $\mu\text{m}$  bead. This shows also in the tendency towards premature symmetry breaking which was observed more frequently for 5  $\mu\text{m}$  beads and 21  $\mu\text{m}$  beads. Gucht et al. [71] showed that increased degree of branching (due to larger density of filaments) may lead to faster symmetry breaking.
3. Even though we could show that the actin gels are under elastic tension, there is still indication that the diffusion of monomers and ARP2/3 in the section between the glass slide and the probe is a limiting factor in cantilever directed gel growth. The main indication is that although the force generation rate is load independent, the vertical gel thickness is 6-8 times smaller than the lateral gel thickness

### **5.2.2.10 Summary**

We have measured forces on of actin gels growing on a spherical colloidal probe attached to an AFM cantilever. The conditions were chosen such that the gel reaches a limiting thickness without breaking. Hence, the gel does not attain the comet geometry. In all phases of the actin gel extension the force generation rate is determined by the polymerization kinetics. This is proven by simultaneous fluorescence imaging revealing a linear gel growth in the regime of linear force production and cancellation of the gel growth in the force stalling regime. Therefore, we have strong indication that the force generation is always independent of the applied load. This is supported by the fact that the stall force is much smaller than actin gels are able to generate in comet geometry. The results strongly suggest, that the external force imposed by the cantilever does neither

limit the gel growth nor the generated forces. Rather, gel internal mechanical stresses control the force generation and the gel growth. When increasing the size of the probes an increase of the maximum gel thickness and maximum force is observed. Here the maximum gel thickness scales linearly with the bead radius. This is in agreement in the framework of the mesoscopic elastic models, and proves that the gel growth is stress limited. Two factors have an effect on the maximum generated force: 1) The spring constant (stiffness) of the actin gels, which determines the fractional amount of gel extension transduced into deflection of the cantilever. Generally, the spring constants increase for larger gels. The gel density, which was shown to vary for different probe types, also promotes the gel stiffness and the generated force. 2) A larger gel thickness increases the generated forces. The gel thickness is limited by the internal elastic stresses and therefore decreasing with the curvature of the probe. This is in agreement with the experimental results. These stresses exist also in curved biological systems like *Listeria* bacteria, or the cell membrane. The magnitude of the internal stresses cannot be directly measured by pure force assays as performed here. Future modeling efforts could yield the spatial stress distribution of actin gels in biologically relevant geometries. Our AFM based data could be used to quantify the stresses of such modeled stress distributions.

### 5.2.3 Effect of the Medium Composition

It is known, that the growth of a branched, dendritic actin network is associated with the formation of a filament nucleating complex that consists of g-actin and ARP2/3. The complex is then activated by the surface bound N-WASP for subsequent insertion of g-actin at the activated (actin|ARP2/3) complex. The ARP2/3 molecule induces branching, which leads to extension of a dendritic network. The general mechanism and the molecular components of the dendritic actin network growth have been discovered by in-vitro assays using merely purified proteins [12, 23]. Today the molecular details of this mechanism are subject to ongoing research. Besides clarifying the conformation of the biomolecules, quantitative assays are required to investigate the underlying self-assembly mechanism. In many studies the composition of *the actin medium is varied* and trajectories, velocity, gel morphology, fluorescence of specifically labeled components and other parameters are studied [12, 44, 48, 71]. Hence, the controlled change of the medium composition allows a better understanding of the macromolecular reactions that govern actin based motility and force generation [2].

Here we set out to study the impact of the medium composition on the force generation properties of the actin network. We perform the same kind of force measurement that employs the colloidal probe AFM approach as described in the previous section. The main findings from the previous section show that this technique is suitable to test gel composition effects. For example, the obtained forces are a function of the internal mechanical stresses, which also limit the growth of the actin gels. Gucht et al. [71] have shown that such growth limitations depend on the gel composition, e.g. the branching density or mesh size  $\xi$  of the network, see Eq. 3-17. The branching density for example, can be controlled by the concentration of ARP2/3 and gelsolin in the medium [44, 48]. Now, the variation of e.g. the branching density probably also affects the stiffness of the actin gel and the ability to transduce its self generated force against a load. Therefore the measurements under variation of the gel composition might give insight to the impact of the gel components on the ability of the gel to generate forces.

By variation of the medium composition we can control the following network properties: a) the degree of branching, which is the number of filament branches per actin monomer and b) the actin density, which represents the density of actin filaments in the network. For the sake of clarity we associate the

network properties with the respective medium component in the following list (explanations are given in section 3.2.2).

- *The degree of branching* depends primarily on the concentration of ARP2/3. Each ARP2/3 molecule in the network results in a branching point. Gelsolin is believed to promote the inclusion of ARP2/3 in the network, and should hence increase the degree of branching as well [44, 48].
- *The actin gel density* depends strongly on the ARP2/3 concentration. Increasing ARP2/3 leads to an actin gel density increase. Explanation: G-actin can either be included to existing filaments or form new filaments via the (actin|ARP2/3|N-WASP) complex. There is a competition for g-actin between both reactions. Only through the generation of new (actin|ARP2/3|N-WASP) complexes the gel density can be increased. Otherwise the existing filaments just grow longer, without affecting the gel density. Increasing ARP2/3 increases the probability for such a nucleating complex to form and hence densifies the gel.
- *The network mesh-size* decreases with both, the degree of branching and the actin gel density, because each filament contact point may serve as a (physical) cross-link. Therefore both parameters may control the mechanical tension in the spherical gel layer and the stiffness of the gel.

In the following the results of the force assays upon gel composition variation will be presented and discussed qualitatively.

***ARP2/3 increases the generation of force by promoting the stiffness of the actin gel:*** Here we vary the concentration of ARP2/3, where the upper limit of the concentration in the colloidal probe force measurements is 100 nM. With concentrations larger than 100 nM the gels increasingly break before their polymerization stops at the characteristic lateral gel thickness  $h_l^{max}$ . This is in qualitative accordance with Gucht et al. [71], where it was found that upon increasing ARP2/3 from 25-200 nM the gels start to break before the gel growth stops at  $h_l^{max}$ . We vary the ARP2/3 concentration between 15 and 100 nM, the complete medium composition is shown in Table 5-4. If a gel breaks prematurely, the respective measurement is not considered for further data analysis.

components	bead preparation		medium composition (proteins)					ARP2/3
	N-WASP	Beads PS-20 $\mu\text{m}$	F-actin	ADF	profilin	gelsolin	0.015 -	
concentration	0.5 $\mu\text{M}$	$1 \times 10^9 \mu\text{m}^2/\text{ml}$	7 $\mu\text{M}$	2.3 $\mu\text{M}$	2.4 $\mu\text{M}$	0.1 $\mu\text{M}$	0.1 $\mu\text{M}$	

**Table 5-4** Actin in-vitro medium composition for the experiments with varying ARP2/3 concentration (highlighted).

Typical force measurements with varying ARP2/3 content are shown in Figure 5-25. We find that all force curves first grow linearly before the stalling regime is reached. Hence, the shape of the force curve is comparable to those obtained in the previous section, where the ARP2/3 concentration,  $[\text{ARP2/3}]^5$ , was held constant at 100 nM. Again we find that the force generation stops at the same time that lateral gel growth stops. As discussed in the previous section, this behavior indicates that the force generation is limited by the polymerization of actin. When varying  $[\text{ARP2/3}]$  in the medium we make the following observations:

1. Increasing  $[\text{ARP2/3}]$  from 15 to 100 nM leads to an increase in the maximum force  $F^{max}$  by a factor of four. Figure 5-26 shows that  $F^{max}$  increases fairly linearly with  $[\text{ARP2/3}]$ .
2. The lateral gel thickness  $h_l^{max}$  is insensitive towards variations in  $[\text{ARP2/3}]$ . Also the unobstructed gel growth (lateral) is invariant to  $[\text{ARP2/3}]$ .
3. The gel density and hence the gel fluorescence intensity  $I$  increases with the concentration of ARP2/3:

$[\text{ARP2/3}][\text{nM}]$	15	30	100
$I[\text{a.u.}]$	2.7	3.5	4.3

**Table 5-5** Variation of  $I$  when changing  $[\text{ARP2/3}]$  from 15 to 100 nM

The actin gel thickness is invariant upon changes in  $[\text{ARP2/3}]$ . Therefore the change in  $F^{max}$  must be connected to the actin gel density or the degree of branching, but not to a change in gel thickness. In any case, we can explain the ARP2/3 related increase in  $F^{max}$  with stiffening of the gel as  $[\text{ARP2/3}]$  is raised. As a measure of the apparent gel stiffness we use the ratio  $F^{max}/h_l^{max}$ . This ratio relates the vertical gel extension  $h_v^{max} = F^{max}/k_c$ , with the lateral

<sup>5</sup> In the following concentrations of the components will be denoted in brackets, [component].

gel extension  $h_l^{max}$ , where  $k_c$  is the spring constant of the cantilever. The ratio  $F^{max}/h_l^{max}$  yields the fractional amount of force generated against the cantilever, as the gel grows by  $h_l^{max}$ . A stiffer gel transduces more of its unobstructed gel thickness increase, as measured by  $h_l^{max}$ , into deflection of the cantilever ( $C = h_l^{max}$ ). From the literature we indeed expect an increase in the apparent gel stiffness if we increase the amount of branches and the overall filament density in the gel. As explained above, both can be achieved by increasing [ARP2/3]. The increase in fluorescence intensity actually proves the increase of the gel density with [ARP2/3]. As shown in Figure 5-25, we indeed observe an increase in the gel stiffness  $F^{max}/h_l^{max}$  when raising [ARP2/3] from 15 to 100 nM. Therefore, ARP2/3 increases the force generation ability by stiffening the actin gel. This allows the gel to transduce more of its force-generating expansion to the load. As a result, we observe a larger deflection of the cantilever and an increase in  $F^{max}$ .

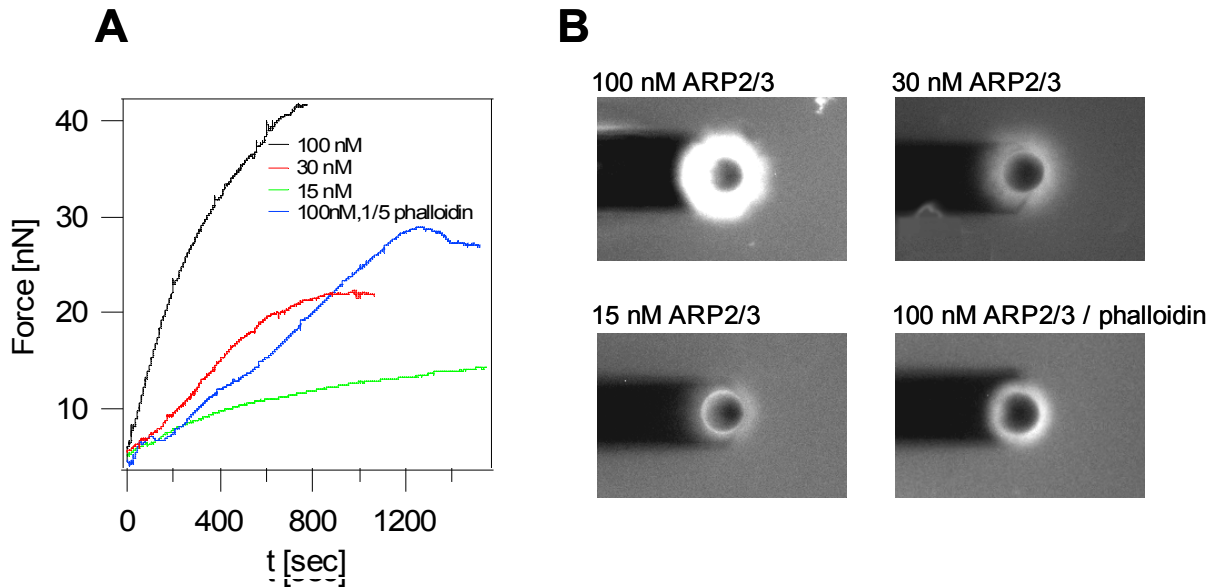


**Figure 5-25** (A) Typical force measurements on actin network of varying ARP2/3 concentration (15 nM yellow, 30 nM red and 100 nM black curves). The blue force curve depicts a measurement at 100 nM ARP2/3 with the addition of phalloidin in a molar ratio of 1 (phalloidin) : 5 (g-actin). The maximum force  $F^{max}$ , as well as the force generation rate increase with the concentration of ARP2/3. Note that the lateral gel thicknesses  $h_l^{max}$  in B) are similar when varying ARP2/3. Adding phalloidin decreases the force generation rate and  $h_l^{max}$ .



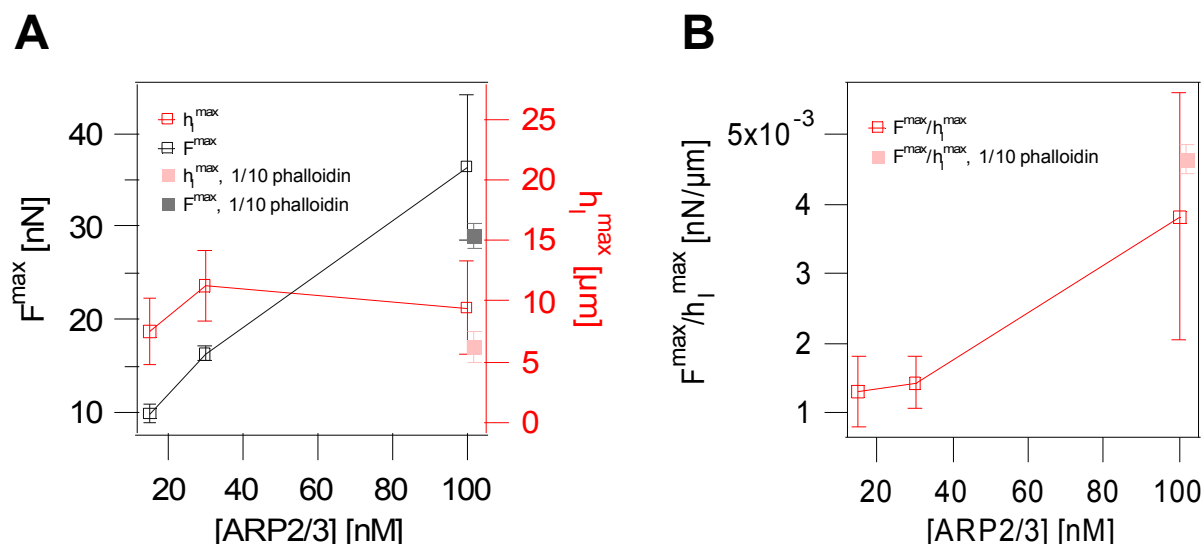


**Figure 5-26** A) The maximum forces  $F^{max}$  and maximum lateral gel thicknesses  $h_l^{max}$  generated by the actin gels with varying concentration of ARP2/3 (15, 30 and 100 nM). B) Plot of the apparent gel stiffness  $F^{max}/h_l^{max}$  against the ARP2/3 concentration, [ARP2/3].

**Phalloidin slows the gel growth but produces stiffer gels:** Phalloidin is a potent toxin that strongly binds to f-actin and hinders depolymerization [127]. Here, we set out to examine whether phalloidin affects the force generation ability of the actin gel. The interactions of phalloidin with actin filaments suggest that the mechanical properties of the entire gel are modified:

- Phalloidin binding decreases the flexibility of actin filaments [108].
- Phalloidin may increase the gel density due to the promotion of filament nucleation by increasing the creation rate of the (actin|ARP2/3|N-WASP) complex [128].
- Phalloidin stimulates the branch formation of ARP2/3 mediated gel growth [128].

A typical force curve and the fluorescence image of an actin gel polymerized in a medium containing phalloidin is shown in Figure 5-25. The ratio phalloidin to actin in the mixture is: 1 (phalloidin) : 5 (g-actin). A 1:1 ratio completely prevents actin gel growth. The comparison with the same composition but without phalloidin (at [ARP2/3]=100 nM), reveals that the generation rates of  $F$  and  $h_l$  are smaller when phalloidin is added to the medium. Figure 5-26A shows that  $F^{max}$  is decreased by 20% and  $h_l^{max}$  by 35 % when adding phalloidin.

The apparent stiffness of the actin gel  $F^{max}/h_l^{max}$  is increased by 17% due to the addition of phalloidin. The fluorescence intensity  $I$  of the actin gel decreases slightly when adding phalloidin: with phalloidin  $I = 3.8$ , without phalloidin  $I = 4.3$ .

The main impact of phalloidin is a reduced network growth which leads to smaller generated forces ( $F^{max}$ ). At the same time the gel becomes stiffer. As a result of the increased stiffness, the gels still produce relatively large forces although generating only small extensions ( $h_l^{max}$ ). As found by Mahaffy et al. [128], phalloidin promotes branching and enhances filament nucleation. Both, branches and a larger filament density could cause the stiffness increase. However, if the filament nucleation would be enhanced, the gel density and the fluorescence intensity would be elevated when adding phalloidin. We find the opposite behavior. Therefore one could attribute the stiffness increase due to increased branching. Alternatively, the stiffness increase could be caused by a reduced compliance of the actin filaments as found by Isambert et al. [108]. It would be possible to distinguish between both mechanisms by measuring the concentration of ARP2/3 induced branches in the gel. Such a measurement could be performed via quantitative fluorescence microscopy on labeled ARP2/3 in the actin network.

**Gelsolin reduces the gel density and the generated force:** We now proceed with the force measurements for a varying gelsolin concentration. The concentration of gelsolin ( $[gelsolin]$ ) is varied between 20 nM and 200 nM. The complete medium composition is shown in Table 5-6.

components	bead preparation		medium composition (proteins)				
	N-WASP	Beads PS-20 $\mu\text{m}$	f-actin	ADF	profilin	gelsolin	ARP2/3
concentration	0.5 $\mu\text{M}$	$1 \times 10^9 \mu\text{m}^2/\text{ml}$	7 $\mu\text{M}$	2.3 $\mu\text{M}$	2.4 $\mu\text{M}$	0.2-0.02 $\mu\text{M}$	0.1 $\mu\text{M}$

**Table 5-6** Actin in-vitro medium composition for the experiments with varying gelsolin concentration (highlighted).

Generally, varying  $[gelsolin]$  has a stronger effect on the generated forces than changing  $[ARP2/3]$ . Reducing  $[gelsolin]$  from 200 to 20 nM leads to a dramatic increase of  $F^{max}$  by about 120 nN. We also observe a remarkable decrease of  $h_l^{max}$  (20  $\mu\text{m}$ ) when changing  $[gelsolin]$  in the same way (Figure 5-27). The following list summarizes the main observations:

1.  $F^{max}$  increases by a factor of 6 when decreasing [gelsolin] from 20 to 200 nM (Figure 5-27). The increase is much steeper between 100 and 20 nM gelsolin (110 nN) as compared to decreases in [gelsolin] from 200 to 100 nM (15 nN).
2. As can be seen in Figure 5-28A  $h_l^{max}$  shows the same behavior as  $F^{max}$ : strong decrease between 20 and 100 nM gelsolin and moderate decreases between 100 and 200 nM gelsolin.
3. The apparent gel stiffness  $F^{max} / h_l^{max}$  decreases by a factor of 2 when raising [gelsolin] from 20 nM to 200 nM. Note, that the change in gel stiffness when varying [ARP2/3] is larger (factor 3.5), compare Figure 5-26 and Figure 5-28.
4. Gelsolin stimulates the (unobstructed) lateral gel growth rate  $v_l$  and decreases the gel fluorescence intensity  $I$ :

[gelsolin][nM]	20	100	200
$v_l$ [ $\mu\text{m}/\text{min}$ ]	0.4	0.9	1.7
$I$ [a.u.]	6.9	4.2	2.9

**Table 5-7** Variation of  $v_l$  and  $I$  when changing [gelsolin] from 20 to 200 nM

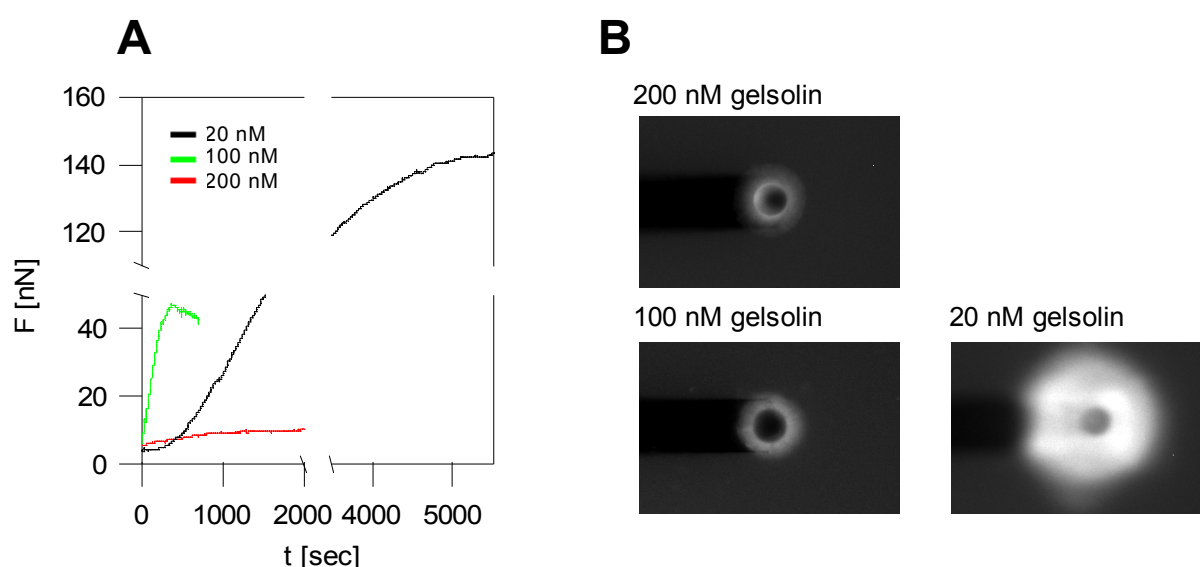


**Figure 5-27** A) Typical force measurements on actin network of varying gelsolin concentration. Increasing gelsolin generally leads to decrease of generated forces. For low gelsolin concentrations (20 nM, black curve)  $F^{max}$  is drastically in-

creased. B) Fluorescence micrographs of the gels representing the force curves in A. Note that for gelsolin concentrations as low as 20 nM the gels become very large and dense.

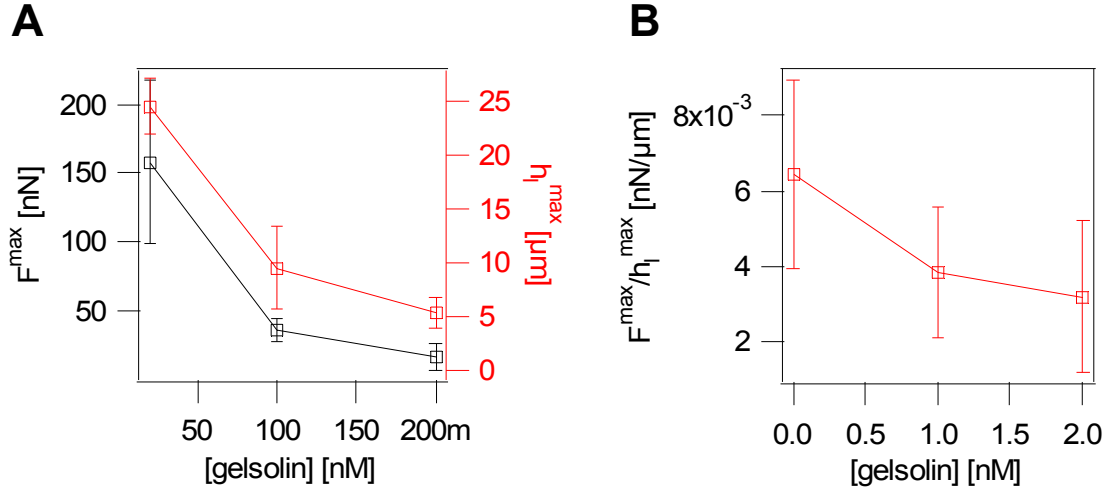


**Figure 5-28** The maximum forces  $F^{max}$  and maximum lateral gel thicknesses  $h_l^{max}$  generated by the actin gels with varying concentration of gelsolin (20, 100 and 200 nM). B) Plot of the apparent gel stiffness  $F^{max}/h_l^{max}$  against the gelsolin concentration.

The dramatic boost in  $F^{max}$  at [gelsolin] = 20 nM goes along with strong increase in  $h_l^{max}$ . Because of that, the apparent gel stiffnesses  $F^{max}/h_l^{max}$  do change as much as the large shift in  $F^{max}$  would suggest. The increase of  $F^{max}$  at lower [gelsolin] is due to two factors: a) larger gel extension; b) less compliant gels. The first explanation is in good agreement with the literature. It is well known that gelsolin directs the inclusion of actin monomers to the N-WASP coated surface by capping the filament barbed ends [43]. If the concentration of gelsolin in the medium is lower, filament capping and surface inclusion of g-actin is reduced. Akin et al. [44] found that for small concentrations of gelsolin (0-14 nM) the inclusion of g-actin to the actin network is faster or equally fast (at 14 nM) as the inclusion of g-actin to the bead surface. This may be due to the fact, that a large fraction of uncapped barbed ends remain uncapped in the network. These filaments are still able compete for g-actin addition with the filaments close to the bead surface. As a result, the inner mechanical stresses are reduced because less new actin layers are formed close to the bead surfaces. New actin layers push the previously grown gel layers outwards,

which create the mechanical stress in the first place. Consequently, lower gelsolin concentrations reduce the mechanical stresses; hence the gel growth and the force generation are less hindered.

The latter explanation b), argues that the increased  $F^{max}$  at lower [gelsolin] is due to an increase in gel density. We assume that denser gels are also stiffer. Stiffening of the actin gel, in turn, enhances the ability of the gel to transduce its self generated force against the cantilever, hence  $F^{max}$  increases. The fluorescence image and the intensity measurement show that the gels indeed become denser if we decrease [gelsolin]. This is in agreement with Akin et al. who finds that upon variation of gelsolin from 84 to 168 nM the fluorescence signal decreases by a factor of four [44]. However, it is also widely accepted that gelsolin promotes the degree of filament branching [44, 48]. This should have the opposite effect on the gel stiffness and  $F^{max}$ , namely an increase of both with [gelsolin]. Regarding the generation of force, the increase in degree of branching is overwhelmed by the decrease in actin density, so that the branching-effect on  $F^{max}$  is not observed.

**Summary:** Taken together, we could show that the gel composition does not only affect the polymerization kinetics as already studied by others [12, 44, 48, 127] but also the ability of the gel to generate forces against the load. The gel composition enhances the maximum generated force by two basic mechanisms: 1) *Increase of the gel stiffness.* This can be either due to more filament branching or by increasing the gel density. Both, branching and density, enhance the ability of the actin gel to transmit its generated force against the cantilever, rather than being deformed by the restoring force of the cantilever. 2) *Increase of the maximum gel thickness.* If the gel growth stops at the maximum gel thickness, the force generation stops as well. By decreasing the internal stresses, e.g. by fewer branching, the maximum gel thickness and force would be increased. Note, that both mechanisms 1 and 2 can be coupled: A stiffness increase (mechanism 1) may go along with a smaller mesh size. This in turn, increases the elastic gel tension and lowers the maximum gel thickness (mechanism 2). Therefore, enhancement of the force generation, be it due to mechanism 1 or 2, may be frustrated by their coupling.

By addition of phalloidin the generated forces are reduced, although the gel stiffness is increased. This can be explained by the very small maximum gel thickness. Seemingly, the coupling hypothesis applies here. An alternative explanation for the relatively small gel thickness is a decrease in the concentration

of polymerizable g-actin caused by phalloidin. This causes earlier cessation of the gel growth and smaller forces. In case of an ARP2/3 increase, the force enhancement is due to mechanism 1 because ARP2/3 reduces the mesh size by increasing the number of branches, which should lead to gel stiffening. The mechanism 2 does not play a role in case of ARP2/3, because the maximum lateral gel thickness is invariant to changes in the concentration of ARP2/3. Hence, a coupling of 1 and 2 is not observed in this case. When adding gelsolin we observe a decrease in gel density and a decrease of the gel thickness. Particularly at very low concentration the coupling of 1 and 2 seems to play no role. This is caused by an “abnormal” gel growth due to the lack of filament capping. In this situation actin is included in the network directly, rather than at the bead surface. As a result, the gels become larger and denser, which allows the gel to generate very large forces.

#### 5.2.4 Formin Based Actin Polymerization and Generation of Force

The force measurements presented so far were performed on dendritic actin gels that are mediated by the (actin|ARP2/3|N-WASP) complex. There exists another mode of actin polymerization where formins emerged as the key regulator [45, 46]. By contrast to the ARP2/3 based mechanism, during formin based actin polymerization the cells generate linear, unbranched bundles of actin. These are required during cytokinesis and to form filopodia in crawling cells [129]. The unbranched filaments generated by formin must have mechanical and rheological properties different as compared to the branched ARP2/3 filaments. Here we present the first force measurements on unbranched actin gels, generated via formin driven actin polymerization. Section 3.2.3 shows a more detailed description on the molecular formin working principle.

components	bead preparation		medium composition (proteins)		
	mDia	Beads PS-10 $\mu\text{m}$	F-actin	ADF	profilin
concentration	7 $\mu\text{M}$	$1 \times 10^9 \mu\text{m}^2/\text{ml}$	7 $\mu\text{M}$	2.6 $\mu\text{M}$	7 $\mu\text{M}$

**Table 5-8** Actin in-vitro medium composition for the force measurements with the unbranched actin gels.

For an in-vitro formin-based actin polymerization, the medium contains only two protein components, besides actin: ADF and profilin. Both regulate the rate of filament polymerization/depolymerization. ADF is necessary to maintain a

high concentration of g-actin by depolymerization of actin filaments that may form spontaneously in the medium. Profilin in combination with the formin greatly accelerates the growth of actin filaments [52]. As a f-actin nucleator we use a mammalian Diaphanous-related formin (mDia) which is deposited on the colloidal probes using the same protocol and beads as for the N-WASP deposition, see section 4.3. The exact composition of the medium is shown in Table 5-8, the same buffer composition is used as with the experiments on the branched actin networks. The force measurement procedure for the formin-based actin gels is very similar to the force measurements on the dendritic actin gels presented in the previous sections. The only difference being that after injection of the actin medium to the liquid cell, the force probe is approached exactly 1  $\mu\text{m}$  above the glass slide surface (no offset force is used to approach the surface).

The fluorescence micrographs in Figure 5-29B show that no sharp gel boundary is formed, as is the case for dendritic actin networks. The diffuse region of increased fluorescence intensity ( $I$ ) around the colloidal probe indicates the growing actin gel. Note, that the actin filaments do not bundle to form cables. This would be the case if methylcellulose was added to the medium [130] (data not shown). After a certain time of gel densification (0-1500 sec), the gel growth levels off. This behavior is reflected in the two force curves depicted in Figure 5-29A, where we observe an excellent matching between  $I$  and  $F$ . Here maximum forces are an order of magnitude smaller as compared to ARP2/3-based actin polymerization. This is most likely due to a much lower stiffness of the unbranched formin gels, which are less able to transduce their gel extension into deflection of the cantilever spring.

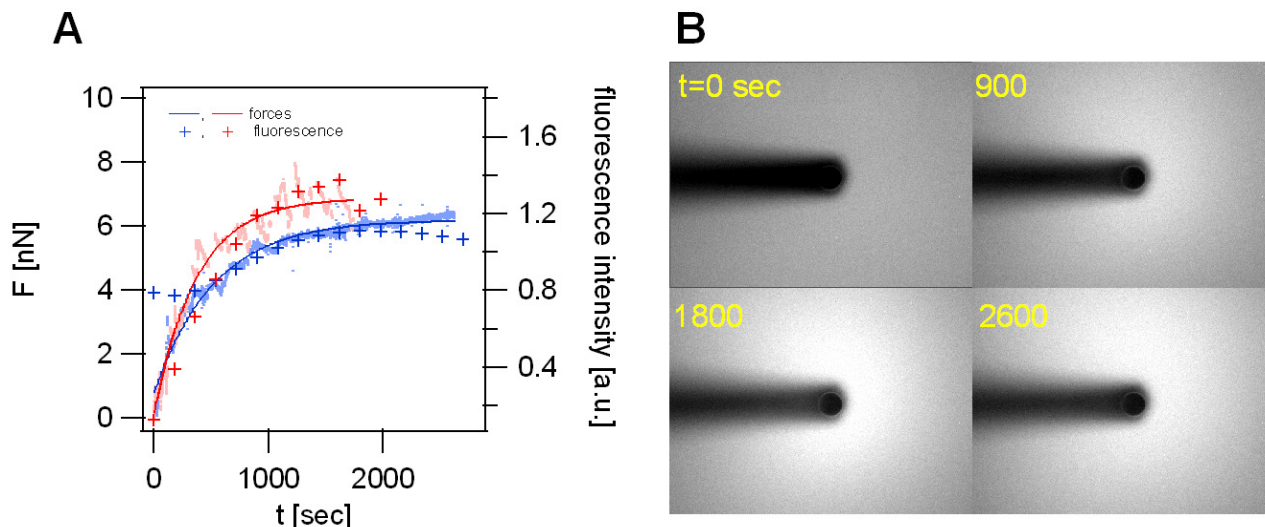


**Figure 5-29** A) Two force measurements (lines) on an unbranched, formin regulated actin gel. The markers represent the respective fluorescence intensity measurements performed at a fixed position in the fluorescence images shown in B. Both, the force- and fluorescence intensity curves match excellently. The fluorescence micrographs shown in B) reveal, that no sharp gel boundary is formed. The diffuse region with the increasing fluorescence intensity represents the gel and shows that the gel growth slows down after  $t \approx 1800$  sec.

The measurements on the formin gels deliver new perspectives for future force assays. One could test the effect of actin binding proteins or strong crosslinking (e.g. via biotin/streptavidin) on the generation of force. The results also show that we are able to measure forces on a relatively simple material consisting of unbranched and elongating filaments. This demonstrates, that the force generation of for example artificial supramolecular assemblies could be characterized using our colloidal probe AFM setup. As model materials one could for example use surface activated hydrogelators [131] or metallo-supramolecular [132] entities.



### ***5.3 Measuring Forces In-Vivo: Capsule Deformation in Cells***

***Background, motivation and general concept:*** This section presents a novel technique for intracellular force measurements. The aim is to detect real-time forces that emerge from cellular processes with capsule probes. These artificial capsules probes are introduced into crawling cells where they are subject to forces exerted by a network of various filaments and motor proteins that compress the capsule. As a measurement of the compression force we utilize the deformation of the capsules. One example where such intracellular forces are important is phagocytosis. Phagocytosis is the process by which cells "swallow" objects for digestion. The process involves large deformations of the cell membrane, driven by a complex machinery of proteins including actin and molecular motors [133]. The idea is to expose the capsule probes to phagocytes in order to activate phagocytosis, by which the capsules are engulfed into the phagocytes. In general, engulfment of material is facilitated by the actin-myosin contractile system. The contraction forces during engulfment and digestion can be measured by recoding the capsule deformation via microscopy. In order to obtain a quantitative measure of the force the following steps are executed: 1) Mechanical characterization of the capsules using colloidal probe AFM force measurements 2) Phagocyte assay in combination with confocal laser scanning microscopy to image the ingested capsules 3) Analysis of the capsule deformation and reconstruction of the compression forces acting to the capsule. The results are presented in the following.

***AFM characterization of polyelectrolyte capsules used as force sensors:*** The mechanical properties of polyelectrolyte multilayer capsules are studied using AFM-colloidal probe force measurements. Dubreuil et al. [134] characterized the elastic properties of polyelectrolyte microcapsules in a fundamental manner. It was found that the elastic response of the capsules is a function of the wall thickness and capsule size. This finding allows tailoring the capsules with regard to their mechanical properties. The capsules are selected such, to meet the mechanical, biological and instrumental requirements of the intracellular force assay. As suitable capsules we identified polyallylamine / polystyrene sulfonate (PAH/PSS) capsules comprising of 8 polyelectrolyte layers and with a diameter of 3  $\mu\text{m}$ . The capsules were manufactured by Surflay NanoTech GmbH, Berlin, Germany. The AFM-based mechanical characterization method is described thoroughly in section 3.7.2. In brief, we measure the applied force

vs. capsule deformation and obtain the stiffness and the buckling force of the capsules.

The force curves depicted in Figure 5-30 show two distinct deformation regimes. At small forces  $F < 110$  nN the capsules deform fairly linearly. From the linear regime we obtain a capsule stiffness of 0.11 nN/nm. For forces on the order of 154 nN, the capsules start to buckle which is indicated in the negative slope of the force curves. Both the buckling force and the capsule stiffness will be used to determine the intracellular forces that act on the capsules as they are engulfed into the phagocytes.

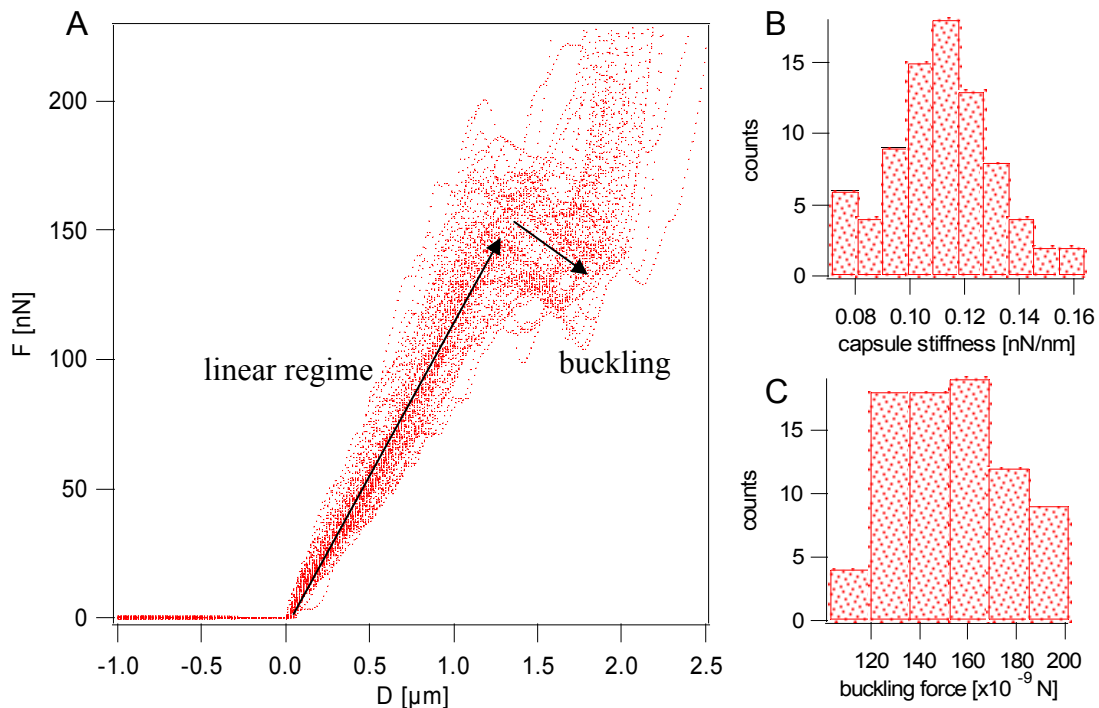


**Figure 5-30** A) Force ( $F$ ) vs. deformation ( $D$ ) curves of 80 single capsule measurements. Negative values for  $D$  denote the approach of the force probe to the capsule. For  $D=0$  the force probe is in contact with the capsule. For  $D < 1$   $\mu\text{m}$  and  $F < 110$  the capsules deform linearly. Capsule buckling is indicated by a negative slope that persists for  $\approx 0.5$   $\mu\text{m}$  B) The average capsule stiffness is  $0.11 \pm 0.02$  nN/nm, as determined by the slope of the force curves from  $D > 0$   $\mu\text{m}$  to  $D < 1.2$   $\mu\text{m}$ . C) The average buckling force is  $154 \pm 24$  nN.

**Deformation of the polyelectrolyte capsules during phagocytosis:** When offering the capsule probes to a medium containing phagocytes, the phagocytes first chase and then engulf the micro capsules. The forces emerging during ingestion lead to deformation of the capsules. The capsule deformation process is

shown in Figure 5-31. The images show that the capsules first attain an ellipsoid-like shape before they buckle in the last phase of cell digestion. Without accurate force field calculation of the capsules in the cells, we can so far only estimate the compression forces. Considering a buckling force of about 150 nN, we estimate that forces of at least  $5 \text{ nN}/\mu\text{m}^2$  are imposed on the capsules. Forces of comparable magnitude have been reported from traction force measurements on fibroblasts [135]. Compared to forces generated by mere actin polymerization ( $\approx 2 \text{ nN}/\mu\text{m}^2$ ) the actin-myosin mechanism obviously enhances the ability of cells to generate forces and to kill engulfed pathogens.

In future experiments specific motor proteins could be inhibited to deconstruct certain modes of cellular force generation. The resulting capsule deformations will be determined as described and the corresponding forces will be analyzed in more detail. This quantitative approach to force measurement in-vivo might contribute to a better understanding of the force generation in cells.

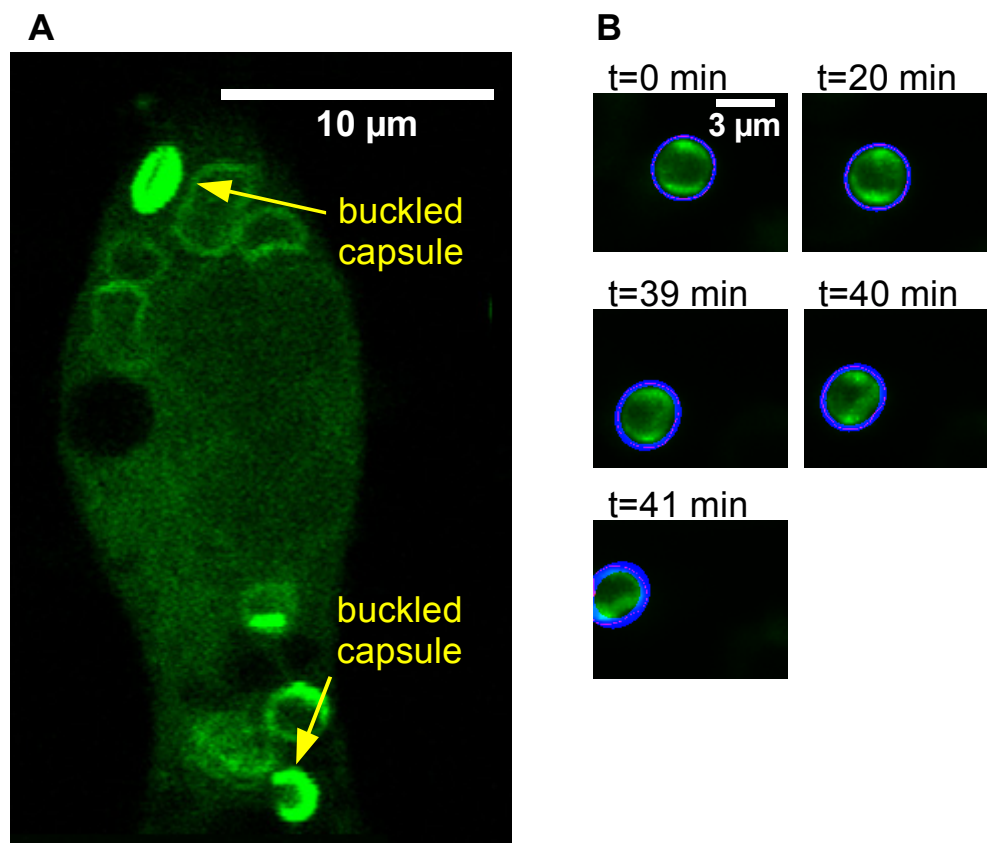


**Figure 5-31** A) Capsules often buckle after phagocyte ingestion. B) Confocal laser scanning microscopy of an engulfed capsule. The time-lapse images yield the capsule deformation by which the (time resolved) compression force acting on the capsules can be analyzed. Images by Vamsi Codali, Curtis Lab, School of Physics, Georgia Tech, Atlanta, GA

## 6 Conclusion

This thesis explores the force generation of actin gels and their famous propulsion mechanism leading to active motility on the cellular scale. In nature the generation of force and motility is regulated by actin binding proteins and the mesoscopic shape of the gel. Here we controlled and analyzed the effect of both, protein regulation and gel morphology by an in-vitro medium consisting of purified proteins and biomimetic beads with a nucleating surface. Under the controlled conditions offered by the medium we analyzed the motion of actin propelled colloids and the forces generated by the expanding actin gels using an AFM-based technique. Besides varying the in-vitro conditions and analyzing the effect on motility and force, we developed a new technique to measure intracellular forces in vivo. Hence, the work is structured in three parts: motility analysis, AFM force measurements (both in vitro) and force measurements in living cells.

***Results of the motility analysis on actin propelled beads:*** In this part we focused on the curvature of the trajectories generated by the actin propelled beads. The trajectory curvature was independent of the bead velocity, suggesting propulsive forces, rather than thermal fluctuation, introduce the trajectory curvature. The distribution of the curvature values was found to be non-Gaussian, indicating the force generating molecular processes are not completely stochastic. Such non-random processes are considered in the framework of the Tethered Ratchet model. Here, a positive feedback-loop exists between the magnitude of the generated force and the number of detached filaments. We simulated curved trajectories by unevenly distributing detached filaments on the bead surface and then computed the filament dynamics according to the Tethered Ratchet Model. If we included the positive feedback in the simulation, the experimental non Gaussian curvature distribution was reproduced, which supports the validity of the Tethered Ratchet model.

We found that a significant amount of beads showed a relatively high propensity for large curvatures and persistent circular motion. A possible reason could be the positive feedback mechanism or inhomogeneous surface coating of the filament recruiting factor (N-WASP). This introduces a torque on the bead leading to persistent circular motion. Such circular motion is the generic case in biology, as is confinement by obstacles such as cell organelles. Here we studied

the effect of confining geometries on the circular motion of actin propelled beads. We varied the confinement by choosing the width of linear channels in which the beads move. Generally, increasing confinement enhances the traveled distance, while larger trajectory curvatures lead to smaller traveled distances in the channels. One possible explanation are interactions with the channel wall allowing the particle to slide linearly along the channel. Such a sliding mode is favored by beads showing smaller trajectory curvatures.

*Perspectives:* The motility experiments could be used to study particle-wall-interaction in more detail to understand how the particles break away from obstacles. Also, the actively moving beads can be sorted according to their comet length, curvature or speed if the confining geometry is chosen appropriately. Our results also suggest that enhancing or deconstructing certain molecular reactions, e.g. capping or branching, affect the curvature of the trajectories. By performing appropriate assays under variation of the medium composition and analyzing the trajectories one can further study the molecular details of actin based motility.

***Force assays on actin gels:*** We performed direct force measurements on spherical actin gels attached to colloidal AFM probes. Simultaneously we recorded the gel shape and density via fluorescence microscopy. The expanding gels stall against a flexible cantilever after they generated forces on the order of  $0.15 \text{ N}/\mu\text{m}^2$ . Remarkably, as the force levels off not only gel growth against the cantilever stopped, but also the unopposed gel growth parallel to the cantilever. This means, the force is limited passively by cessation of the gel expansion, rather than active compression of the cantilever. The reason for the limitation of the gel expansion are internal mechanical stresses due to the spherical geometry of the gels. This is in line with the linear dependence of the gel thickness with the curvature of the probes. The measurements revealed that the internal stresses and not the load force were the limiting factor for actin polymerization and gel motility under these circumstances. By means of these AFM measurements, we detected a fraction of the internal gel stresses. Therefore, the collected data could be used to justify model calculations on the stress state of actin gels.

The AFM/fluorescence microscopy assay also revealed that the force generated against a load depends not only on the gel size, but also on its density and degree of branching. Both were controlled by adjusting the in vitro medium composition, e.g. by variation of the concentration of the auxiliary proteins ARP2/3 and gelsolin. ARP2/3 promotes branching and also increases the gel

density, leading to stiffening of the gel and larger forces. The capping protein gelsolin decreases the gel density. As a result, low gelsolin concentrations lead to very large forces, while the gel compliance decreased. Overall, the effect of the auxiliary proteins on the mechanical properties of actin gels can be well explained by their supramolecular reactions in the actin network. Adding phalloidin, a low molecular weight actin specific drug, enhances the stiffness of the actin gels by reducing the filament flexibility. We also prepared completely unbranched gels by the formin associated gel growth. Here the maximum forces were reduced by a factor of 10 because the gels were much more compliant as compared to branched, ARP2/3 containing networks.

*Perspectives:* The developed method allows for direct force measurements on mechanically weak unbranched gels. These “active” gels could be gradually cross-linked (even artificially) which should have a drastic effect on the elastic properties. Assessing the force generation of such networks would contribute to a more basic understanding of the mechanical properties of the cytoskeleton and active gels in general. Furthermore, finite element modeling of the compressed gels at the colloidal probe should reveal the complete stress distribution and elastic constants of the active gel.

***Force measurements in living cells:*** In vivo assays are essential because they provide means to validate results from in vitro measurements. Here we developed a method to measure the forces generated by phagocyte cells that engulf and kill pathogens in the organism. The idea is to measure the forces by recording the deformation of capsules engulfed in the phagocytes. We obtained forces on the order of  $5 \text{ nN}/\mu\text{m}^2$ , which is larger than the forces obtained by pure actin polymerization in vitro. The reason is that phagocytes make use of the actin-myosin contractile system rather than pure actin polymerization. Obviously, the actin-myosin system generates larger forces than lamellipodium-like actin polymerization. Using deformable capsules as force probes should provide insight into the real-time forces generated by a multitude of micro-biological entities. Even artificial systems could be studied with this method (e.g. responsive poly(NIPAM) microgels).

The force generation of actin gels and cell motility is based on molecular-scale processes. To gain an overall understanding of phenomena such as cell crawling, also the collective actions of the underlying molecular processes have to be understood. For instance, optical tweezer measurements revealed that the

force generated by single actin filaments is in the piconewton regime. Yet, the question remains how the action of individual filaments is concerted to yield forces up to several hundred nanonewtons as is the case for crawling cells. Therefore, it is crucial to study actin dynamics also on the mesoscopic scale and to adjust the measurement methods accordingly. The methods used and developed in this work are well suitable for such meso-scale investigations. For example, AFM and the capsule probe technique are capable of measuring the forces in the nanonewton regime. Their combination with optical methods yields the corresponding mesoscopic sample features. Hence, we quantified the actin-related meso-scale phenomena without directly analyzing the underlying molecular-scale processes. As a next step, modeling could be used in order to gain a multi-scale picture of actin dynamics, which is still largely unexplored. For example in this work, we contributed to such a generalized picture by describing the meso-scale motion of actin propelled colloids with the molecular-scale Tethered Ratchet model.

## 7 Zusammenfassung

Die vorliegende Arbeit beschäftigt sich mit der Krafterzeugung von Aktin Gelen und der daraus resultierenden aktiven Bewegung von kolloidalen Objekten. Die hier zugrundeliegende Art der Krafterzeugung ist von fundamentaler Bedeutung in der Natur, da sie Grundlage der aktiven Migration von eukaryontischen Zellen ist. In der Zelle wird die Krafterzeugung durch eine Vielzahl von aktinbindenden Proteinen und durch die Morphologie des Aktinnetzwerks reguliert. Im Rahmen dieser Arbeit wurden beide Effekte, sowohl Protein-regulierung als auch Gelmorphologie, in Bezug auf die Krafterzeugung und Bewegungsfähigkeit von Aktin Gelen in einem in-vitro Medium untersucht. Dieses Medium erlaubt Wachstum von Aktinnetzwerken auf aktivierten Oberflächen, wodurch z.B. AFM-Kraftmessungen an expandierenden Gelen ermöglicht wurden. Neben der in-vitro Analyse von Aktin-assoziierten Kräften und Bewegungen haben wir eine neue Technik zur Bestimmung von intrazellulären Kräften entwickelt, welche in lebenden Zellen vorgenommen werden kann. Entsprechend ergibt sich eine dreiteilige Gliederung der Arbeit: Bewegungsanalyse von Aktin-angetriebenen Partikeln, AFM-Kraftmessungen an Aktin Gelen (beides in-vitro) und Kraftmessungen in lebendigen Zellen.

***Bewegungsanalyse vom Aktin-getriebenen Partikeln:*** In diesem Teil untersuchten wir das Verhalten von Partikeln, welche von einem schweifartigen Aktinnetzwerk angetrieben wurden und konzentrierten uns auf die Krümmung der Partikeltrajektorien. Die Krümmung der Trajektorien war unabhängig von der Partikelgeschwindigkeit was darauf hindeutet, dass die Triebkraft des Aktin Gelen, und nicht etwa thermische Fluktuationen für die Trajektorienkrümmung verantwortlich sind. Den Krümmungen lag keine Normalverteilung zugrunde, was bedeutet, dass die krafterzeugenden molekularen Prozesse im Gel nicht regellos ablaufen. Solche nicht-stochastischen Prozesse werden im „Tethered Ratchet“ Modell berücksichtigt. Darin wird eine positive Rückkopplung zwischen generierter Kraft und Anzahl ungebundener, also wachsender, Aktinfilamenten beschrieben. In Simulationen zeigten sich bei Einbeziehung dieser Rückkopplung ebenfalls nicht normalverteilte Krümmungen und eine generelle Übereinstimmung mit den experimentell beobachteten Trajektorien. Diese Studie unterstützt daher die Gültigkeit des „Tethered Ratchet“ Modells und zeigt, dass sich die mesoskopische Bewegung des Aktinnetzwerks durch Prozesse auf molekularer Ebene beschreiben lässt.



Ein großer Teil der Partikel vollzog kreisförmige Bewegungen mit gleich bleibendem Krümmungsradius. Dies könnte durch den besagten Rückkopplungsmechanismus, oder durch inhomogene Beschichtung der katalysierenden Partikeloberfläche geschuldet sein. Beides erzeugt ein Drehmoment am Partikel, welches zu der persistenten Kreisbewegung führt. Kreisförmigkeit ist nicht ungewöhnlich für Bewegungen von z.B. Pathogenen auf der Zellebene, wobei hier auch Hindernisse durch z.B. Zellorganellen die Bewegungsrichtung zusätzlich beeinflussen können. Wir untersuchten nun die Partikeltrajektorien mit zusätzlichen Hindernissen, dargestellt durch lineare Kanalwände zwischen denen sich die Partikel bewegten. Für engere Kanäle beobachteten wir eine Steigerung der zurückgelegten Partikelstrecke, wobei kleinere Krümmungsradien den umgekehrten Effekt zeigten. Diese Befunde lassen sich durch das Gleiten der Partikel an den linearen Kanalwänden erklären. Diese Gleitbewegung wird von Partikeln mit großen Krümmungsradien bevorzugt.

*Ausblick:* Die Partikeltrajektorien in eingeschränkten Geometrien zeigen wie mikroskopische „Kreisschwimmer“ mit Hindernissen interagieren und wie sie sich von ihnen losreißen können. Bei optimierter Hindernisgeometrie sollten die Partikel in Abhängigkeit ihres Krümmungsradius oder Schweiflänge unterschiedliche Distanzen zurücklegen und sich dementsprechend separieren lassen. Weiterhin könnte man die Zusammensetzung des in-vitro Mediums verändern und dessen Einfluss auf die Partikeltrajektorien untersuchen. Somit ließen sich weitere Einblicke in die molekularen Prozesse im Aktinnetzwerk erlangen.

***Kraftmessungen an expandierenden Aktingelen:*** In diesem Abschnitt untersuchten wir die Kraftentwicklung von Aktingelen, die hier auf kolloidalen AFM-Sonden expandieren. Simultan zur Kraftmessung wurde die Form und Dichte der Gele mittels Fluoreszenzmikroskopie aufgezeichnet. Das Gelwachstum und die damit Kraftentwicklung gegen die AFM-Blattfeder brachen ab, nachdem Kräfte einer Größenordnung von  $0.15 \text{ N}/\mu\text{m}^2$  erzeugt worden waren. Erstaunlicherweise stoppte gleichzeitig auch das (ungehinderte) Gelwachstum parallel zur Blattfeder. Daher ist hier die Kraftentwicklung eher durch Abbruch des gesamten Gelwachstums begrenzt, als durch aktive Kompression der Blattfeder. Der Grund für die Wachstumslimitierung sind mechanische Spannungen, welche durch die kugelförmige Gelgeometrie entstehen. Dies stimmt auch mit der linearen Abhängigkeit von den maximalen Gel-dicken mit der Krümmung der AFM-Sonden überein, auf denen die Gele wach-

sen. Die Messungen konnten also zeigen, dass hier die interne Gelspannung und nicht die externe Belastung der limitierende Faktor für das Gelwachstum ist. Die AFM Messungen erlauben eine Abschätzung der Gelspannung, was für die Modellierung von Spannungszuständen in Aktin Gelen hilfreich sein könnte.

Die kraft- und fluoreszenzmikroskopischen Messungen zeigten außerdem, dass die Fähigkeit Kräfte zu entwickeln nicht nur von der Größe, sondern auch von der Zusammensetzung d.h. von Verzweigungsgrad und Dichte der Gele abhängt. Beides, Dichte und Verzweigungsgrad, wurden über die Zusammensetzung des in-vitro Mediums kontrolliert, z.B. durch Veränderung der Konzentration von ARP2/3 und Gelsolin. ARP2/3 dient zur Verzweigung von Aktinfilamenten und erhöht gleichzeitig die Dichte der Filamente, was die erzeugten Kräfte und die Steifigkeit der Gele erhöhte. Gelsolin wiederum bindet an Filamente und verhindert deren Wachstum. Es zeigte sich, dass erhöhte Konzentrationen von Gelsolin zu kleineren Kräften und geringer Gelsteifigkeit führen. Wir konnten hier den Einfluss der untersuchten aktinbindenden Proteine auf die Kraftentwicklung anhand deren supramolekularen Reaktionen im Gel qualitativ erklären. Vollkommen unverzweigte Aktin Gele wurden mittels Formin-gesteuerter Aktinpolymerisation erzeugt. Diese Gele sind deutlich weicher, daher waren die erzeugten Kräfte eine Größenordnung kleiner im Vergleich zu den verzweigten ARP2/3-assoziierten Gelen.

*Ausblick:* Die hier entwickelte kraftmikroskopische Methode erlaubte direkte Kraftmessungen auch an sehr weichen, unverzweigten Aktin Gelen. Diese aktiven Gele lassen sich kontrolliert vernetzen, z.B. über Biotin/Streptavidin Wechselwirkungen. Die daraus folgende Veränderung der mechanischen Eigenschaften und der Kraftentwicklung lassen Rückschlüsse auf vernetzte Systeme wie dem Zytoskelett zu. Generell lässt sich mit dieser Methode auch der Einfluss weiterer aktinbindender Proteine auf die Kraftentwicklung analysieren. Es bietet sich weiterhin an, finite-Elemente Modellierung an den hier untersuchten Gelstrukturen durchzuführen um den Stresszustand sowie elastische Konstanten der Gele zu ermitteln.

***Kraftmessungen in lebenden Zellen:*** In-vivo Untersuchungen sind generell von Bedeutung, da sie sich eignen, um die Gültigkeit von in-vitro Messungen in lebenden Organismen zu überprüfen. In diesem Teil der Arbeit wurden Kräfte in Phagozyten gemessen, welche in der Lage sind, pathogene Keime zu umschlingen und abzutöten. Als Kraftsensoren boten wir den Phagozyten künstliche Mikrokapseln mit maßgeschneiderten mechanischen Eigenschaften

an. Diese wurden dann von den Phagozyten umschlungen und deformiert. Anhand von Deformationsmessungen konnten wir Rückschlüsse auf die Kräfte ziehen, die gegen die Kapseln gerichtet wurden. Die Kräfte lagen hier in der Größenordnung von  $5 \text{ nN}/\mu\text{m}^2$ . Im Vergleich dazu liefert die reine Aktinpolymerisation Kräfte von nur etwa  $2 \text{ nN}/\mu\text{m}^2$ . In Phagozyten entsteht die Kompressionskraft durch das Aktin-Myosin Motorsystem welches offenkundig größere Kräfte erzeugt als die Aktinpolymerisation im Lamellipodium. Auch diese neue Methode zur Bestimmung von intrazellularen Kräften ist universell einsetzbar und könnte neue Erkenntnisse über die Kräfte in anderen mikrobiologischen Organismen liefern. Darüber hinaus sind Kraftmessungen in künstlichen, responsiven Gelen möglich (z.B. in poly(NIPAM) Mikrogelen).

Die Generierung von Kräften in Aktingelen und die aktive Zellmigration basiert auf molekularen Prozessen. Um mit Kenntnis dieser Prozesse z.B. die Kriechbewegung von Zellen vollständig zu beschreiben, muss jedoch auch die Selbstordnung und das Zusammenwirken der molekularen Prozesse verstanden werden. Als Beispiel: Einzelne Aktinfilamente generieren Kräfte von nur wenigen Piconewton. Es ist jedoch nicht im Detail klar, wie die Gesamtheit von Filamenten im Zytoskelett gesteuert wird, damit Kräfte von mehreren hundert Nanonewton zu erzeugt werden. Entscheidend ist daher, die Dynamik von Aktinnetzwerken auch auf mesoskopischer Ebene zu analysieren, und dahingehende Meßmethoden zu entwickeln. Die in dieser Arbeit entwickelten Methoden eignen sich für entsprechende Untersuchungen auf der Mesoebene. Die Deformationsmessungen an Mikrokapseln und die AFM-basierte Methode wurden optimiert, um Kräfte im Nanonewton-Bereich zu messen. Die Kombination mit optischen Methoden erlaubte es, simultan die mesoskopische Probenmorphologie zu analysieren. Wir haben also Kräfte und Bewegungen von Aktingelen auf der Mesoebene quantifiziert, ohne direkten Einblick in Prozesse auf molekularer Ebene zu erhalten. Mittels Modellierung könnte nun ein skalenübergreifender Einblick in die Dynamik im Aktingel erlangt werden. Zum Beispiel gelang es hier, die mesoskopische Krümmung der Partikeltrajektorien anhand des „Tethered Ratchet“ Modells auf molekularer Ebene erklären.

## 8 Appendix

### 8.1 Parameters and Abbreviations

Many kinetic parameters of ARP2/3 mediated actin network growth have been determined experimentally. Table 8-1 lists the kinetic parameters used for calculations in section 5.1.1 as well as all other parameter symbols used in this work.

Parameter	Definition	Value [Units]
	<i>Actin Polymerization</i>	
$k_n$	Nucleation/branching rate	10 [#s]
$k_{na}$	Nucleation/branching rate per unit area	0.8 [s <sup>-1</sup> /μm <sup>-2</sup> ]
$k_c$	Capping rate	0.15 [s <sup>-1</sup> ]
$k_{d,0}$	Effective filament dissociation rate	0.1 [s <sup>-1</sup> ]
$[A_g]$	Effective actin monomer concentration	1 μM
$V_p$	Polymerization velocity	0.500[nm/s]
$V_{dep}$	Depolymerization velocity	2.2[nm/s]
$V_{max}$	Load free polymerization velocity	
$l$	Length increment of filament growth	2.2[nm]
$\delta$	Effective monomer size	
$k_B T$	Thermal Energy	2.2[pN·nm]
$x_b$	Effective length of the attachment bond	0.4 [nm]
$f_b$	Effective strength of the attachment bond	10 [pN]
$k_a$	Spring constant of the attachment link and filament	3 [pN/nm]
$k_f$	Spring constant of an actin filament	0.3 [pN/nm]
$a$	Number of attached filaments	[#]
$w$	Number of free, working filaments	[#]
$t$	Time	[sec],[min]
$f_w$	Single filament polymerization ratchet Force	[pN]
$f_a$	Attachment force per filament	6 [pN]

## 8. Appendix

$f_L$	Load Force	[pN]
$V$	Velocity of the load (bead)	[nm/s]
$k_+$	Barbed end polymerization rate	$10 [s^{-1} \mu M^{-1}]$
$k_-$	Barbed end depolymerization rate	$1 [s^{-1} \mu M^{-1}]$
$\kappa$	Curvature	$[\mu m^{-1}]$
$d_{e2e}$	End-to-end distance	$[\mu m]$
<b><i>AFM Experiment</i></b>		
$F$	Force measured by AFM	[N]
$I$	Area normalized fluorescence intensity	
$F^{max}$	Maximum force generated during gel extension	[N]
$F'_{max}$	Fluorescence intensity normalized maximum force	[N]
$C$	Cantilever deflection	[nm]
$k_c$	Spring constant of the cantilever	
$h$	Actin gel thickness	$[\mu m]$
$h_v$	Actin gel thickness vertical to compression	$[\mu m]$
$h_l$	Actin gel thickness lateral to compression	$[\mu m]$
$\delta = h_l - h_v$	Actin gel deflection	$[\mu m]$
$k_g$	Apparent actin gel stiffness	[N/m]

**Table 8-1** The parameters used in this work.

The following table lists important abbreviations and technical terms.

<b>Abbreviation/Term</b>	<b>Definition</b>
	<b><i>Instruments</i></b>
AFM	Atomic Force Microscopy
CLSM	Confocal Laser Scanning Microscopy
	<b><i>Proteins</i></b>
ADF	Actin Depolymerization Factor
ARP2/3	Actin Related Protein, branches/nucleates filaments
f-actin	Filamentous actin
formin	A nucleation promotion factor (NPF)
g-Actin	Globular actin

gelsolin	Barbed end capping protein
mdia	Mammalian Diaphanous-related formin
NPF	Nucleation promotion factor (WASP, formins)
N-WASP	Wiscott-Aldrich Syndrome Protein, an NPF
Profilin	Actin polymerization promoter

## 8.2 Force measurement on actin comets at the colloidal probe

In a first force assay we aimed to determine the forces generated by the actin comet growing at the colloidal probe. Here the actin comet is directed against a substrate, while it extends. Upon extension the comet generates forces which lead to deflection of the cantilever. This deflection generates a restoring force, which can be measured with the AFM. A similar but more general AFM experiment is explained in detail in paragraph 3.7.2. This type of setup is very similar to the micropipette experiment performed by Marcy et al. [55] which is described in section 3.3. Our AFM based setup should be more sensitive and also have a larger range of accessible forces as compared to the micropipette approach. Another fundamental difference to the work Marcy is that the actin comet remains free to undergo shearing motion (perpendicular to the direction of growth) as it is compressed with the cantilever. Marcy fixed the comet between the activated bead and the outlet of a micropipette, trapping the comet at both ends, so that shearing motion is hindered. Similar to the micropipette experiments, NPF-coated silica beads attached to a flexible cantilever form actin comets in the actin medium (see Table 4-1). Break of the spherical actin shell and comet formation is here observed at times larger than 5 min in for beads of 5  $\mu\text{m}$  diameter using the following protein composition: 7  $\mu\text{M}$  Actin, 2.25  $\mu\text{M}$  ADF, 2.4  $\mu\text{M}$  profilin, 0.1  $\mu\text{M}$  ARP2/3, 0.1  $\mu\text{M}$  gelsolin. Colloidal probes of a larger diameter were used to measure the forces without breaking the gel symmetry, and therefore forming no comets, see sections 5.2.2 and 5.2.3. In the following however, only force measurements of gels in comet geometry will be discussed.

The comet always grows perpendicular from the underside of the cantilever as shown for example in the lower right image of Table 4-1 and Figure 8-1A. According to [71] the position of the comet on the bead can be predetermined

by defects in the gel. In our case such a defect is introduced by the attachment of the bead to the cantilever. Due to the bead attachment, the gel thickness vanishes at the attachment point, which creates a gel defect where the regular spherical symmetry of the gel layer is broken. As a result of this preset broken symmetry, the nascent uncompressed actin comets are always growing perpendicular to the cantilever.

For the interpretation of the data collected during force measurements it would be advantageous to maintain the actin comet in perpendicular position. The question is, whether the perpendicular orientation of the comet remains stable under its self generated compression. To investigate the position stability of the comet we apply a constant force against the comet in the range of 2-30 nN, see Figure 8-1. With beads of 5  $\mu\text{m}$  in radius the pressures on the comet are roughly 0.05-0.75  $\text{nN}/\mu\text{m}^2$ . For each applied constant force a new experiment with a “fresh” probe is made. From this it follows that the comet length is not the same for the different experiments under variation of the applied pressures. Therefore the compliance of the comet varies for the different measurements, which makes quantitative comparisons difficult. However, the observed main trends are persistent through the different experiments. All experiments show that the actin comet undergoes sliding even at extremely small compressions on the order of 50  $\text{pN}/\mu\text{m}^2$ , as shown in Figure 8-1A. Decreased compression merely leads to slower sliding of the comet as represented in the slower height change (Figure 8-1B) for smaller compression. Consequently, measurements of the gel extension force generated by the actin network will be very difficult to interpret as sliding of the comet also occurs by the self generated force of the actin network (data not shown). As a conclusion from this study, we do not perform the quantitative force measurements on comets but on spherical actin gels which are not prone to sliding, see paragraph 5.2.2.

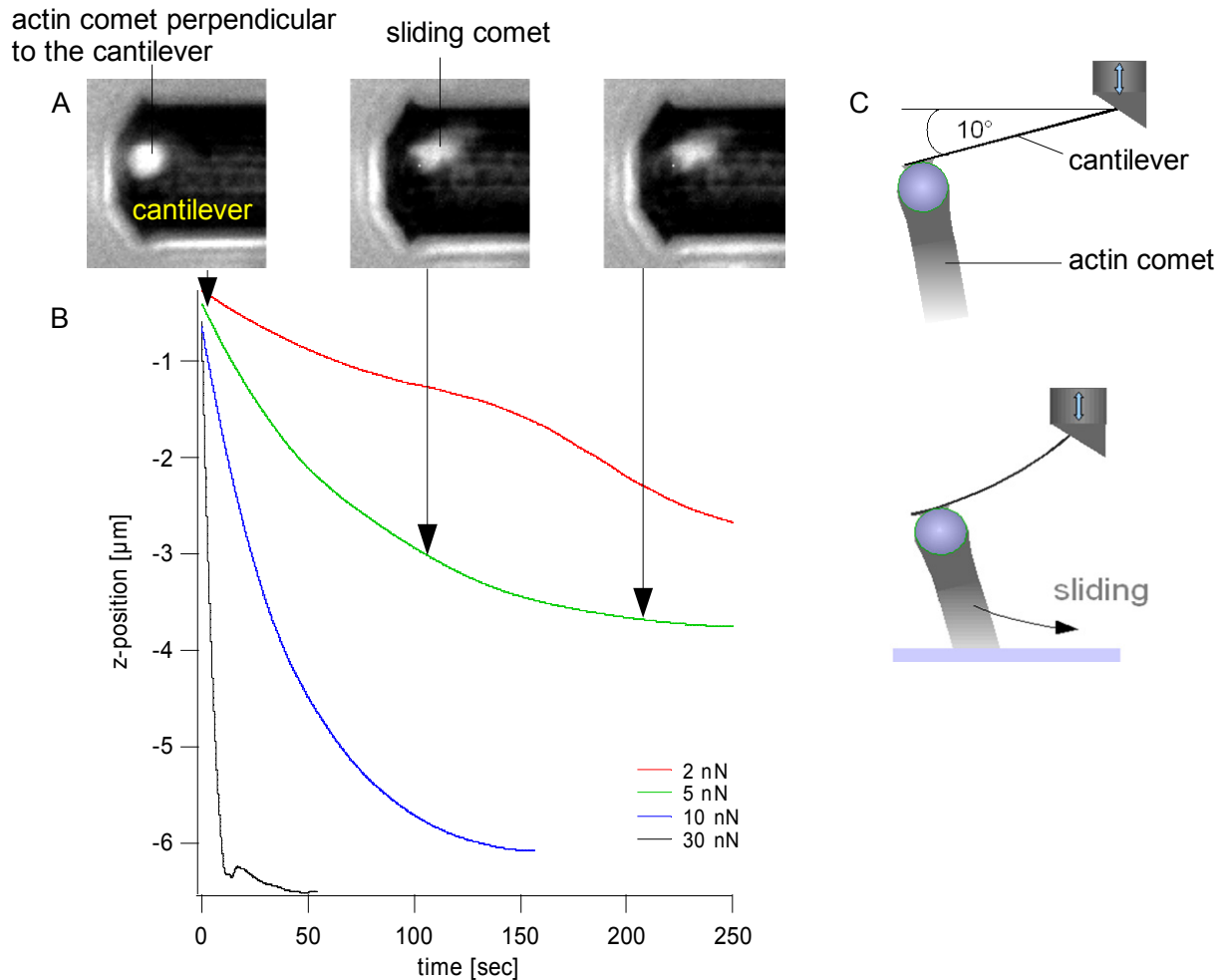


**Figure 8-1** Actin comet undergoes sliding motion under compression imposed by the AFM cantilever. A) Fluorescence microscopy time lapse images taken at constant applied force of 5 nN. B) To maintain a constant applied force by the cantilever position of the z-piezo is changed by the AFM-feedback controls. In other words, the z-piezo movement compensates for the sliding motion of the actin comet. The figure shows z-position data collected for different applied forces. Increased compressions lead to faster comet sliding and faster response of the z-piezo. C) The actin comet is always tilted by  $10^\circ$ , so that even without compression the cantilever is not perfectly perpendicular to the substrate (at  $90^\circ$ ) but at least at  $80^\circ$  with respect to the substrate. Sliding therefore always occurs towards the center of the cantilever.

After retraction of the cantilever from the surface and release of the compressing force on the actin comet, the comet returns to the perpendicular orientation. From the microscopic or molecular point of view the side-sliding motion of the comet could be induced due to two mechanisms:



- a) Under compression the actin filaments are pushed against the surface. Then, according to the Tethered Ratchet model, an increased fraction of minus filament ends bind to the surface bound N-WASP (see Eq. 3-5 in section 3.4.2). These N-WASP sites are then not available for nucleation of new filaments. This essentially slows the polymerization at the sites of increased filament bonding, which occurs at the sites of highest compression. The sites of highest compression always faces the substrate, therefore actin polymerization becomes more favorable at the sides of the colloidal probe. This results in polymerization of a comet *not* perpendicular to the substrate or cantilever. So instead of moving the network, polymerization / depolymerization translocates the comet, which might appear as sliding motion. This process is limited by the polymerization velocity of the gel.
- b) The preset tilt of  $10^\circ$  of the actin comet and the following compression against the substrate results in a torque that drags the actin comet from its perpendicular orientation to a parallel orientation with respect to the cantilever. According to the sketch in Figure 8-1 the torque would shift the comet from left to right which requires breaking of N-WASP links on the left side, and buildup of new links on the right side of the comet. Again force dependent breaking of filament barbed end links with surface bound N-WASP might explain breaking on the left, while the surface-directed force in the right enhances the attachment of the comet. This process is not limited by polymerization speed of the gel. Here the network is truly translocated under the strain due to the applied force.

The main difference between a) and b) is the timescale of comet orientation change. Mechanism a) requires polymerization of a new network, which is slower than the true sliding of the network along the bead surface in case of b). The experiment performed does not allow deciding which could be the prevailing mechanism. However, it is clear that for smaller compression mechanism a) becomes increasingly important. Furthermore, a) could also explain why even very small compressions of only  $50 \text{ pN}/\mu\text{m}^2$  induce a shift in comet orientation. Here the reason is that alteration of the polymerization kinetics requires small forces. The apparent sliding is due to polymerization of a new, side-wise oriented network.

### 8.3 Working up g-Actin

1. Transformation of G-actin to F-actin
  - for 1 ml of an old actin solution give 25  $\mu$ l KCl 4M and 1  $\mu$ l MgCl<sub>2</sub> 1M
  - wait for complete F-actin polymerization, leave it room temperature for 1 hour
2. Centrifuge, wash and redisperse in G-buffer
  - centrifuge 1 ml of the F-actin solution at 400 000g for, 40 min, 20°C.
  - prepare 2 l of G-buffer, see Table 4-1
  - remove the supernatant, try to keep the pellet at the centrifuge tube wall
  - wash the pellet with G-buffer (2x 2 ml)
  - redisperse and homogenize the actin pellet with a 2 ml potter mortar
  - let the F-actin depolymerize for 1 hour on ice
3. Dialysis
  - dialyze the G-actin solution in 500 ml G-Buffer at 4°C, using a pore size of <40 kDa
  - change the buffer three times after at least 6 hours
4. Determination of the G-actin concentration
  - measure the UV-Vis spectra of the actin solution in a 1 cm cuvette
  - read the absorbance ( $abs_{290nm}$ ) at 290 nm and calculate the concentration according to:

$$c_{actin} = \frac{abs_{290nm}}{\epsilon \cdot x \cdot M}$$

$$\epsilon=0,617 \text{ mg}^{-1} \text{ ml cm}^{-1}, x=1 \text{ cm}, M=42000 \text{ g/mol},$$

### 8.4 Grey Value Normalization in Image Stacks Using an Internal Reference

```
macro "normalize slice"
//this macro allows grey value normalization of single images
//or image stacks. performing the background normalization:
// a) select region(s) in the image or stack that represent the
// background grey value (BGV) you want to normalize the rest of the image with
//(b) run the script, it will calculate the background grey value
//for each slide, and normalize the whole image, pixel by pixel as
// pixelvalue/BGV for each slide separately
```

## 8. Appendix

---

```
run("Clear Results"); //creates an empty data table
run("32-bit"); //transforms the image matrix from integer to real numbers
getSelectionBounds(x,y,width,height);
//measures the ROI (background) area

w = getWidth();
h = getHeight();

//the loop sets the slices (image frames) forward
//and measures the average ROI grey value
for (n=1; n<=nSlices; n++) {
    setSlice(n);
    run("Measure");
    mean=getResult("Mean", n-1);
    //loop moves trough each pixel and normalizes it
    for (y=0; y<h; y++) {
        for (x=0; x<w; x++){
            norm=getPixel(x,y)/mean;
            setPixel(x, y, norm);
        }
    }
}
setSlice(1); //jumps back to the first slice
makeRectangle(0, 0, w, h);
//selects the whole stack for contrast enhancement
run("Enhance Contrast", "saturated=0.1");
//as the grey value was changes during normalization
```

### 8.5 Automated Linear Fits for AFM Force-Distance Curves

```
FUNCTION forcefit(startfit, forcelen) //Main procedure that calls subprocedures "calc-
def()", "baseline()" //and "forceslope"

variable startfit, forcelen
calcdef() //"calcdef()" transforms deformation into distance data, re-
quires
baseline() //that the spring constant is stored as a global variable in the
root //folder
forceslope(startfit,forcelen) //"baseline()", fits the baseline of a forcecurve
killwaves/z errorwave, vDefl, error //"forceslope()" creates a linear force curve fit, pa-
rameter "startfit"
end //determines where the fit starts, startfit(1) means fitting from
the //maximum force, startfit(0.8) from 80% of the maximum
force, //startfit(0.5) from 50% and so on.

function calcdef() //"calcdef()" transforms deformation into distance
data, requires
nvar k=root:k //that the spring constant is stored as a global variable in the
root
wave vDeflection, height //folder
duplicate/O vDeflection,Deformation
Deformation=height+vDeflection/k //calculation of the deformation
end

function baseline() //"baseline()", fits the baseline of a forcecurve
```

## 8. Appendix

---

```
wave vDeflection
variable i, XpickA, XpickB, YpickA, YpickB, m, n, V_sdev, V_avg

duplicate/O vDeflection, baselinefit, errorwave, vDefl

XpickB=0
YpickB=vDeflection[XpickB]
  for (XpickA=numpts(vDeflection);V_avg>=V_sdev;XpickA=XpickA-1)
//Calculates a straight line to fit the baseline, starts to draw a line between first and the last data point
of the force //curve, the difference between this line and the whole force curve decreases when going
backwards by drawing //the line from the first data point to decreasing data points (XpickA=XpickA-
1). This creates a moving straight line //which approaches the base line as XpickA=XpickA-1. If the
difference is small enough see “criteria” the //baseline fit is satisfying and the calculation is complete.

      YpickA=vDeflection[XpickA]
      m=(YpickA-YpickB)/(XpickA-XpickB)
      n=YpickA-(YpickA-YpickB)/(XpickA-XpickB)*XpickA
//slope m and axis intercept n, definition of the straight baseline fit
      for(i=0;i<XpickA;i=i+1)                                //generates a new baseline
fit
      baselinefit[i] = m*i+n

      endfor

      deletepoints XpickA, numpts(vDeflection)-XpickA, baselinefit
//severs off the points of the force curve that do not belong to the baseline
      deletepoints XpickA, numpts(vDeflection)-XpickA, errorwave
      deletepoints XpickA, numpts(vDeflection)-XpickA, vDefl
      errorwave=(baselinefit-vDefl)
//calculates the difference between the baseline and the forces, for the fit criterion
      wavestats/Q errorwave

      //the criteria that decide whether the baseline is good
enough
      if (V_avg<V_sdev)
        break
// Execute if condition is TRUE
// if the scatter is larger than the difference between the fit and the force data, the fitting is finished
      endif
      if (errorwave(numpts(errorwave))>V_avg)
        break
// Execute if condition is TRUE
// the (theoretically) largest point in the baseline-force difference is smaller than the average
```

## 8. Appendix

---

```
//baseline signal
    endif
    if (numpnts(vDefl)<3)
        print "no baseline fit possible"
        break
//if the baseline fit gets smaller than 3 data points the fit has failed
    endif

    endfor
appendtograph/C=(0,65535,0) baselinefit vs deformation
removefromgraph/Z baselinefit#1
killwaves/Z errorwave
//Note that the baseline fit is actually not a real fit, it merely finds the point where the cantilever has
//contact with //the sample and draws a line between this point and the first data point of the force
//curve. If desired, a "real" fit //could be easily established by using the fit function (see "CurveFit") in
//IgorPro by using the first- and the contact //data point as fit interval.
end

function forceslope(startfit,forcelength)
//"forceslope()" creates a linear force curve fit. The parameter "startfit" determines where the fit
//starts: startfit(1) means fitting from the maximum force, startfit(0.8) from 80% of the maximum
//force startfit(0.5) from 50% and so on. "forcelength" forces the fit to be performed from "stafit"
//down to the zero force value or baseline (forcelength(1)), from start fit to 80% of the zero force
//point (forcelength(0.8)), from start fit to 50% of the zero force point (forcelength(0.5)) and so on.

    variable startfit,forcelength
    wave vDeflection
    WAVE slopes=root:slopes
    variable i, XpickA, XpickB, YpickA, YpickB, m, n, V_sdev, V_avg, sdevDefl, sdeverrowave
    variable/G slope
    variable maxforces=vDeflection[+inf] //definition of the maximum force point as the last
point in the force //curve
    variable zeroforces=mean(baselinefit) //definition of the zero force point as the average of the
baseline
    removefromgraph/Z vdeflection, fit_vdeflection
    appendtograph/C=(0,0,65535) vdeflection vs deformation
    FindValue/T=(maxforces*startfit/100)/s=(zeroforces)/V=(maxforces*startfit) vDeflection
//finds the desired startfit value in the force curve
    XpickA=V_value
    if (XpickA==-1)
//if no starting value was found the tolerance is decreased and a new attempt //to find starting val//ue
is started
        FindValue/T=(maxforces*startfit/50)/s=(zeroforces)/V=(maxforces*startfit) vDeflection
        XpickA=V_value
    endif
    if (XpickA==-1)
        FindValue/T=(maxforces*startfit/10)/s=(zeroforces)/V=(maxforces*startfit) vDeflection
        XpickA=V_value
    endif

    if (XpickA==-1)
        print "range was too small, I am fitting the whole curve"
        XpickA=numpnts(vDeflection)
    endif
    if(startfit==1)
```

## 8. Appendix

---

```
        XpickA=numpnts(vDeflection)
    endif
    duplicate/O vDeflection, forcesfit, errorwave, vDefl
//creates temporary waves for the calculation
    deletepoints XpickA+1,+inf, forcesfit
    deletepoints XpickA+1,+inf, errorwave
    deletepoints XpickA+1,+inf, vDefl

    YpickA=vDeflection[XpickA]
    for (XpickB=0;V_avg>=V_sdev;XpickB=XpickB+1)
// the same fitting method as for as for the baseline is applied for fitting the force curve fit
//procedure, i.e. a moving straight line, which approaches stepwise to the force curve
//as XpickB=XpickB+1
        YpickB=vDeflection[XpickB]          //Def. der Geradenpunkte
        m=(YpickB-YpickA)/(XpickB-XpickA)
        n=YpickB-(YpickB-YpickA)/(XpickB-XpickA)*XpickB //Geradengleichung

        for(i=XpickB;i<XpickA;i=i+1)
//generates a new forcefit
            forcesfit[i-XpickB] = m*i+n

        endfor

        deletepoints 0, 1, forcesfit
//severs off the points that dont belong to the baseline
        SetScale/P x XpickB,1,"", forcesfit
        deletepoints 0, 1, errorwave
        SetScale/P x XpickB,1,"", errorwave
        deletepoints 0, 1, vDefl
        SetScale/P x XpickB,1,"", vDefl
        errorwave=(forcesfit-vDefl)
//calculates the difference between the baseline and the forces
        wavestats/Q errorwave
        FindValue/T=(maxforces*startfit/10)/s=(zeroforces)/V=(maxforces*startfit)
vDeflection
        if (V_avg<V_sdev)
            break
// Execute if condition is TRUE if the scatter is larger than the signal => baseline
        endif
        if (errorwave(numpnts(errorwave))>V_avg)
            break
// Execute if condition is TRUE the (theoretically) largest point in the baseline-force difference
// is smaller than the average baseline signal
        endif
        if (numpnts(vDefl)<3)
            print "no force fit possible"
            break
        endif
//the criterions that decide whether the baseline is good enough
        if (numpnts(forcesfit) < (numpnts(vDeflection)-XpickA)/10)
            break
        endif
        if (forcesfit[+inf]-forcesfit[0] < maxforces*startfit*forcelength)
            break
```

```
endif
endfor
CurveFit/Q/NTHR=0/TBOX=0 line vDeflection[XpickB,XpickA] /X=Deformation /D

// Note that the fit procedure is actually not a real fit yet, it merely draws a line between the
//“startfit()” parameter //and the “forcelength()” parameter. It furthermore decides whether the
//choice of parameters would lead to a //good fit. Now, a “real” fit is established by using the fit
//function “CurveFit” in IgorPro by using the two //parameters as the fit interval

wave W_coef
slope = W_coef[1]
print "slope=",slope
killwaves/Z errorwave
end
```

## 9 References

- [1] M. Chicurel, Cell migration research is on the move, *Science*, 2002, **295**, 606-609.
- [2] G. Romet-Lemonne, E. Helfer, V. Delatour, B. Bugyi, M. Bosch, S. Schmidt, A. Fery and M. F. Carlier, BIOMIMETIC SYSTEMS SHED LIGHT ON ACTIN-BASED MOTILITY DOWN TO THE MOLECULAR SCALE, *Biophysical Reviews and Letters*, 2009, **in press**.
- [3] E. Gouin, M. D. Welch and P. Cossart, Actin-based motility of intracellular pathogens, *Current Opinion in Microbiology*, 2005, **8**, 35-45.
- [4] A. Mogilner and G. Oster, Polymer motors: Pushing out the front and pulling up the back, *Current Biology*, 2003, **13**, R721-R733.
- [5] F. Gerbal, P. Chaikin, Y. Rabin and J. Prost, An elastic analysis of *Listeria monocytogenes* propulsion, *Biophysical Journal*, 2000, **79**, 2259-2275.
- [6] V. Noireaux, R. M. Golsteyn, E. Friederich, J. Prost, C. Antony, D. Louvard and C. Sykes, Growing an actin gel on spherical surfaces, *Biophysical Journal*, 2000, **78**, 1643-1654.
- [7] J. A. Theriot and T. J. Mitchison, ACTIN MICROFILAMENT DYNAMICS IN LOCOMOTING CELLS, *Nature*, 1991, **352**, 126-131.
- [8] J. V. Small, T. Stradal, E. Vignat and K. Rottner, The lamellipodium: where motility begins, *Trends Cell Biol.*, 2002, **12**, 112-120.
- [9] C. G. Dos Remedios, D. Chhabra, M. Kekic, I. V. Dedova, M. Tsubakihara, D. A. Berry and N. J. Nosworthy, Actin binding proteins: Regulation of cytoskeletal microfilaments, *Physiol. Rev.*, 2003, **83**, 433-473.
- [10] T. D. Pollard and J. A. Cooper, Actin and Actin-Binding Proteins - a Critical-Evaluation of Mechanisms and Functions, *Annual Review of Biochemistry*, 1986, **55**, 987-1035.
- [11] L. G. Tilney and D. A. Portnoy, ACTIN-FILAMENTS AND THE GROWTH, MOVEMENT, AND SPREAD OF THE INTRACELLULAR BACTERIAL PARASITE, *LISTERIA-MONOCYTOGENES*, *J. Cell Biol.*, 1989, **109**, 1597-1608.
- [12] T. P. Loisel, R. Boujemaa, D. Pantaloni and M. F. Carlier, Reconstitution of actin-based motility of *Listeria* and *Shigella* using pure proteins, *Nature*, 1999, **401**, 613-616.
- [13] D. Pantaloni, C. Le Clainche and M. F. Carlier, Cell biology - Mechanism of actin-based motility, *Science*, 2001, **292**, 1502-1506.
- [14] B. Bugyi, C. Le Clainche, G. Romet-Lemonne and M. F. Carlier, How do in vitro reconstituted actin-based motility assays provide insight into in vivo behavior?, *Febs Letters*, 2008, **582**, 2086-2092.
- [15] A. R. Bausch and K. Kroy, A bottom-up approach to cell mechanics, *Nature Physics*, 2006, **2**, 231-238.



## 9. References

---

- [16] Y. Luan, O. Lieleg, B. Wagner and A. R. Bausch, Micro- and macrorheological properties of isotropically cross-linked actin networks, *Biophysical Journal*, 2008, **94**, 688-693.
- [17] M. L. Gardel, J. H. Shin, F. C. MacKintosh, L. Mahadevan, P. Matsudaira and D. A. Weitz, Elastic Behavior of cross-linked and bundled actin networks, *Science*, 2004, **304**, 1301-1305.
- [18] M. Staat, G. Baroud, M. Topcu and S. Sponagel, Bioengineering in Cell and Tissue Research, Springer-Verlag, Berlin, 2008.
- [19] A. R. Bausch, W. Moller and E. Sackmann, Measurement of local viscoelasticity and forces in living cells by magnetic tweezers, *Biophysical Journal*, 1999, **76**, 573-579.
- [20] K. C. Holmes, D. Popp, W. Gebhard and W. Kabsch, ATOMIC MODEL OF THE ACTIN FILAMENT, *Nature*, 1990, **347**, 44-49.
- [21] P. R. Smith, W. E. Fowler, T. D. Pollard and U. Aebi, Structure of the Actin Molecule Determined from Electron-Micrographs of Crystalline Actin Sheets with a Tentative Alignment of the Molecule in the Actin Filament, *Journal of Molecular Biology*, 1983, **167**, 641-660.
- [22] T. D. Pollard, Regulation of actin filament assembly by Arp2/3 complex and formins, *Annual Review of Biophysics and Biomolecular Structure*, 2007, **36**, 451-477.
- [23] T. D. Pollard and G. G. Borisy, Cellular motility driven by assembly and disassembly of actin filaments, *Cell*, 2003, **112**, 453-465.
- [24] Y. L. Wang, EXCHANGE OF ACTIN SUBUNITS AT THE LEADING-EDGE OF LIVING FIBROBLASTS - POSSIBLE ROLE OF TREADMILLING, *J. Cell Biol.*, 1985, **101**, 597-602.
- [25] F. Julicher, K. Kruse, J. Prost and J. F. Joanny, Active behavior of the cytoskeleton, *Physics Reports-Review Section of Physics Letters*, 2007, **449**, 3-28.
- [26] K. Sekimoto, J. Prost, F. Julicher, H. Boukellal and A. Bernheim-Grosswasser, Role of tensile stress in actin gels and a symmetry-breaking instability, *European Physical Journal E*, 2004, **13**, 247-259.
- [27] K. John, P. Peyla, K. Kassner, J. Prost and C. Misbah, Nonlinear study of symmetry breaking in actin gels: Implications for cellular motility, *Physical Review Letters*, 2008, **1**, -.
- [28] S. Schmidt, J. Van der Gucht, P. M. Biesheuvel, R. Weinkamer, E. Helfer and A. Fery, Non-Gaussian curvature distribution of actin-propelled biomimetic colloid trajectories, *European Biophysics Journal with Biophysics Letters*, 2008, **37**, 1361-1366.
- [29] T. Yanagida, M. Nakase, K. Nishiyama and F. Oosawa, DIRECT OBSERVATION OF MOTION OF SINGLE F-ACTIN FILAMENTS IN THE PRESENCE OF MYOSIN, *Nature*, 1984, **307**, 58-60.
- [30] B. Alberts, A. Johnson, J. Lewis, M. Raff, K. Roberts and P. Walter, Molecular Biology of the Cell, Garland Science, London, 2007.

## 9. References

---

- [31] T. D. Pollard, W. Earnshaw and J. Lippincott-Schwartz, *Cell Biology*, Saunders/Elsevier, New York, 2007.
- [32] T. J. Mitchison and L. P. Cramer, Actin-based cell motility and cell locomotion, *Cell*, 1996, **84**, 371-379.
- [33] E. Reisler and E. H. Egelman, Actin structure and function: What we still do not understand, *J. Biol. Chem.*, 2007, **282**, 36133-36137.
- [34] M. F. Carlier, V. Laurent, J. Santolini, R. Melki, D. Didry, G. X. Xia, Y. Hong, N. H. Chua and D. Pantaloni, Actin depolymerizing factor (ADF/cofilin) enhances the rate of filament turnover: Implication in actin-based motility, *J. Cell Biol.*, 1997, **136**, 1307-1322.
- [35] E. Andrianantoandro and T. D. Pollard, Mechanism of actin filament turnover by severing and nucleation at different concentrations of ADF/cofilin, *Molecular Cell*, 2006, **24**, 13-23.
- [36] D. Pantaloni and M. F. Carlier, HOW PROFILIN PROMOTES ACTIN FILAMENT ASSEMBLY IN THE PRESENCE OF THYMOSIN-BETA-4, *Cell*, 1993, **75**, 1007-1014.
- [37] D. Didry, M. F. Carlier and D. Pantaloni, Synergy between actin depolymerizing factor cofilin and profilin in increasing actin filament turnover, *J. Biol. Chem.*, 1998, **273**, 25602-25611.
- [38] D. Sept and J. A. McCammon, Thermodynamics and kinetics of actin filament nucleation, *Biophysical Journal*, 2001, **81**, 667-674.
- [39] D. Yarar, W. To, A. Abo and M. D. Welch, The Wiskott-Aldrich syndrome protein directs actin-based motility by stimulating actin nucleation with the Arp2/3 complex, *Current Biology*, 1999, **9**, 555-558.
- [40] C. Co, D. T. Wong, S. Gierke, V. Chang and J. Taunton, Mechanism of actin network attachment to moving membranes: Barbed end capture by N-WASP WH2 domains, *Cell*, 2007, **128**, 901-913.
- [41] A. Mogilner and G. Oster, Force generation by actin polymerization II: The elastic ratchet and tethered filaments, *Biophysical Journal*, 2003, **84**, 1591-1605.
- [42] S. C. Kuo and J. L. McGrath, Steps and fluctuations of *Listeria monocytogenes* during actin-based motility, *Nature*, 2000, **407**, 1026-1029.
- [43] D. Pantaloni, R. Boujemaa, D. Didry, P. Gounon and M. F. Carlier, The Arp2/3 complex branches filament barbed ends: functional antagonism with capping proteins, *Nature Cell Biology*, 2000, **2**, 385-391.
- [44] O. Akin and R. D. Mullins, Capping protein increases the rate of actin-based motility by promoting filament nucleation by the Arp2/3 complex, *Cell*, 2008, **133**, 841-851.
- [45] D. R. Kovar, Molecular details of formin-mediated actin assembly, *Current Opinion in Cell Biology*, 2006, **18**, 11-17.
- [46] B. L. Goode and M. J. Eck, Mechanism and function of formins in the control of actin assembly, *Annual Review of Biochemistry*, 2007, **76**, 593-627.

## 9. References

---

- [47] D. Pruyne, M. Evangelista, C. S. Yang, E. F. Bi, S. Zigmond, A. Bretscher and C. Boone, Role of formins in actin assembly: Nucleation and barbed-end association, *Science*, 2002, **297**, 612-615.
- [48] S. Wiesner, E. Helfer, D. Didry, G. Ducouret, F. Lafuma, M. F. Carlier and D. Pantaloni, A biomimetic motility assay provides insight into the mechanism of actin-based motility, *J. Cell Biol.*, 2003, **160**, 387-398.
- [49] V. Delatour, S. Shekhar, A. C. Reymann, D. Didry, K. H. D. Le, G. Romet-Lemonne, E. Helfer and M. F. Carlier, Actin-based propulsion of functionalized hard versus fluid spherical objects, *New J. Phys.*, 2008, **10**, 20.
- [50] A. Upadhyaya, J. R. Chabot, A. Andreeva, A. Samadani and A. van Oudenaarden, Probing polymerization forces by using actin-propelled lipid vesicles, *Proceedings of the National Academy of Sciences of the United States of America*, 2003, **100**, 4521-4526.
- [51] L. A. Cameron, M. J. Footer, A. van Oudenaarden and J. A. Theriot, Motility of ActA protein-coated microspheres driven by actin polymerization, *Proceedings of the National Academy of Sciences of the United States of America*, 1999, **96**, 4908-4913.
- [52] S. Romero, C. Le Clainche, D. Didry, C. Egile, D. Pantaloni and M. F. Carlier, Formin is a processive motor that requires profilin to accelerate actin assembly and associated ATP hydrolysis, *Cell*, 2004, **119**, 419-429.
- [53] R. B. Dickinson, L. Caro and D. L. Purich, Force generation by cytoskeletal filament end-tracking proteins, *Biophysical Journal*, 2005, **88**, 12a-12a.
- [54] J. L. McGrath, N. J. Eungdamrong, C. I. Fisher, F. Peng, L. Mahadevan, T. J. Mitchison and S. C. Kuo, The force-velocity relationship for the actin-based motility of *Listeria monocytogenes*, *Current Biology*, 2003, **13**, 329-332.
- [55] Y. Marcy, J. Prost, M. F. Carlier and C. Sykes, Forces generated during actin-based propulsion: A direct measurement by micromanipulation, *Proceedings of the National Academy of Sciences of the United States of America*, 2004, **101**, 5992-5997.
- [56] Y. Marcy, J. F. Joanny, J. Prost and C. Sykes, Probing friction in actin-based motility, *New J. Phys.*, 2007, **9**, -.
- [57] S. H. Parekh, O. Chaudhuri, J. A. Theriot and D. A. Fletcher, Loading history determines the velocity of actin-network growth, *Nature Cell Biology*, 2005, **7**, 1219-1223.
- [58] J. L. Choy, S. H. Parekh, O. Chaudhuri, A. P. Liu, C. Bustamante, M. J. Footer, J. A. Theriot and D. A. Fletcher, Differential force microscope for long time-scale biophysical measurements, *Rev. Sci. Instrum.*, 2007, **78**, 6.
- [59] O. Chaudhuri, S. H. Parekh and D. A. Fletcher, Reversible stress softening of actin networks, *Nature*, 2007, **445**, 295-298.
- [60] P. A. Giardini, D. A. Fletcher and J. A. Theriot, Compression forces generated by actin comet tails on lipid vesicles, *Proceedings of the National Academy of Sciences of the United States of America*, 2003, **100**, 6493-6498.

## 9. References

---

- [61] M. J. Footer, J. W. J. Kerssemakers, J. A. Theriot and M. Dogterom, Direct measurement of force generation by actin filament polymerization using an optical trap, *Proceedings of the National Academy of Sciences of the United States of America*, 2007, **104**, 2181-2186.
- [62] Molecular Motors, Wiley-VCH, Weinheim, 2003.
- [63] A. Mogilner and G. Oster, Cell motility driven by actin polymerization, *Biophysical Journal*, 1996, **71**, 3030-3045.
- [64] L. A. Cameron, T. M. Svitkina, D. Vignjevic, J. A. Theriot and G. G. Borisy, Dendritic organization of actin comet tails, *Current Biology*, 2001, **11**, 130-135.
- [65] E. Evans and K. Ritchie, Strength of a weak bond connecting flexible polymer chains, *Biophysical Journal*, 1999, **76**, 2439-2447.
- [66] L. Landau and E. Lifchitz, Teoriya Uprugosti (Theory of Elasticity), Nauka, Moscow, 1967.
- [67] A. Bernheim-Groswasser, S. Wiesner, R. M. Golsteyn, M. F. Carlier and C. Sykes, The dynamics of actin-based motility depend on surface parameters, *Nature*, 2002, **417**, 308-311.
- [68] A. Bernheim-Groswasser, J. Prost and C. Sykes, Mechanism of actin-based motility: A dynamic state diagram, *Biophysical Journal*, 2005, **89**, 1411-1419.
- [69] I. M. Schwartz, M. Ehrenberg, M. Bindschadler and J. L. McGrath, The role of substrate curvature in actin-based pushing forces, *Current Biology*, 2004, **14**, 1094-1098.
- [70] J. Plastino, I. Lelidis, J. Prost and C. Sykes, The effect of diffusion, depolymerization and nucleation promoting factors on actin gel growth, *European Biophysics Journal with Biophysics Letters*, 2004, **33**, 310-320.
- [71] J. van der Gucht, E. Paluch, J. Plastino and C. Sykes, Stress release drives symmetry breaking for actin-based movement, *Proceedings of the National Academy of Sciences of the United States of America*, 2005, **102**, 7847-7852.
- [72] T. L. Hill and M. W. Kirschner, SUBUNIT TREADMILLING OF MICROTUBULES OR ACTIN IN THE PRESENCE OF CELLULAR BARRIERS - POSSIBLE CONVERSION OF CHEMICAL FREE-ENERGY INTO MECHANICAL WORK, *Proceedings of the National Academy of Sciences of the United States of America-Biological Sciences*, 1982, **79**, 490-494.
- [73] A. van Oudenaarden and J. A. Theriot, Cooperative symmetry-breaking by actin polymerization in a model for cell motility, *Nature Cell Biology*, 1999, **1**, 493-499.
- [74] A. A. Griffith, THE PHENOMENA OF RUPTURE AND FLOW IN SOLIDS, *Philosophical Transactions of the Royal Society of London*, 1920, **221**, 163-197.
- [75] B. D. Murphy, Fundamentals of Light Microscopy and Electronic Imaging, Wiley-Liss, Inc, New York, 2001.
- [76] S. Inoue and K. Spring, Video Microscopy: the Fundamentals, Plenum Press, New York, 1997.
- [77] H.-J. Eichler and e. al., Bergmann Schäfer - Band 3 Optik Walter de Gruyter, Berlin, New York, 2004.

- [78] A. H. Bennett and e. al., *Phase Microscopy: Principles and Applications*, Wiley, New York, 1951.
- [79] F. Zernike, in *Achievements in Optics*, ed. A. Bouwers, Elsevier, New York, Amsterdam, 1946.
- [80] F. Zernike, How I Discovered Phase Contrast, *Science*, 1955, **121**, 345-349.
- [81] O. Wolfbeis and e. al., *Fluorescence Methods and Applications*, Wiley New York, 2008.
- [82] G. Binnig, C. F. Quate and C. Gerber, Atomic Force Microscope, *Physical Review Letters*, 1986, **56**, 930-933.
- [83] G. Binnig, C. Gerber, E. Stoll, T. R. Albrecht and C. F. Quate, Atomic Resolution with Atomic Force Microscope, *Europhysics Letters*, 1987, **3**, 1281-1286.
- [84] M. Radmacher, Measuring the elastic properties of living cells by the atomic force microscope, *Atomic Force Microscopy in Cell Biology*, 2002, **68**, 67-90.
- [85] J. L. Alonso and W. H. Goldmann, Feeling the forces: atomic force microscopy in cell biology, *Life Sciences*, 2003, **72**, 2553-2560.
- [86] A. Simon and M. C. Durrieu, Strategies and results of atomic force microscopy in the study of cellular adhesion, *Micron*, 2006, **37**, 1-13.
- [87] I. Dulinska, M. Targosz, W. Strojny, M. Lekka, P. Czuba, W. Balwierz and M. Szymonski, Stiffness of normal and pathological erythrocytes studied by means of atomic force microscopy, *Journal of Biochemical and Biophysical Methods*, 2006, **66**, 1-11.
- [88] D. J. Muller, K. T. Sapra, S. Scheuring, A. Kedrov, P. L. Frederix, D. Fotiadis and A. Engel, Single-molecule studies of membrane proteins, *Current Opinion in Structural Biology*, 2006, **16**, 489-495.
- [89] T. E. Fisher, P. E. Marszalek and J. M. Fernandez, Stretching single molecules into novel conformations using the atomic force microscope, *Nature Structural Biology*, 2000, **7**, 719-724.
- [90] K. A. Addae-Mensah and J. P. Wikswo, Measurement techniques for cellular biomechanics in vitro, *Experimental Biology and Medicine*, 2008, **233**, 792-809.
- [91] R. Dimova, S. Aranda, N. Bezlyepkina, V. Nikolov, K. A. Riske and R. Lipowsky, A practical guide to giant vesicles. Probing the membrane nanoregime via optical microscopy, *Journal of Physics-Condensed Matter*, 2006, **18**, S1151-S1176.
- [92] K. Dholakia, M. P. MacDonald, P. Zemanek and T. Cizmar, Cellular and colloidal separation using optical forces, *Laser Manipulation of Cells and Tissues*, 2007, **82**, 467-495.
- [93] D. Collard, C. Yamahata, B. Legrand, T. Takekawa, M. Kumemura, N. Sakaki, G. Hashiguchi and H. Fujita, Towards mechanical characterization of biomolecules by MNEMS tools, *Ieej Transactions on Electrical and Electronic Engineering*, 2007, **2**, 262-271.
- [94] K. C. Neuman and A. Nagy, Single-molecule force spectroscopy: optical tweezers, magnetic tweezers and atomic force microscopy, *Nature Methods*, 2008, **5**, 491-505.

- [95] S. Alexander, L. Hellemans, O. Marti, J. Schneir, V. Elings, P. K. Hansma, M. Longmire and J. Gurley, An Atomic-Resolution Atomic-Force Microscope Implemented Using an Optical-Lever, *Journal of Applied Physics*, 1989, **65**, 164-167.
- [96] P. Samoni, Scanning Probe Microscopy Beyond Imaging, Wiley-VCH, Weinheim, 2006.
- [97] E. Meyer, H.-J. Hug and R. Bennewitz, Scanning Probe Microscopy: The Lab on a Tip Springer, Berlin, 2003.
- [98] R. Garcia and R. Perez, Dynamic atomic force microscopy methods, *Surface Science Reports*, 2002, **47**, 197-301.
- [99] H. J. Butt, B. Cappella and M. Kappl, Force measurements with the atomic force microscope: Technique, interpretation and applications, *Surface Science Reports*, 2005, **59**, 1-152.
- [100] A. L. Weisenhorn, P. K. Hansma, T. R. Albrecht and C. F. Quate, Forces in Atomic Force Microscopy in Air and Water, *Applied Physics Letters*, 1989, **54**, 2651-2653.
- [101] S. Kasas and G. Dietler, Probing nanomechanical properties from biomolecules to living cells, *Pflugers Archiv-European Journal of Physiology*, 2008, **456**, 13-27.
- [102] A. Fery and R. Weinkamer, Mechanical properties of micro- and nanocapsules: Single-capsule measurements, *Polymer*, 2007, **48**, 7221-7235.
- [103] J. E. Sader, Frequency response of cantilever beams immersed in viscous fluids with applications to the atomic force microscope, *Journal of Applied Physics*, 1998, **84**, 64-76.
- [104] J. L. Hutter and J. Bechhoefer, CALIBRATION OF ATOMIC-FORCE MICROSCOPE TIPS, *Rev. Sci. Instrum.*, 1993, **64**, 1868-1873.
- [105] W. A. Ducker, T. J. Senden and R. M. Pashley, Direct Measurement of Colloidal Forces Using an Atomic Force Microscope, *Nature*, 1991, **353**, 239-241.
- [106] V. Bosio, Interactions of multilayer coated surfaces studied by colloidal probe Atomic Force Microscopy, PhD Thesis, Potsdam, 2003.
- [107] J. A. Spudich and S. Watt, REGULATION OF RABBIT SKELETAL MUSCLE CONTRACTION .1. BIOCHEMICAL STUDIES OF INTERACTION OF TROPOMYOSIN-TROPONIN COMPLEX WITH ACTIN AND PROTEOLYTIC FRAGMENTS OF MYOSIN, *J. Biol. Chem.*, 1971, **246**, 4866-&.
- [108] H. Isambert, P. Venier, A. C. Maggs, A. Fattoum, R. Kassab, D. Pantaloni and M. F. Carlier, FLEXIBILITY OF ACTIN-FILAMENTS DERIVED FROM THERMAL FLUCTUATIONS - EFFECT OF BOUND NUCLEOTIDE, PHALLOIDIN, AND MUSCLE REGULATORY PROTEINS, *J. Biol. Chem.*, 1995, **270**, 11437-11444.
- [109] I. Gutsche-Perelroizen, J. Lepault, A. Ott and M. F. Carlier, Filament assembly from profilin-actin, *J. Biol. Chem.*, 1999, **274**, 6234-6243.
- [110] C. Egile, T. P. Loisel, V. Laurent, R. Li, D. Pantaloni, P. J. Sansonetti and M. F. Carlier, Activation of the CDC42 effector N-WASP by the *Shigella flexneri* IcsA

- protein promotes actin nucleation by Arp2/3 complex and bacterial actin-based motility, *J. Cell Biol.*, 1999, **146**, 1319-1332.
- [111] A. Upadhyaya and A. van Oudenaarden, Actin polymerization: Forcing flat faces forward, *Current Biology*, 2004, **14**, R467-R469.
- [112] S. van Teeffelen and H. Lowen, Dynamics of a Brownian circle swimmer - art. no. 020101, *Physical Review E*, 2008, **78**, 101-101.
- [113] L. A. Cameron, J. R. Robbins, M. J. Footer and J. A. Theriot, Biophysical parameters influence actin-based movement, trajectory, and initiation in a cell-free system, *Molecular Biology of the Cell*, 2004, **15**, 2312-2323.
- [114] V. B. Shenoy, D. T. Tambe, A. Prasad and J. A. Theriot, A kinematic description of the trajectories of *Listeria monocytogenes* propelled by actin comet tails, *Proceedings of the National Academy of Sciences of the United States of America*, 2007, **104**, 8229-8234.
- [115] A. D. Rutenberg and M. Grant, Curved tails in polymerization-based bacterial motility, *Physical Review E*, 2001, **6402**, -.
- [116] D. M. Woolley, Motility of spermatozoa at surfaces, *Reproduction*, 2003, **126**, 259-270.
- [117] B. C. Carter, G. T. Shubeita and S. P. Gross, Tracking single particles: a user-friendly quantitative evaluation, *Physical Biology*, 2005, **2**, 60-72.
- [118] E. Kreyszig, Differential geometry, Dover, New York, 1991.
- [119] S. Caldwell, Statistics Unplugged Wadsworth Publishing, 2006.
- [120] D. T. Gillespie, EXACT STOCHASTIC SIMULATION OF COUPLED CHEMICAL-REACTIONS, *J. Phys. Chem.*, 1977, **81**, 2340-2361.
- [121] E. Paluch, J. van der Gucht, J. F. Joanny and C. Sykes, Deformations in actin comets from rocketing beads, *Biophysical Journal*, 2006, **91**, 3113-3122.
- [122] W. L. Zeile, F. L. Zhang, R. B. Dickinson and D. L. Purich, *Listeria*'s right-handed helical rocket-tail trajectories: Mechanistic implications for force generation in actin-based motility, *Cell Motil. Cytoskeleton*, 2005, **60**, 121-128.
- [123] S. E. Hulme, W. R. DiLuzio, S. S. Shevkoplyas, L. Turner, M. Mayer, H. C. Berg and G. M. Whitesides, Using ratchets and sorters to fractionate motile cells of *Escherichia coli* by length, *Lab Chip*, 2008, **8**, 1888-1895.
- [124] G. Csucs, R. Michel, J. W. Lussi, M. Textor and G. Danuser, Microcontact printing of novel co-polymers in combination with proteins for cell-biological applications, *Biomaterials*, 2003, **24**, 1713-1720.
- [125] N. V. Lavrik, M. J. Sepaniak and P. G. Datskos, Cantilever transducers as a platform for chemical and biological sensors, *Rev. Sci. Instrum.*, 2004, **75**, 2229-2253.
- [126] J. M. Gere, Mechanics of Materials, Thomson Learning, Inc., Belmont (CA), 2004.
- [127] J. A. Cooper, EFFECTS OF CYTOCHALASIN AND PHALLOIDIN ON ACTIN, *J. Cell Biol.*, 1987, **105**, 1473-1478.
- [128] R. E. Mahaffy and T. D. Pollard, Influence of phalloidin on the formation of actin filament branches by Arp2/3 complex, *Biochemistry*, 2008, **47**, 6460-6467.

## 9. References

---

- [129] B. J. Wallar and A. S. Alberts, The formins: active scaffolds that remodel the cytoskeleton, *Trends Cell Biol.*, 2003, **13**, 435-446.
- [130] A. Michelot, J. Berro, C. Guerin, R. Boujemaa-Paterski, C. J. Staiger, J. L. Martiel and L. Blanchoin, Actin-filament stochastic dynamics mediated by ADF/cofilin, *Current Biology*, 2007, **17**, 825-833.
- [131] A. M. Bieser and J. C. Tiller, Surface-induced hydrogelation, *Chem. Commun.*, 2005, 3942-3944.
- [132] D. G. Kurth, Metallo-supramolecular modules as a paradigm for materials science, *Sci. Technol. Adv. Mater.*, 2008, **9**, 25.
- [133] A. Aderem and D. M. Underhill, Mechanisms of phagocytosis in macrophages, *Annu. Rev. Immunol.*, 1999, **17**, 593-623.
- [134] F. Dubreuil, N. Elsner and A. Fery, Elastic properties of polyelectrolyte capsules studied by atomic-force microscopy and RICM, *European Physical Journal E*, 2003, **12**, 215-221.
- [135] J. H. C. Wang and J. S. Lin, Cell traction force and measurement methods, *Bio-mech. Model. Mechanobiol.*, 2007, **6**, 361-371.



## Acknowledgements

---

I would like to take the opportunity to thank all the people who supported me through my PhD studies. First and foremost, I express my gratitude to my PhD supervisor Prof. Andreas Fery for the outstanding supervision and the interesting topic. I also like to thank Marie-France Carlier for taking share in initiating this project and being the “thought leader” of the biochemistry part. Prof. Helmut Möhwald is to thank for fruitful discussions and providing the position at the MPI’s interface department in the first place.

Working with the in-vitro medium would not have been possible without the expertise and constant aid of Emmanuelle Helfer and Guillaume Romet-Lemonne. I am also grateful to Maarten Biesheuvel and Jasper van der Gucht for their modeling calculations that indeed added meaning to the experiments. I will not forget to thank my “old” group members Phillipe, Nils and Renate for their technical (and personal) help with getting AFM experiments working, so thank you! I also thank the other group members in Golm me for creating such a cooperative and relaxed atmosphere in the lab.

After moving to Bayreuth things were different first, not on a negative note, but because of the lack of group members. At this point, many thanks to Eva for helping me to set up the lab in Bayreuth and guiding me through the “city” and the University. I also appreciate the help of the technical staff at our chair and the mechanical workshop for helping us with modifications in the lab and creating helpful gadgets for the experiments. I am especially thankful that Pia and Georg showed interest in my work and finally released me from working on my own. My (ex)office mates Alex, Öznur, Melanie, Daniel, Johann and others are to blame for some fun in the office; pleasure to work with you! Finally, I would like to thank Laura for reviewing this text and for keeping it close although 10000 miles away.

I acknowledge financial support by the European Community program STREP “Active Biomics”, the Max-Planck Society and the University of Bayreuth.

Hiermit erkläre ich, dass ich die vorliegende Arbeit selbständig verfasst, und keine anderen als die angegebenen Quellen und Hilfsmittel benutzt habe.

Ferner erkläre ich, dass ich weder an der Universität Bayreuth noch anderweitig mit oder ohne Erfolg versucht habe, eine Dissertation einzureichen oder eine Doktorprüfung abzulegen.

Bayreuth, den 27.02.2009

Stephan Schmidt